Lehrstuhl für Fluidmechanik und Prozessautomation
der Technischen Universität München

Numerical Investigation of Thermofluiddynamical Heterogeneities during High Pressure Treatment of Biotechnological Substances

Panit Kitsubun

Vollständiger Abdruck der von der Fakultät Wissenschaftszentrum Weihenstephan für Ernährung, Landnutzung und Umwelt der Technischen Universität München zur Erlangung des akademischen Grades eines

Doktor-Ingenieurs (Dr.-Ing.)

genehmigten Dissertation.

Vorsitzender: Univ.-Prof. Dr.rer.nat.habil. Rudi F. Vogel

Prüfer der Dissertation:

1. Univ.-Prof. Dr.-Ing.habil. Antonio Delgado
   (Friedrich-Alexander-Universität Erlangen-Nürnberg)

2. Univ.-Prof. Dr.-Ing.habil. Rainer Friedrich, em.
   (schriftliche Beurteilung)

3. Univ.-Prof. Dr.-Ing. Karl Sommer

Die Dissertation wurde am 16.03.06 bei der Technischen Universität München eingereicht und durch die Fakultät Wissenschaftszentrum Weihenstephan für Ernährung, Landnutzung und Umwelt am 19.07.06 angenommen.

Dedicated to Peter, Christoph and Klaus

And all the Thai students in Germany

It was so much fun with all of you guys!

Publications

Publications

Hartmann, C., Schuhholz, J.-P., Kitsubun, P., Chapleau, N., Le Bail, A., Delgado, A. 2004. Experimental and numerical analysis of the thermofluiddynamics in a high-pressure autoclave, Innovative Food Science and Emerging Technologies, 5, 399-411.

Kilimann, K.V., Kitsubun, P., Chapleau, N., Le Bail, A., Delgado, A., and Gänzle, M.G. and Hartmann, C. Simulation of heterogeneous pressure-temperature induced lethal and sublethal injury of *Lactococcus lactis* in a industrial 3.3-Litre-High-Pressure-Autoclave, Biotechnology and Bioengineering, 94(4), 655-666.

Proceedings

Kitsubun, P., Hartmann, C., Delgado., A. 2004. Numerische Analyse von Prozessinhomogenitäten bei der Hochdruckbehandlung von Lebensmitteln, Gesellschaft für Angewandte Mathematik und Mechanik (GAMM), Dresden, Proceedings in Applied Mathematics and Mechanics (PAMM), WILEY-VCH Verlag Weinheim, 4(1), 486-487.

Diez, L., Zima, E., Kitsubun, P., Hartmann, Ch., Delgado, A. 2005. Numerical Simulation of Granula Motion in Sequencing Batch Reactor (SBR). Books of Abstracts, 11th Workshop on Two-Phase Flow Predictions.

Kitsubun, P., Hartmann, C., Delgado., A. 2005. Numerical Investigations of Process Heterogeneities during High Hydrostatic Pressure Treatment with Turbulent Inflow Conditions, Gesellschaft für Angewandte Mathematik und Mechanik (GAMM), Luxembourg, Proceedings in Applied Mathematics and Mechanics (PAMM), WILEY-VCH Verlag Weinheim, 5(1), 573-574.

Oral presentations

Kitsubun, P., Hartmann, C., Delgado, A. 2004. Numerische Analyse von Prozessinhomogenitäten bei der Hochdruckbehandlung von Lebensmitteln. GVC Fachausschuss Hochdruckverfahrenstechnik, 4./5. Februar 2004, Karlsruhe.

Kitsubun, P., Hartmann, C., Delgado, A. 2004. Numerische Analyse von Prozessinhomogenitäten bei der Hochdruckbehandlung von Lebensmitteln. Jahrestagung der Gesellschaft für Angewandte Mathematik (GAMM), Dresden, 21.-27.03.2004.

Kitsubun, P., Hartmann, C., Delgado, A. 2004. Numerische Analyse von Prozessinhomogenitäten bei der Hochdruckbehandlung von Lebensmitteln. GVC Fachausschuss Computational Fluid Dynamics und Rheologie., Würzburg.

Kitsubun, P., Hartmann, C., Delgado, A. 2004. Numerical Investigation of Process Heterogeneities During High Hydrostatic Pressure Treatment with Turbulent Inflow Conditions, 3rd International Conferences on High Pressure Bioscience and Biotechnology, Rio de Janeiro, Brazil, 27.-30.9.2004.

Kitsubun, P., Hartmann, C., Delgado, A. 2004., Numerische Untersuchungen von Prozessheterogenitäten während der Hochdruckbehandlung mit turbulenten Bedingungen“, Gemeinsames Statusseminar von BMBF-, DBU- und DFG -geförderten Forschungsprojekten „Hochdrucklebensmitteltechnologie und -bioverfahrenstechnik“, October 2004, TU München.

Kitsubun, P., Hartmann, C., Delgado, A. 2005. Numerical Investigations of Process Heterogeneities during High Hydrostatic Pressure Treatment with Turbulent Inflow Conditions, Jahrestagung der Gesellschaft für Angewandte Mathematik (GAMM), Luxembourg, 28.03.-01.04.2005.

Diez, L., Zima, E., Kitsubun, P., Hartmann, Ch., Delgado, A. 2005. Numerical Simulation of Granula Motion in Sequencing Batch Reactor (SBR). 11th Workshop on Two-Phase Flow Predictions, Halle, 5.-8. April 2005.

Poster presentation

Kitsubun, P., Delgado, A. 2005. Numerical simulation of the process non-uniformity during high pressure treatment with turbulent inflow conditions. 1st European Congress on Life Science Process Technology, Nürnberg, 11.-13. October 2005.

Kitsubun, P., Kilimann, K. V., Rauh, C., Delgado A. 2005. Experimental and numerical study of thermofluiddynamically induced lethal and sublethal injury of *Lactococcuc lactis* in a medium scale high pressure autoclave, 1st International Symposium on Biothermodynamics, Frankfurt am Main, 16. – 17. February 2006.

KURZFASSUNG

Die Hochdrucktechnologie ist eine neuartige Anwendung zur Zubereitung und Haltbarmachung von biotechnologischen Substanzen, z. B. Lebensmitteln. Hierbei werden biotechnologische Substanzen in sog. Hochdruckautoklaven bei Drücken bis zu 1.000 MPa behandelt. Beim Vorgang der Kompression wird die Volumenänderungsarbeit in innere Energie umgesetzt, so dass sich die Temperatur im Hochdruckautoklaven erhöht. In kleineren Hochdruckautoklaven lassen sich solche Temperaturerhöhungen relativ einfach mit Einrichtungen zur Temperierung in den Griff bekommen. In größeren Hochdruckautoklaven liegt indessen keine gleichmäßige Temperaturverteilung innerhalb des Autoklaven vor. Da die Heterogenität in der Temperaturverteilung Einflüsse auf die Qualität des Produkts ausübt, stellt dies eine der wichtigsten Problemstellungen in der Hochdruckbehandlung von Lebensmitteln dar.

Die vorliegende Arbeit widmet sich der Analyse der thermofluiddynamischen Prozesse während der Hochdruckbehandlung von biotechnologischen Substanzen mit Hilfe der theoretischen Modellierung und der numerischen Simulationen. Der Finite-Volumen-Code CFX-5.7 und CFX-10 wurde mit selbst entwickelten Subroutinen erweitert, um thermofluiddynamische Vorgänge bei der Hochdruckbehandlung von verschiedenen biotechnologischen Substanzen bei 500 MPa simulieren zu können. Hierzu werden zwei Inaktivierungskinetiken mit in das Programm implementiert.

Zum einen gibt die Verwendung der Inaktivierungskinetik des Enzyms *Bacillus subtilis* α-Amylase bei den Untersuchungen des Strömungsverhaltens des Druckmediums „Wasser“ Auskunft darüber, wie sich die thermische Heterogenität auf die Homogenität bei der Behandlung von flüssigen Lebensmitteln auswirkt. Anhand verschiedener Prozesstrajektorien werden Einflüsse verschiedener fluiddynamischer Subvorgänge auf die gesamte Hochdruckbehandlung, vor allem die Verteilung der Temperatur sowie der Restaktivität des Enzyms, untersucht. Die dimensionslosen Zahlen Re, Pr, Fr, Gr, Ra und $\alpha_0 T_0$ geben zusätzlich Auskunft über das Verhalten der Strömung des Druckmediums im Autoklaven. Es kann gezeigt werden, dass das Zusammenspiel der thermischen Expansion und der Kühlung durch das Wandmaterial des Autoklaven maßgeblich für die Heterogenität des Systems ist. Außerdem stellen die Interaktionen zwischen der erzwungenen Konvektion, die durch die Zuströmung des Druckmediums entsteht, und der freien Konvektion, die von den Temperaturunterschieden der Flüssigkeit hervorgerufen wird, einen höchst interessanten fluiddynamischen Vorgang dar. Es wird gezeigt, wie mit einfachen Hilfsmitteln die Heterogenität des Systems minimiert werden kann.

Zum anderen ist es erstmalig möglich, die ortabhängigen Inaktivierungsvorgänge von Mikroorganismen in einem mittelgroßen Hochdruckautoklaven vorauszusagen. Das zusammen mit Herrn Dr.-Ing. Klaus Kilimann entwickelte Modell zur Inaktivierung von *Lactococcus lactis* in einem 3,3-Liter Autoklaven in 3 verschiedenen Lebensmittelmatrizen zeigt, wie mit Hilfe einer anderen Modellierungsmethode eine höchst präzise Voraussage über die Abtötungskinetiken von Mikroorganismen in mittelgroßen Hochdruckautoklaven gemacht werden kann. Hierfür wurde ein Hybridverfahren aus CFD und dem Verhulst-Pearl Modell entwickelt. Dies stellt eine Weltneuheit dar, womit Aussagen über die Produktsicherheit hinsichtlich der mikrobiellen Kontamination während einer Hochdruckbehandlung in mittelgroßen Hochdruckautoklaven gemacht werden können.

ABSTRACT

High pressure technology is a new application in the preparation and preservation of biotechnological substances, e.g. food. Here, biotechnological substances are treated with pressures up to 1,000 MPa in high pressure autoclaves. During the procedure of the volume change work is converted into internal energy, so that the temperature in high pressure autoclaves increases. In smaller high pressure autoclaves, such temperature increase can be controlled effectively. In larger high pressure autoclaves, however, temperature gradients are prominent. Since the heterogeneity in the temperature distribution has influences on the quality of the product, this represents one of the most important problems in the high pressure treatment of food.

This work dedicates itself to the analysis of the thermofluiddynamic processes during the high pressure treatment of biotechnological substances using theoretical modelling and numerical simulations. The finite volume code CFX-5.7 and CFX-10 are extended with own subroutines, in order to be able to simulate thermofluiddynamic processes during the high pressure treatment of different biotechnological substances with 500 MPa. For this two inactivation kinetics are also implemented into the program.

On the one hand, the use of inactivation kinetics of the enzyme *Bacillus subtilis* α-Amylase to investigate the flow behaviour of the fluid "water" gives information about how the thermal heterogeneity affects the homogeneity of the treatment of liquid food. Different process trajectories lead to different fluiddynamic processes during the entire high pressure treatment. Above all, the distributions of the temperature as well as of the residual activity of the enzyme are examined.

The dimensionless numbers, Re, Pr, Fr, Gr, Ra and $\alpha_0 T_0$, give additional information on the behaviour of the fluid movements in the autoclaves. It can be shown that the interaction of the thermal expansion and the cooling process by the wall material of the autoclaves is relevant for the heterogeneity of the system. In addition, the interactions between forced convection, which results from the inflow of the fluid, and free convection, which is caused by the temperature differences of the liquid, represent one of the most interesting fluiddynamic procedures during the high pressure process. It should also be shown, how the heterogeneity of the system can be minimized with simple measures.

On the other hand, for the first time it is possible to forecast the local inactivation process of micro organisms in medium sized high pressure autoclaves. The developed model for the inactivation of *Lactococcus lactis* in a 3.3-liter autoclaves in 3 different food matrices shows how another modelling method enables a highly precise forecast of the inactivation kinetics of micro organisms in medium sized high pressure autoclaves. Therefore, a hybrid approach of CFD and the Verhulst Pearl model was developed. This represents an innovation, with which statements about food safety regarding the microbial contamination during a high pressure treatment in medium sized high pressure autoclaves can be made.

CONTENTS

1 INTRODUCTION 1

1.1 High Pressure Treatment in Biotechnology 1

1.2 Process Non-uniformities during the High Pressure Treatment 4

1.3 Numerical Simulation of High Pressure Processing 5

1.4 Objectives 8

2 THEORETICAL CONSIDERATIONS TO MODELLING AND SIMULATION OF THE HIGH PRESSURE PROCESSING 10

2.1 Physical Properties of Liquid Water under High Pressure 10

2.2 Equilibrium Thermodynamics of Water as a homogeneous system 15

2.3 Introductory Remarks to Computational Fluid Dynamics (CFD) 20

2.3.1 Conservation of Mass 22

2.3.2 Conservation of Momentum 22

2.3.3 Conservation of Energy 25

2.4 Dimensionless equations for the high pressure treatment 27

2.4.1 Fundamental dimensionless equations 28

2.4.1.1 Dimensionless equation of mass conservation for forced convection 30

2.4.1.2 Dimensionless equation of momentum conservation for forced convection 31

2.4.1.3 Dimensionless equation of energy conservation for forced convection 35

2.4.1.4 Dimensionless equation of mass conservation for free convection 40

2.4.1.5 Dimensionless equation of momentum conservation for free convection 41

2.4.1.6 Dimensionless equation of energy conservation for free convection 42

2.4.2 Dimensionless equation for the temperature change 44

2.5 Characteristics of Buoyant Turbulent Free Shear Flows 46

2.6 Computation with Turbulence Models 50

2.6.1 Shear Stress Transport (SST) Model 52

2.7 Equations for the Pressure Induced Biotechnological Conversion Process 54

2.7.1 Inactivation of *Bacillus subtilis* α-Amylase 56

2.7.2 Inactivation of lactic acid bacteria 57

2.7.3 Dimensionless transport equation for an additional scalar 58

3 NUMERICAL METHODS 60

3.1.1 Meshing 60

3.1.2 Solution Technique 63

3.1.3 Discretisation of the governing equations 64

3.1.4 Convergence Criteria 66

3.1.5 Initial and Boundary Conditions 66

3.1.6 Implementation of the fluid properties and additional source terms 67

3.1.7 Particle Tracking Simulation 68

4 RESULTS 70

4.1 Approximation of the dimensionless groups 71

4.2 Thermofluiddynamical non-uniformity during the high pressure treatment 73

4.2.1 Preliminary study and proposed improvements 74

4.2.2 Mesh study 77

4.2.3 Reference case 79

4.2.3.1 Compression phase 80

4.2.3.2 Pressure holding phase 87

4.2.4 Inactivation of enzyme Bacillus subtilis α-Amylase 90

4.2.5 Effects of buoyancy (compensated gravity case) 98

4.2.6 Effects of different length scales 102

4.2.7 Effects of the pressure ramps 109

4.2.8 Effects of the position of the autoclave 114

4.3 Non-uniformity during high pressure inactivation of microorganisms 118

4.3.1 Formulating the inactivation model 119

4.3.2 Temperature distribution and the flow field 124

4.3.3 Non-uniformity of the inactivation process of *L. lactis* 125

4.3.3.1 Milk buffer 126

4.3.3.2 Milk buffer with 1.5 M sucrose 130

4.3.3.3 Milk buffer with 4 M NaCl 133

4.3.3.4 Comparison of predicted data and experimental results 136

5 CONCLUSION 139

6 APPENDIX 146

7 BIBLIOGRAPHY 148

LIST OF NOTATIONS

Symbols

c_p	specific thermal capacity at constant pressure	J/kg K
g	gravitational acceleration	m/s^2
h	specific enthalpy	
m	mass	kg
p	pressure	Pa
T	temperature	K
ΔT	temperature difference	K
t	time	s
V	volume	m^3
$\vec{W}$	velocity vector	m/s
W_0	reference velocity	m/s
∇	nabla operator	
ρ	density	kg/m^3
η	viscosity	kg/m s
α	thermal expansion coefficient	1/K
δ	unit tensor	
β	isothermal compressibility	1/Pa
λ	thermal conductivity	W/m K

Dimensionless numbers

Ar	Archimedes number
Ec	Eckert number
Fr	Froude number

Ga	Galileo number
Gr	Grashof number
Nu	Nusselt number
Pe	Peclet number
Pr	Prandtl number
Ra	Rayleigh number
Re	Reynolds number
$\alpha_0 T_0$	-

Abbreviations

BSA	*Bacillus subtilis* α-Amylase
CFD	Computational Fluid Dynamics
HHP	High Hydrostatic Pressure
HP-DPIT	High Pressure Digital Particle Image Thermography
HP-DPIV	High Pressure Digital Particle Image Velocimetry
HP-CFD	High Pressure Computational Fluid Dynamics
SST	Shear Stress Transport

Sub/superscripts

0	reference property
*	dimensionless property
x, y, z	cartesian coordinates

1 INTRODUCTION

1.1 High Pressure Treatment in Biotechnology

High Pressure Treatment has gained importance in many biotechnological fields. In recent years, it has proved itself as an alternative to the conventional heat treatment, because it provides methods of avoiding off-flavor and deterioration of food components and nutrients, producing unique texture on food, and saving total amounts of energy required for food processing [1]. The range of the proper pressure levels for different processes may vary from as low as 100 MPa to as high as 1000 MPa. Also the pressure holding time can be very short for some products, but amounts up to many hours in some cases.

Although high pressure treatment drastically gained a high interest only in the last decades, the very first research activities in this field were reported as early as in the late 19th century. In the year 1899, Hite [2] could observe a reduction of the microorganisms in the high pressurised milk. A few years later, the Nobel laureate Bridgman reported the irreversible denaturisation of albumen at a pressure level of 700 MPa in [3]. Furthermore, he published [4], in which he studied the thermal conductivity of five different liquids under pressure.

After Bridgman, the research activities in the field of high pressure remained idle for many decades. It is only during the past few years that the high pressure technique became interesting for the industry, and thus led to intensive research activities as seen at present.

In [5] Knorr illustrated the benefits and the possibility using the high pressure technique in the food processing. But he also added that in order to make the most out of this technique, we need a better understanding of this innovative technology, and many studies are still to be carried out.

For instance, it is important for the food industry to study the processing of packed food systems. Although there are still quite few studies carried out in the treatment of packed food, there are some interesting contributions regarding the treatment of the packages. One of these studies was carried out by Lambert et al. [6], who expose many package materials to pressure treatments at different pressure levels.

High pressure can also have a strong influence on many properties of the treated substances. For instance, an interesting issue was studied by Harte et al. [7]. In this study, he compared the yield stress and microstructure of yoghurts made from high pressurised milk, heat treated milk and not treated milk. Particularly, the viscosity and aggregation of β-Lactoglobulin was studied by Baars et al. [8, 9].

Another highly interesting application field of the high pressure technique is the high pressure induced freezing and thawing. Bridgman [10] studied the 5 different types of ice and the phase changes occurring under different pressures and temperatures.

There are many advantages of the high pressure induced freezing and thawing compared to normal freezing and thawing. Most importantly, high pressure induced ice crystals are mostly smaller and more homogeneous in size than those at ambient pressure, and thus lead to less texture damage of the food systems. Le Bail [11] gave a good overview of the influences of the high pressure freezing and thawing on different food systems. Furthermore, there have also been some research activities carried out to examine the behaviour of the freezing and thawing processes under high pressure, like the studies carried out by Özlem et al. [12] and Ferstl et al. [13], who visualised the process of phase changing of ice during the freezing and the thawing process under high pressure with liquid crystals.

Another important application field of the high pressure technique is the inactivation of biological substances like enzymes, microorganisms, diseases or other microbial contaminations at lower temperatures. This leads to a concentration of research activities in medical biotechnology. Masson et al. [14] gave an overview of the possibilities to use high pressure technique in medicine and pharmaceutical science. One good example given in this review article is the high pressure inactivation of biological agents. Since viruses are very sensitive to moderate pressures between 1 and 3 kbar [15, 16, 17], high pressure technology has proven itself to be an attractive alternative to conventional heat treatment. Jurkiewicz et al. [18] have succesfully inactivated immunodeficiency viruses by pressure.

Furthermore, high pressure technology provides the medicine and pharmaceutical science with a powerful tool to develop innovative treatment methods. In the past few years, high pressure gained interest in the development of vaccines against viruses and malignant cells. In particular, Perche et al. [19] successfully developed a vaccine against Rift Valley Fever Virus (RVFV). Mice which were vaccinated with pressure-treated virus were protected against infection by wild-type RVFV.

Another highly interesting issue was studied by Korn et al [20], who tried to inactivate human tumour cells with pressure. They found out that pressures above 300 MPa immediately induced cell death by necrosis and completely inactivated the cells. The cell death caused by necrosis observed during the high pressure treatment is different from that caused by heat, freeze/thaw or chemical agents. Instead high pressure generates a gelatinised mixture of antigens captured in a distinct and robust particle and maintains their immunogenicity. Thus, high pressure is an attractive alternative method to inactivate mammalian cells in clinics or laboratories. Furthermore, there are contributions, where various protein folding phenomena under high pressure are discusses, i. e. Silva et al [21].

The research activity in the field of high pressure inactivation can also be found in food biotechnology, especially the high pressure inactivation of food contaminants. Smelt gave an overview of the recent advances in the microbiology of high pressure processing in [22]. Hinrichs et al. [23] reported the possibility of an ultra-high-pressure inactivation of microbial contaminations in milk and dairy products. Ananta et al. [24], on the contrary, tried to study the kinetics of the high pressure inactivation of *Bacillus* endospores. In order to understand the inactivation process during the high pressure treatment, different research methods have been developed in the past years. For instance, Gänzle et al. [25, 26] developed a system to observe the mechanism of the high pressure inactivation of different cells.

Moreover, the possibility to inactivate enzymes with high pressure has been widely studied during the past years. In particular, the research group of Hendrickx has made a huge leap forward in modelling the inactivation process of many different enzymes under high pressure. For example, Indrawati et al. [27] studied the inactivation of lipoxygenase in green beans at subzero and elevated pressures. Furthermore, Fachin et al. [28] studied the high pressure inactivation of an enzyme called Polygalacturonase (PG), which can be found in Tomatoes. The authors quantified kinetic parameters of this inactivation process under isothermal and isotherm-isobar conditions.

Ludikhuyze et al. [29, 30] and Denys et al. [31, 32] have studied the high pressure inactivation of an enzyme called *Bacillus subtilis* α–Amylase thoroughly. The inactivation rate of this enzyme depends on temperature and pressure. The inactivation mechanism of this enzyme will play an important role in this PhD thesis, thus it will be discussed thoroughly at a later point.

1.2 Process Non-uniformities during the High Pressure Treatment

For many years, high pressure treatment was believed to be a spontaneous and homogeneous process. Delgado and Hartmann [33] shared the opinion that the high pressure process is spontaneous, but the homogeneities of the process must depend on many thermofluiddynamical factors including the temperature increase of the treated substances and the pressure medium. Thus, it is very unlikely that the high pressure process is also homogeneous. The studies carried out by the group Delgado [i.e. 12, 13, 34, 35,] in the past few years have confirmed their assumption.

Pehl [36] and Pehl et al. [37, 38, 39] were the first to examine the dynamic effects of fluid convection and heat transfer in high-pressure processes. They have developed the first in-situ technique to observe thermofluiddynamical processes inside of a high pressure autoclave. In order to gain insight of the autoclave, sapphire window units were installed at the inner wall of the autoclave. Furthermore, they introduced two new techniques called high-pressure digital particle image velocimetry (HD-DPIV) and high-pressure digital particle image thermography (HD-DPIT), which allow the determination of time scales for hydrodynamic and thermal compensation of liquids under high-pressure up to 800 MPa. Both methods work with bio crystals, which reflect against light in different colours indicating the current temperature or other properties of the fluid inside the autoclave (see also Figure 1).

The results from this experimental setup showed a heterogeneous temperature distribution throughout the autoclave. Due to the external work done during the compression phase, the temperature of compressible fluid increases as long as the coefficient of thermal expansion is positive. Thus, heat transfer occurs between the pressure medium, the wall of the autoclave and the treated product leading to a time and space dependent temperature distribution. In the case of liquid food systems, suspended ingredients and microorganisms are subject to transport due to forced and free convection in the direct or indirect process.

However, there have also been publications, in which the authors tried to make use of this pressure-induced temperature increase. De Heij et al. [40], for example, maximised the temperature increase effect with a layer of synthetic material installed at the inside wall of the autoclave, which acts as a heat damping and reduced the heat transfer between the wall and the fluid substantially. This leads to a higher temperature increase and a much more homogeneous temperature distribution in the autoclave [49].

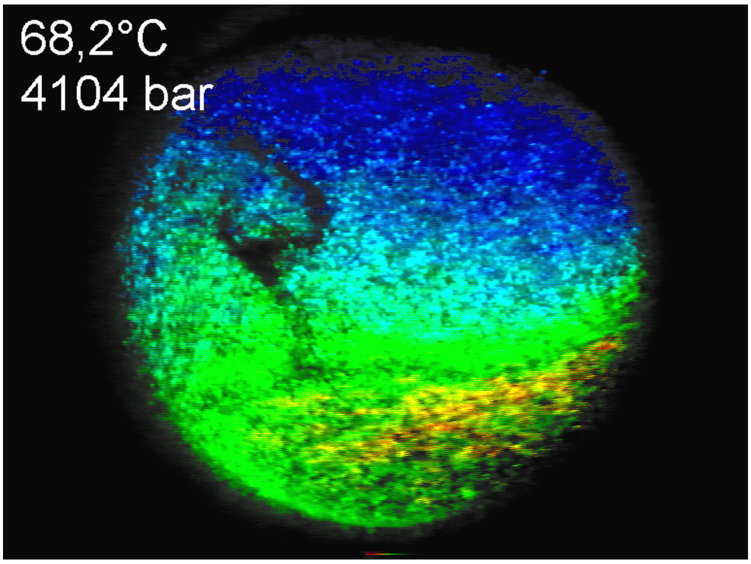

Figure 1: Temperature distribution inside of an autoclave (Pehl et al. 1998)

1.3 Numerical Simulation of High Pressure Processing

Not only in such cases, where real experiments are not possible or very hard to accomplish, numerical simulation plays a vital role as an alternative research methodology. It has made its way to some research activities due to its efficiency and accuracy. Furthermore, in many cases it costs less to do numerical simulation than setting up real experiments. Altogether, numerical simulation is gaining high interest from researchers in many fields of research activities including the high pressure processing.

For instance, Hartmann and Delgado [41] successfully simulated the cell death of a yeast cell under high pressure using the Finite Element technique. The calculated cell death at around 440 MPa represented excellent agreement with experimental results from literature (see also Figure 2).

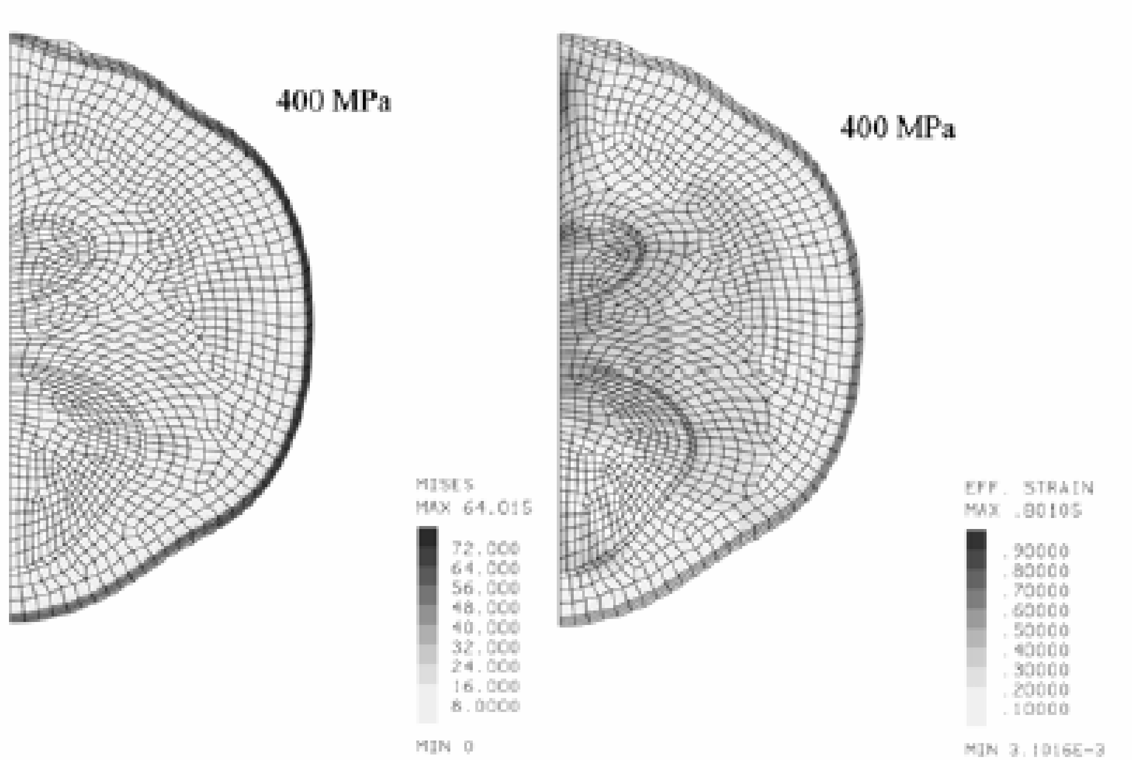

Figure 2: A finite element simulation of a yeast cell at 400 MPa [41]

Another good example for the use of numerical simulation for high pressure treatment is the study carried out by Otero et al. [42]. In this contribution, the authors showed the thermal heterogeneities of fatty food ingredients during a high pressure treatment solving the Fourier heat conduction equation. In [43] the same authors developed a simulation and control method, that enables the study of thermal effects in a real high pressure chamber. Although this method took every single component of a high pressure research unit into account, i.e. the thermal regulation bath, the temper coil, heat conduction across the steel housing of the vessel, it did not represent the spatial distributed quantities inside the vessel but only average quantities. Thus, the effects of thermal heterogeneities on the desired pressure induced mass conversions were not considered.

Although there have been many experimental methods developed for in-situ observations of the high pressure processing, it is still extremely hard, in many cases even impossible, to characterize the thermofluiddynamical and mass conversion processes occurring in a high pressure vessel in real time. The main reason is the wall thickness of the autoclave, which makes it difficult to observe the processes inside of the high pressure chamber. There have been some attempts to measure the temperature with thermocouples at different points inside of the autoclave [44]. The results confirmed temperature heterogeneity during the high pressure treatment. And it is already possible to visualise thermofluiddynamical processes in some small high pressure chambers, where sapphire window units for real time observations are installed, but unfortunately, there are still no studies confronting the visualisation of process heterogeneities inside of larger high pressure chambers as yet.

At the chair of Fluid Mechanics and Process Automation of the Technical University Munich, there is a strong research activity combining the high pressure technique with the finite volume method. Hartmann [45] was the first to simulate thermofluiddynamical processes at higher pressures with distributed quantities as results. His subsequent publications (see [46, 47, 48, 49] for more detail) were dedicated to numerical simulations of thermofluiddynamical and mass conversion processes and the studies of process heterogeneities during high pressure treatments of liquid and packed food systems. The good agreement of his numerical simulations with the experiments carried out by Rademacher [50] confirmed the excellent accuracy of his numerical simulation technique.

Another good example are the studies carried out by Kowalczyk et al. [51, 52, 53, 54], who numerically simulated the process of high pressure freezing and thawing of both liquid and solid food systems. The numerical simulations showed excellent agreement with the experimental results.

In order to make the numerical simulation of the thermofluiddynamical processes during the high pressure processing as realistic as possible, these thermodynamic properties of the high pressure treated substances must be known: density, thermal capacity, thermal conductivity, compressibility, coefficient of thermal expansion and, for fluid system, the transport parameter viscosity.

The properties of the treated substances must be determined experimentally. Such fundamental researches are the most important grounding for successful numerical simulations of the high pressure processing. For instance, Eder et al. [55] have developed a new method to measure the density of the high pressure treated fluid with laser. This method has proven itself to be one of the most accurate density measuring techniques available at present. Another example is the study carried out by Werner et al. [56], who determined the heat conductivity of low viscous liquid food under high pressure.

As water plays both the role of pressure medium and the main “part” of any food, this study will concentrate on the high pressure treatment of aqueous systems. Yet there have been many comprehensive studies on the properties of water at higher pressures in the past years. All these properties gained from the experiments must be modelled and implemented into the numerical simulation in order to ensure the accuracy of the results. The properties of water under high pressure will be thoroughly discussed at a later point of this thesis.

Over the past years, the group of Delgado at the Chair for Fluid Mechanics and Process Automation of the Technical University Munich has been developing methods to implement all these properties into the numerical simulation, resulting in many user routines tha consist of over 6000 commands linked to various interfaces of the main simulation program. This complicated simulation technique will play an extremely important role in this thesis.

1.4 Objectives

This PhD thesis concentrates on the mathematical modelling, numerical simulation and analysis of the process heterogeneities of the high pressure treatment of biological systems. In order to achieve this goal, the following questions must be answered:

- Which thermofluiddynamical processes occur during the compression phase, the holding phase and the release phase of the high pressure treatment?
- What is the contribution of the different terms in the basic equations to the thermofluiddynamical processes?
- How can the temperature distribution of the pressurized fluid be described as a function of time and space during the high pressure treatment?
- What is the velocity field of the treated fluid during the whole high pressure processing?
- How strong is the influence of convection on the homogeneities of the process?
- Can the temperature distribution of the inside wall be mathematically described?
- Which influence does the temperature distribution of the inner wall have on the temperature distribution of the pressurized fluid?

Particularly during implementation of mass conversion models like inactivation models, there are some numerical problems to be solved, for instance:

- How can the mass conversion be mathematically described?
- Which influence does the mass conversion have on mass transport?
- How can other source terms, which enable numerical description of the mass conversion, be added to the equations and implemented onto the model?

Moreover, under some circumstances turbulences can exist in bigger autoclaves due to higher inflow velocities needed for a faster pressure ramp. The existence of turbulence influences the velocity field and the temperature distribution of the pressure medium, and therefore, leads to an alteration of mass conversion in biological systems. In the past decades, significant progresses could be made in the numerical analysis of turbulence particularly by the group of Friedrich [i.e. 57, 58, 59, 93]. However, the effect of turbulence on high pressure has not been considered in the literature yet. In order to enable a correct numerical solution, there questions are to be answered:

- How can turbulence be generated during the high pressure processing?
- Which turbulence model suits the numerical simulation of a high pressure treatment the most?
- What influences can turbulence have on the velocity field and the temperature distribution of the fluid?
- What is the influence of turbulence on mass conversion?

Last but not least, it should also be shown at a later point of this thesis, how the heterogeneities can be reduced. All the results shown in this thesis should contribute to an intelligent process design for high pressure treatments in the future. Especially, the scale-up effect and the transferability of experiments made in the lab-scale high pressure units to larger industrial sized high pressure vessels should be examined intensively.

2 THEORETICAL CONSIDERATIONS TO MODELLING AND SIMULATION OF THE HIGH PRESSURE PROCESSING

In order to model the thermofluiddynamical processes during the high pressure treatment of biological substances, some theoretical considerations must be made. Especially the problems of how to enable the finite volume code used to calculate the compression of the fluid will be discussed in detail. In this work, water is chosen as the pressure fluid due to the completeness of the data considering its characteristics under high pressure. Furthermore, water is one of the most often used pressure media and represents the largest “part” of most foods. In this context, thermofluiddynamical properties of water under high pressure will be explained first. Subsequently, the fundamental thermodynamic and fluiddynamic equations solved in this thesis shall be shown and explained in detail.

Moreover, the existence of turbulent flows during the high pressure treatment should also be examined. Especially the interactions of the turbulent free shear flows, which are caused by the compression process, with the free convection inside the autoclave are of great interest. Therefore, the methods used for the turbulence modelling shall be described shortly.

Last but not least, in order to characterise the importance of each thermofluiddynamical sub-process during the high pressure treatment, dimensionless studies of the thermofluiddynamical equations solved during the simulation of the high pressure treatment will be carried out. Especially the possibility of neglecting less important terms of the solved equations in order to reduce computational costs and time shall be examined.

2.1 Physical Properties of Liquid Water under High Pressure

Water has been a subject of a large body of publications, see e.g. [60, 61, 62]. Thus, only the most remarkable properties in connection with the high pressure treatment can be considered here. Generally, a water molecule is visualized as V-shaped, with two hydrogens attached to an oxygen atom at a 104.5° angle. However, water molecules can also be visualized as tetrahedrons, with the oxygen atom in the middle (see also Figure 3). Two of the corners are hydrogen atoms and the other two are so called "lone-pairs" of electrons. Although most liquids are held together by van der Waals forces between the molecules, water is primarily held together by hydrogen-bonds between hydrogens and lone-pairs [63]. The hydrogen bonds are approximately ten times stronger than van der Waals forces, but only a tenth as strong as the covalent bond holding hydrogen to oxygen. Both the van der Waals forces and the hydrogen bonds will play an important role in explaining the characteristics of water under high pressure.

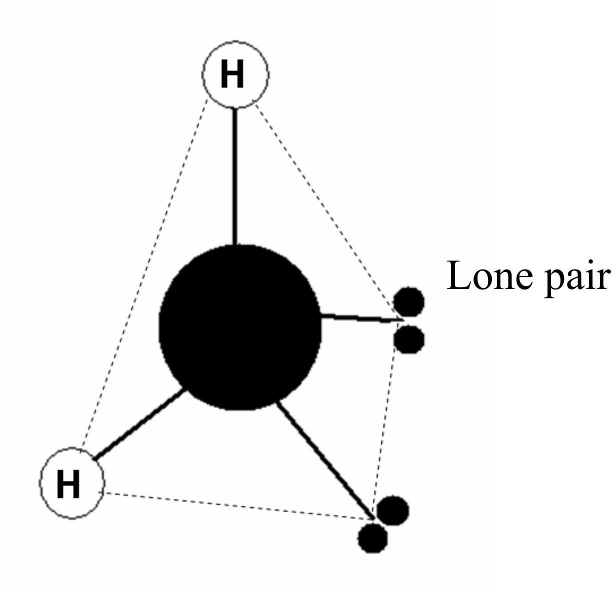

Figure 3: A model of a water molecule

At higher pressures, however, the properties of liquid water differ from those at ambient condition significantly (see also Figure 4).

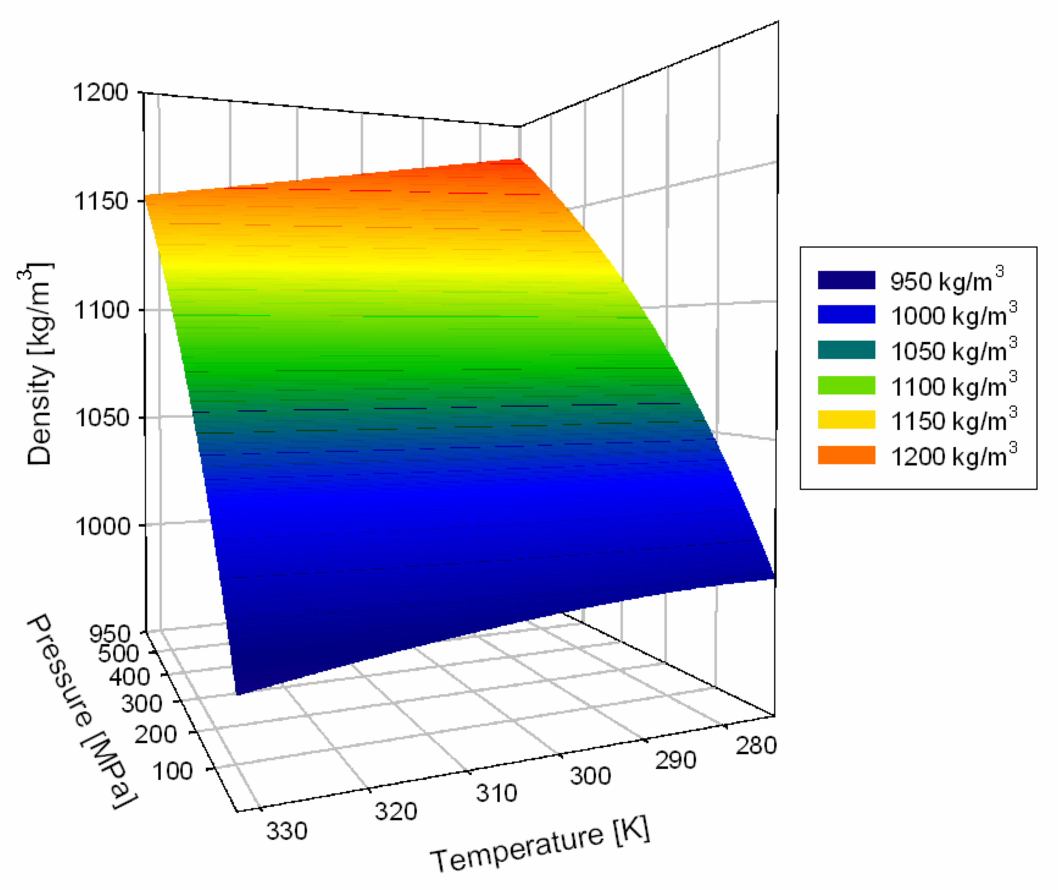

Figure 4: Density in dependence of temperature and pressure [83]

The density of liquid water depends mainly on the cohesive nature of the hydrogen-bonded network. At temperatures higher than this, density of liquid water decreases with increasing temperature due to thermal expansion. The density maximum of 1000 kg/m^3 at ambient pressure is due to the opposing effects of increasing temperature, causing both structural collapse that increases density and thermal expansion that lowers density. However, when liquid water is put under pressure (below about 200 MPa) the water molecules approach their neighbors more closely and the distances between the water molecules become smaller, as might be obvious from the density increase. However, if the pressure is about 200 to 400 MPa, the average distance between neighboring water molecules increases [64] (see also Figure 5). In the pressure range above 400 MPa the distances between the water molecules reduce again slightly with increasing pressure. A similar and corroborative behavior is seen with the O-H stretch vibration frequency (v1), which increases with pressure between about 200 to 400 MPa [65] whilst reducing with pressure at higher or lower pressures. The possible explanation for these effects is an increase in interpenetration of hydrogen bonded networks at about 200 MPa (at 290 K); interpenetration of hydrogen bonded clusters being preferred over more extreme bending or breaking of the hydrogen bonds. The 200 MPa pressure also marks the extreme pressure that the density maximum can occur. Although pressure will increase the density of water at all temperatures, it will have a disproportionate effect at lower temperatures. Thise results in a shift in the temperature of maximum density to lower temperatures. At high enough pressures the density maximum is shifted to below 0°C (~20 MPa) and, at above 200 MPa, and thus, cannot be observed anymore.

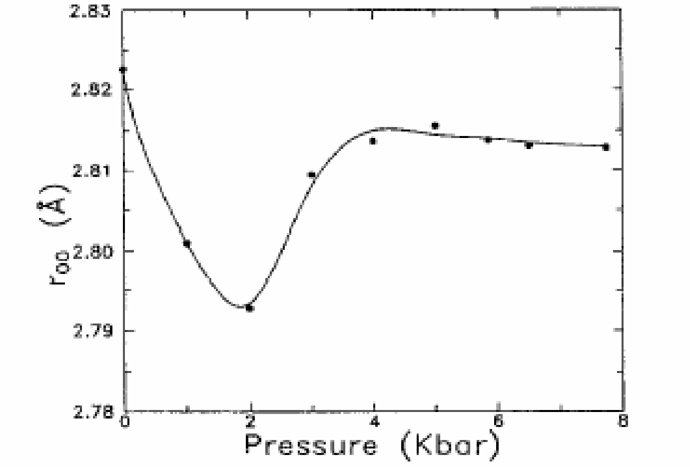

Figure 5: The pressure dependence of the separation between the nearest molecules [64]. In this picture r_{OO} is given in Ångström (1 Å= 10^{-10} m).

Another important fluid property is the thermal capacity, defined as the amount of energy that a mass unit of a substance can absorb. As water consists of light molecules, there are more molecules per gram, which can absorb the same amount of energy, than in similar fluids. Therefore, water has the largest thermal capacity at constant pressure (c_P) of all liquids except ammonia. Furthermore, this unusually large specific thermal capacity of water is also strongly related to the strength of the hydrogen bonds between the water molecules. However, as the hydrogen bonds are disturbed at high pressures, this leads to a decrease of the specific heat capacity with increasing pressure level (see also Figure 6).

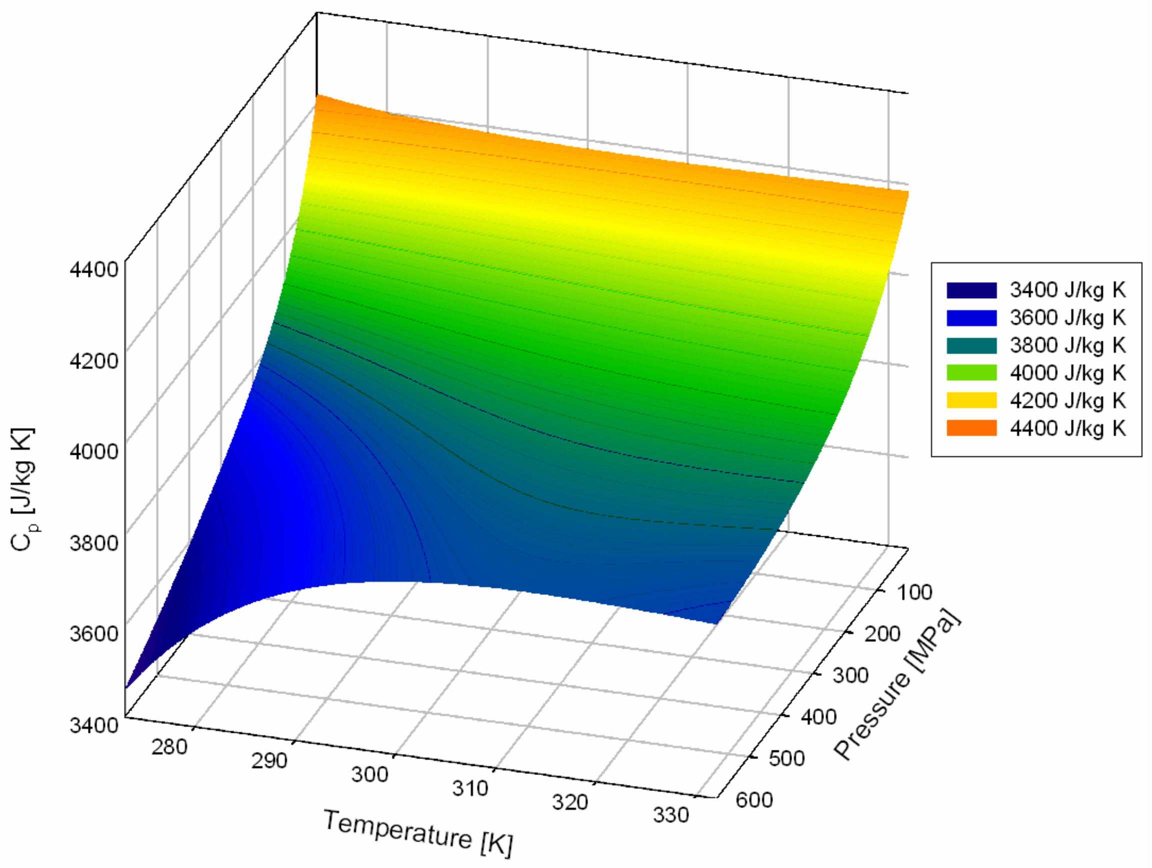

Figure 6: Thermal capacity in dependence of temperature and Pressure [83]

Last but not least, the rheological material parameters of the fluid must also be considered. The most investigated material parameter is the viscosity. In general, the viscosity of water decreases as the temperature increases. This is also due to weaker hydrogen bonding at higher temperatures. On the other hand, as the pressure increases, the volume decreases and the volume of the voids between the molecules reduces, so normally increasing the viscosity. However, at pressures lower than 150 MPa, viscosity minima can be observed. This pressure-viscosity behavior of water can be explained by the increased pressure causing deformation, thus reducing the strength of the hydrogen-bonded network, which is also partially responsible for the viscosity [66]. However, this reduction in cohesivity more than compensates for the reduced void volume. Thus, it is a direct consequence of the balance between hydrogen bonding effects and the van der Waals dispersion forces in water [67]. At higher pressures (and densities), the balance between hydrogen bonding effects and the van der Waals dispersion forces is tipped in favor of the dispersion forces. However, the remaining hydrogen bonds are stronger due to the closer proximity of the contributing oxygen atoms [68]. Thus, viscosity increases with pressure anyway (see also Figure 7).

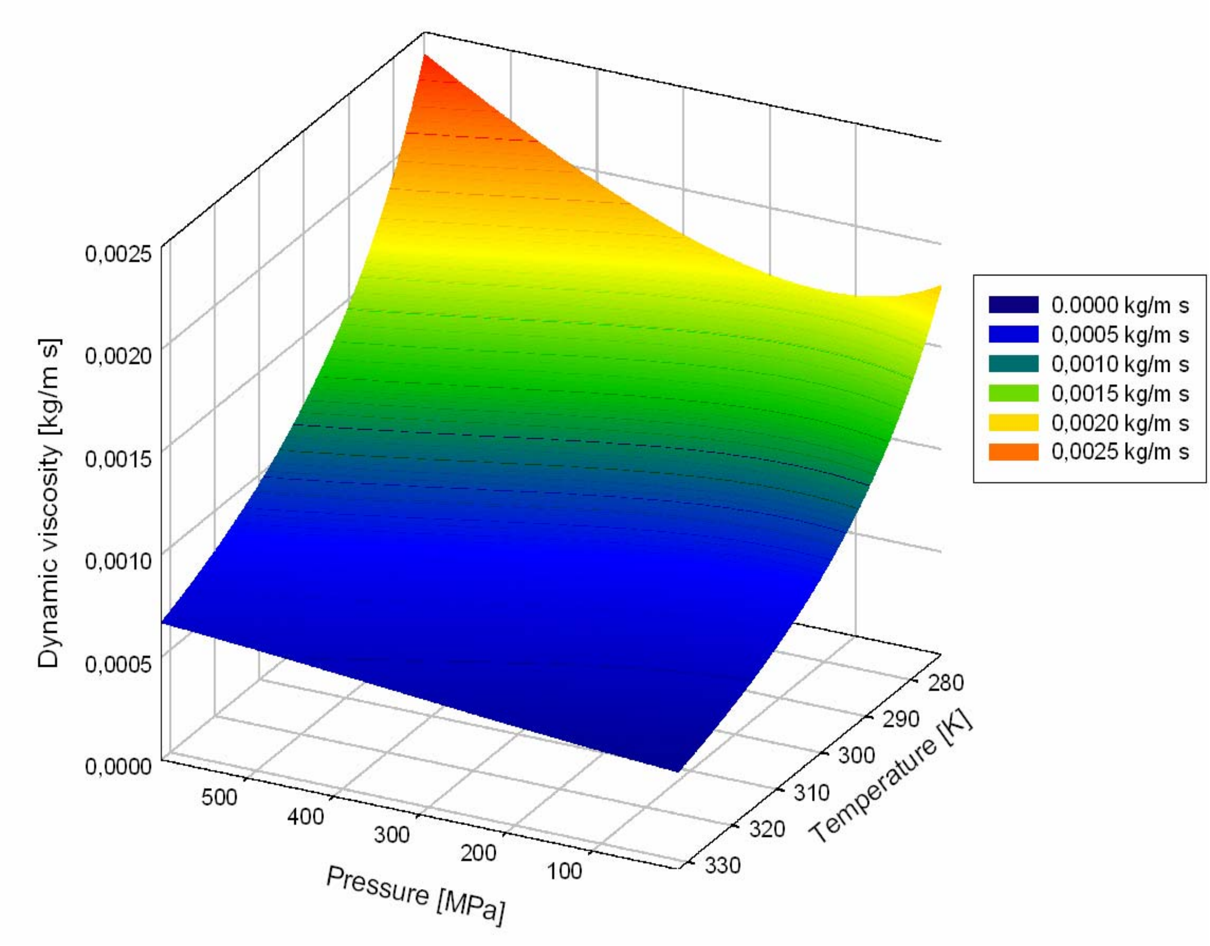

Figure 7: Dynamic viscosity in dependence of temperature and pressure [84, 85, 86]

2.2 Equilibrium Thermodynamics of Water as a homogeneous system

In this work, water is used as the pressure fluid. However, the compression of the fluid is always accompanied by thermodynamic processes, especially the pressure-induced thermal expansion of water during the high pressure treatment. Thus, the thermodynamics of water must be explained briefly. More details are given in the literature, e.g. [54, 69, 77, 80].

One of the most important state variables is the internal energy (U), which is an extensive state quantity and means the total energy of a system due to the random, disordered motion of molecules, plus the rotation, and vibration of atoms within molecules. Heat and work serve as for adding energy to or subtracting energy from a system. They represent energy in transit and are the terms used when energy is moving. Thus, in terms of the amount of heat dQ, work dW and change of internal energy dU, the first law of thermodynamics can be written as:

$$dU = dQ + dW \,. \tag{2.1}$$

Hence, with

$dQ = TdS$ for irreversible processes and (2.2)

$dW = -pdV$ for external work (2.3)

the change of the specific internal energy of a thermodynamic system can be written as:

$$dU = T\ dS - p\ dV \,. \tag{2.4}$$

Hereby, T represents the temperature, S the entropy, p the pressure, and the volume is denoted by V. The equation 2.4 can be rewritten in a specific form as:

$$du = T\ ds - p\ dv \,. \tag{2.5}$$

Additionally to u in thermodynamics, the (non conservative) specific enthalpy h is often introduced for convenience. In this context h is then a precisely measurable state variable, since it is defined in terms of three other precisely definable state variables, the specific internal energy u, pressure p and specific volume v, and can be described as:

$$h = u + pv = u + \frac{p}{\rho} \,. \tag{2.6}$$

Through differentiation of the equation (2.6) and substitution in the equation (2.5), the relation between the specific enthalpy and other thermodynamic parameters can be described as:

$$dh = T\ \ ds + v\ dp \,. \tag{2.7}$$

As h depends on s and p, and dh can be written as a total differential, which must fulfill the requirement:

$$df = a\,dx + b\,dy\text{, where } a = \left.\frac{\partial f}{\partial x}\right|_y \text{ and } b = \left.\frac{\partial f}{\partial y}\right|_x . \tag{2.8}$$

Therefore, dh can be rewritten in as a complete differential equation:

$$dh = \left.\left(\frac{\partial h}{\partial T}\right)\right|_p dT + \left.\left(\frac{\partial h}{\partial p}\right)\right|_T dp\ . \tag{2.9}$$

Furthermore, the specific thermal capacity at constant pressure is hence defined:

$$c_p = \left.\left(\frac{\partial h}{\partial T}\right)\right|_p . \tag{2.10}$$

The second term of the equation (2.9) is important for the temperature increase in the high pressure treatment and will be discussed at a later point. The equations (2.5) – (2.9) altogether with the equation for Gibb's free energy:

$$G = H - T \cdot S \tag{2.11}$$

and the free energy *A* (also called Helmholtz energy)

$$A = U - T \cdot S \tag{2.12}$$

are used to describe the thermodynamic processes and the derivation of Maxwell's equations. Through the differentiation of the equations (2.11) and (2.12), additional equations could be derived as follow:

$$\begin{aligned} dG &= dH - T \cdot dS - S \cdot dT \\ &= T \cdot dS + V \cdot dp - T \cdot dS - S \cdot dT \\ &= -S \cdot dT + V \cdot dp \end{aligned} \tag{2.13}$$

$$\begin{aligned} dA &= dU - T \cdot dS - S \cdot dT \\ &= T \cdot dS - p \cdot dV - T \cdot dS - S \cdot dT \\ &= -S \cdot dT - p \cdot dV \end{aligned} \tag{2.14}$$

The equations (2.5), (2.13) and (2.14) must also fulfill the requirement shown in equation (2.8). Thus, the following relations can be obtained:

$$\left(\frac{\partial U}{\partial S}\right)\bigg|_V = T \quad (2.15) \qquad \left(\frac{\partial U}{\partial V}\right)\bigg|_S = -p \quad (2.16)$$

$$\left(\frac{\partial A}{\partial V}\right)\bigg|_T = -p \quad (2.17) \qquad \left(\frac{\partial H}{\partial p}\right)\bigg|_S = \left(\frac{\partial G}{\partial p}\right)\bigg|_T = V \quad (2.18)$$

$$\left(\frac{\partial H}{\partial S}\right)\bigg|_p = T \quad (2.19) \qquad \left(\frac{\partial A}{\partial T}\right)\bigg|_V = \left(\frac{\partial G}{\partial T}\right)\bigg|_p = -S \quad (2.20)$$

Furthermore, these thermodynamic relations can be rewritten as Maxwell's equations [69]:

$$\left(\frac{\partial T}{\partial V}\right)\bigg|_S = -\left(\frac{\partial p}{\partial S}\right)\bigg|_V , \qquad (2.21)$$

$$\left(\frac{\partial T}{\partial p}\right)\bigg|_S = -\left(\frac{\partial V}{\partial S}\right)\bigg|_p , \qquad (2.22)$$

$$\left(\frac{\partial p}{\partial T}\right)\bigg|_V = \left(\frac{\partial S}{\partial V}\right)\bigg|_T , \qquad (2.23)$$

$$\left(\frac{\partial V}{\partial T}\right)\bigg|_p = -\left(\frac{\partial S}{\partial p}\right)\bigg|_T . \qquad (2.24)$$

In order to study the temperature increase during the compression, the 2nd term of the equation (2.9) is of great importance (see also Zemansky [70]):

$$\left(\frac{\partial h}{\partial p}\right)\bigg|_T = v - T\left(\frac{\partial v}{\partial T}\right)\bigg|_p . \qquad (2.25)$$

With the thermal capacity c_p (see also equation (2.10)) and the thermal expansion coefficient

$$\alpha = \frac{1}{v}\left(\frac{\partial v}{\partial T}\right)\bigg|_p = -\frac{1}{\rho}\left(\frac{\partial \rho}{\partial T}\right)\bigg|_p \text{ (ρ represents the density),} \qquad (2.26)$$

which describes the relative volume change during a temperature increase at constant pressure, following equation can be derived:

$$ds = \frac{1}{T} c_p \; dT - \alpha \; v \; dp \; . \tag{2.27}$$

In isentropic cases where ds = 0, the following relation must be fulfilled for a closed system:

$$\frac{1}{T} c_p \; dT = \alpha \; v \; dp \; . \tag{2.28}$$

In the end, the temperature increase of the pressure medium in isentropic cases can be described as follow:

$$\left.\left(\frac{dT}{dp}\right)\right|_S = \frac{\alpha T v}{c_p} = \frac{\alpha T}{\rho c_p} \, . \tag{2.29}$$

In order to calculate the adiabatic temperature increase at a given pressure, the previous equation is rewritten in

$$\frac{dT}{T} = \frac{\alpha}{\rho c_p} dp \; . \tag{2.30}$$

In the literature [80], it is shown that

$$\frac{\alpha}{\rho c_p} \approx const = k \; . \tag{2.31}$$

Therefore, by solving the differential equation (2.30), the following equation can be obtained:

$$\ln\left|\frac{T}{T_0}\right| = k \cdot p = \frac{\alpha}{\rho c_p} p \;\; \text{with } T_0 \text{ as the start temperature.} \tag{2.32}$$

Therefore, the adiabatic temperature can be calculated with

$$T_{ad} = T_0 \cdot e^{k \cdot p} = T_{0.} e^{\frac{\alpha}{\rho c_p} p} \; . \tag{2.33}$$

And the adiabatic temperature increase can be described as

$$(\Delta T)_{ad} = T_{ad} - T_0 = T_0 \left(e^{\frac{\alpha}{\rho c_p} p} - 1 \right) . \tag{2.34}$$

Additionally, the volume change due to pressure increase at constant temperature is described as

$$\beta = -\frac{1}{v}\left(\frac{\partial v}{\partial p}\right)\bigg|_T = \frac{1}{\rho}\left(\frac{\partial \rho}{\partial p}\right)\bigg|_T . \tag{2.35}$$

Taking a closer look at equation (2.29), it is obvious that the temperature increase during the compression strongly depends on the properties of the compressed material. During the compression, the temperature increase of the fluids with smaller thermal capacity and larger thermal expansion coefficient like oils or alcohols must be higher than those of fluids with larger thermal capacity, i.e. water. In general, the temperature of water increases by approx. 2 – 3 K per 100 MPa in the isentropic case. At the start temperature of 313 K, for instance, the adiabatic temperature increase of water at 500 MPa amounts up to 14.8 K according to the equation (2.34).

However, the high pressure process cannot always be considered isentropic, because thermofluiddynamical processes take place between the fluid inside of the autoclave, the inflowing fluid and the wall of the autoclave itself. The temperature increase (dT/dp) calculated with equation (2.34) can be considered as the maximum one and can only be reached under isentropic conditions. Due to heat transfer, the temperature distribution remains heterogeneous at all time during the high pressure treatment. Thus, the problem is spatial and transient, making the numerical simulation a suitable solution for this work.

2.3 Introductory Remarks to Computational Fluid Dynamics (CFD)

Computational Fluid Dynamics is a term representing a variety of numerical techniques used to solve the equations that govern fluid flows (see [71] for more details). The set of equations solved in CFD-simulations include equations of conservation of mass, energy and momentum of the fluid. Particularly for Newtonian fluids, the Navier-Stokes equations, which represent a set of partial differential equations that was derived in the early nineteenth century, are solved. Although there are some analytical solutions of the Navier-Stokes equations in very few applications, no general analytical solutions of the Navier-Stokes equations have been found as yet. But these can be discretised and solved numerically. The numerical methods used to solve the Navier-Stokes equations can be found in the literature, e.g. [72, 73, 74]. Additionally, equations describing other processes, such as combustion or other chemical reactions, can also be solved in conjunction with the Navier-Stokes equations. Modern CFD results can rival the accuracy of experiments and must be considered as alternatives to experiments not only in such cases, where experiments are too costly, too dangerous or too difficult to carry out.

There are different discretization methods which are used in CFD codes such as the Finite Element method, the Finite Difference method and the Boundary Element method. However, the most common and most widely used is known as the Finite Volume technique. In this technique, the region of interest is divided into small sub-regions, called control volumes. The equations are then discretized and solved for each control volume. As a result, an approximation of the value of each variable at specific points throughout the domain can be obtained. In this way, one derives a full picture of the behavior of the flow. The iterative approach is required here due to the non-linear nature of the equations to be solved. As the numerical solution approaches the exact solution, the simulation is said to converge. For each iteration, an error, or residual, is reported as the measure of the overall conservation of the flow properties.

The accuracy of the CFD model depends on many factors including the size and the shape of the control volumes and the magnitude of the final residuals. More complex physical processes, for instance turbulence, are often modelled using additional empirical relationships. However, the approximants inherent in these models also contribute to deviations between the CFD solution and the real flow.

In the literature, there are reports on numerical simulations of compressible fluids, particularly by the group of Friedrich [75, 76]. However, there are only few contributions concerning the numerical simulations of compressible liquids under high pressure. Therefore, the fundamental equations solved in the simulations of the high pressure treatment shall be discussed in detail. The most important background of this work is the PhD thesis of Kowalczyk [54], who summarized, affiliated and discussed the equations needed for the calculations of the high pressure treatment.

Most importantly, Kowalczyk presented the equations to be solved during the simulations in their dimensionless forms. However, due to differences in the definitions of some dimensionless groups in this work from the original work of Kowalczyk, the equations shown in [54] cannot be taken without changes. Thus, it is necessary to rewrite all the equations in their dimensionless forms once again. In this chapter, the fundamental equations will be shown and their dimensionless forms shall be shown in chapter 2.4.

2.3.1 Conservation of Mass

The conservation of mass is a fundamental concept of physics along with the conservation of momentum and energy. All the three laws of conservation are explained in detail in the literature, i. e. [77, 78, 79, 80]. The conservation of mass itself, in its most compact form, states that matter (or mass) in a system of substance is neither created nor destroyed. Although Albert Einstein announced his discovery of the equation $E = mc^2$ and, as a consequence, the two laws of mass and energy conservations were merged into the Law of Conservation of Mass-Energy, the high pressure processing is not affected by this, and the conservation of mass is still valid here, as the high pressure process does not create or destroy atoms, or change one kind of atom into another.

The mass conservation equation for a homogeneous pure medium

$$\frac{\partial \rho}{\partial t} + \nabla \bullet \left(\rho \vec{W} \right) = 0 \tag{2.36}$$

describes the transient change of the mass in a fixed control volume as the difference between the ingoing and outgoing mass flow.

2.3.2 Conservation of Momentum

The conservation of momentum

$$\frac{\partial \rho \vec{W}}{\partial t} + \nabla \bullet \left(\rho \vec{W} \otimes \vec{W} \right) = \nabla \bullet \hat{T} + \vec{F}\,, \tag{2.37}$$

describes the transient momentum change in a control volume as the difference between the momentum of the ingoing and outgoing fluid in a cell of constant volume and the sum of the forces upon the control volume itself. It is possible to distinguish two kinds of forces which act on the matter: 1) long-range forces like gravity which decrease slowly with increase of distance; 2) short-range forces, which have a direct molecular origin.

Long range forces act on all elements of the fluid. Gravity is the obvious and most important example. A consequence of the slow variation of long-range forces with position is that the force acts equally on all the matter within a small fluid element and the total force is proportional to the size of the volume element. Long-range forces are also called volume or body forces. The only specific volume force found in the case of the high pressure processing is the gravity with the term:

$$\vec{F} = \rho \cdot \vec{g}\,, \tag{2.38}$$

where $\vec{g}$ represents the acceleration due to gravity.

Short-range forces, also called surface forces, of direct molecular origin decrease rapidly with increase of distance between interacting elements, and are significant only when that distance is of the order of the molecular separation. They are negligible unless there is direct mechanical contact between the interacting elements, as in the case of the reaction between two rigid bodies, because without that contact none of the molecules of one of the elements is sufficiently close to a molecule of the other element. In the case of a liquid the situation is more complex because there are contributions to the short-range or contact forces from transport of momentum across the common boundary by molecules in oscillatory motion about some quasi-stationary position and from the forces between molecules on the two sides of the common boundary; both these contributions have large magnitude, but they act approximately in opposite directions and their resultant normally has a much smaller magnitude than either.

In the high pressure processing of a homogeneous, chemically and electrically inert medium the most important surface forces are frictional forces and the pressure itself. These two forces must be included in the model.

The stress tensor $\hat{T}$ shown in equation (2.37) can be described as:

$$\hat{T} = -p\delta + \tau\,, \tag{2.39}$$

with the frictional tension tensor for Newtonian fluids τ

$$\tau = \left(\zeta - \frac{2}{3}\eta \right)\left(\nabla \bullet \vec{W}\right)\delta + \eta\left(\nabla\vec{W} + \left(\nabla\vec{W}\right)^T\right) \tag{2.40}$$

as η represents the dynamic viscosity and ζ the volume (or bulk) viscosity

$$\zeta = \eta' + \frac{2}{3}\eta , \tag{2.41}$$

which is responsible for the energy dissipation in a fluid of smooth temperature distribution due to a finite change in volume. Therefore, the bulk viscosity is another physical property of a compressible isotropic Newtonian fluid.

The assumption of the Stokes hypothesis states that the thermodynamic pressure is equal to the value of the invariant “one third of the sum of the normal stresses”, even if finite compression and expansion takes place. Therefore, according to the Stokes hypothesis

$$\eta' = -\frac{2}{3}\eta , \tag{2.42}$$

so that ζ disappears (see also [77]).

In order to determine under what conditions this assumption holds, experimental investigations must be carried out. However, the measurement of bulk viscosity is difficult to carry out, and there are yet no reliable results. There are statistical methods for high density gases, which are not so well developed that they yield useful insights into these problems. It is also probable that the bulk viscosity vanishes for low density gases, i. e. under conditions where only binary collision occur. In dense gases, the numerical value of the bulk viscosity seems to be very small [88]. However, in processes where the relaxation processes are due to local deviations from chemical equilibrium [81, 82], the Stokes hypothesis does not hold, and the thermodynamic pressure no longer equals one third the sum of the main diagonal elements of the stress tensor.

In this work, due to the lack of the data concerning the bulk viscosity of water under high pressure, the Stokes hypothesis is assumed, so that the momentum conservation equation becomes

$$\frac{\partial \rho \vec{W}}{\partial t} + \nabla \bullet \left(\rho \vec{W} \otimes \vec{W} \right) = -\nabla p + \nabla \bullet \tau + \rho \vec{g} \, . \tag{2.43}$$

2.3.3 Conservation of Energy

In this work, the energy equation is used in the enthalpy formulation.

$$\frac{\partial \rho h_{tot}}{\partial t} - \frac{\partial p}{\partial t} + \nabla \bullet \left(\rho \vec{W} h_{tot} \right) = \rho \vec{g} \bullet \vec{W} + \nabla \bullet \left(\lambda \nabla T \right) + \nabla \bullet \left(\tau \bullet \vec{W} \right). \tag{2.44}$$

The term $\rho \vec{g} \bullet \vec{W}$ represents the temporal energy rate gained due to the gravitational forces, and heat flux is described with the term $\nabla \bullet \left(\lambda \nabla T \right)$. The third term results from the work done by the viscous forces.

Herein, h_{tot} is defined as the specific total enthalpy, which is given in terms of the specific static enthalpy, h by:

$$h_{tot} = h + \frac{1}{2} W^2 . \tag{2.45}$$

And with equation (2.9), (2.10) and (2.25) the enthalpy equation can be rewritten as

$$dh = c_p dT + \left[\nu - T \left(\frac{\partial \nu}{\partial T} \right) \bigg|_p \right] dp. \tag{2.46}$$

Together with

$$\nu = \frac{1}{\rho} \text{ and} \tag{2.47}$$

$$d\nu = -\frac{1}{\rho^2} d\rho \tag{2.48}$$

The enthalpy equation can be written in dependency of temperature and density of the fluid as

$$dh = c_p dT + \frac{1}{\rho} \left[1 - \frac{T}{\rho} \left(\frac{\partial \rho}{\partial T} \right) \right] dp. \tag{2.49}$$

Using equation (2.49) together with the thermal expansion coefficient

$$\alpha = -\frac{1}{\rho}\left(\frac{\partial \rho}{\partial T}\right)_p \tag{2.50}$$

the energy equation can then be rewritten as

$$c_p \rho \frac{DT}{Dt} = \alpha T \frac{Dp}{Dt} + \nabla \bullet \left(\lambda \nabla T\right). \tag{2.51}$$

If dissipative effects such as viscous work are significant, then an additional term is added to the right hand side of the equation of the energy to account for the effect of the viscous shear. Hence the energy equation becomes:

$$c_p \rho \frac{DT}{Dt} = \alpha T \frac{Dp}{Dt} + \nabla \bullet \left(\lambda \nabla T\right) + \eta \Phi \ , \tag{2.52}$$

with the dissipation function Φ, and its form in rectangular three dimensional coordinates is

$$\begin{aligned}\Phi = 2&\left[\left(\frac{\partial W_x}{\partial x}\right)^2 + \left(\frac{\partial W_y}{\partial y}\right)^2 + \left(\frac{\partial W_z}{\partial z}\right)^2\right] \\ &+ \left(\frac{\partial W_x}{\partial y} + \frac{\partial W_y}{\partial x}\right)^2 + \left(\frac{\partial W_x}{\partial z} + \frac{\partial W_z}{\partial x}\right)^2 + \left(\frac{\partial W_y}{\partial z} + \frac{\partial W_z}{\partial y}\right)^2 \\ &- \frac{2}{3}\left(\frac{\partial W_x}{\partial x} + \frac{\partial W_y}{\partial y} + \frac{\partial W_z}{\partial z}\right)^2 .\end{aligned} \tag{2.53}$$

At this point, there are 8 variables $\left(W_x, W_y, W_z, p, T, \rho\right)$ and the material properties c_p, η, λ in the 5 conservation equations (2.36), (2.43 in 3 dimensions) and (2.52). But the set can be closed by adding several algebraic thermodynamic equations: the thermal Equation of State describing the density as function of pressure and temperature; and the Caloric Equation relating the enthalpy to the temperature and pressure. Furthermore, a formulation for viscosity of water under high pressure must also be implemented.

For this PhD thesis, the water data under high pressure is taken from the literature. An equation of state for water under high pressures up to 2500 MPa is taken from the contribution of Saul and Wagner [83], which describes the density and the specific heat capacity of water as functions of pressure and temperature. By fitting the Helmholtz function to several kinds of experimental data including density and thermal capacity, the authors developed two models, a regular model with 58 coefficients and a “fast” solution with 38 coefficients. Here, the regular model with 58 coefficients is favored due to its higher accuracy.

Furthermore, the dependency of the viscosity on pressure and temperature was studied thoroughly by Watson, Basu and Sengers [84] and Förster [85, 86]. The data from these distributions acted as a basis for the development of a pressure-temperature-viscosity model, which is implemented in the numerical models as well.

2.4 Dimensionless equations for the high pressure treatment

The combined temperature-high pressure treatment normally takes place in a so-called high pressure autoclave. In many cases, tempering mechanisms are installed at the outer wall of the autoclave. The high pressure processing itself consists of 3 steps: compression, pressure holding, and decompression. On the one hand, during compression and the decompression the motion of the fluid in the autoclave is dominated by the forced convection due to the free jet of the fluid pumped into and out of the autoclave by the pressure pump or a pressure intensifier. On the other hand, free convection dominated throughout the pressure holding phase due to the cooling process taking place at the inner wall of the autoclave.

An example of the geometry of the inner volume of an autoclave is shown in Figure 8. Due to the rotational symmetry found in most of the autoclaves, the equations for the 2-dimensional system will be considered.

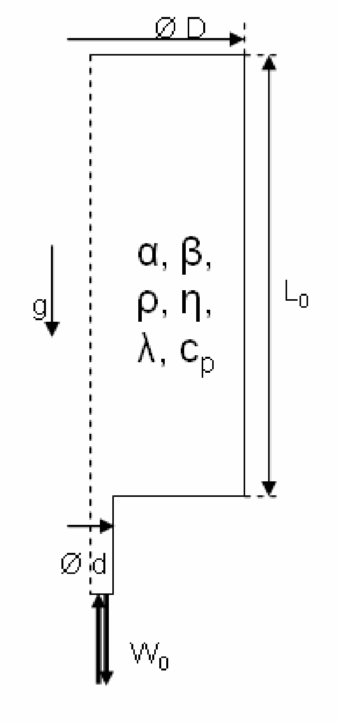

Figure 8: High pressure autoclave with characteristic parameters

Last but not least, the pressure of the system can be described as the sum of the hydrostatic and dynamic pressure as follow:

$$p = p_{stat} + p_{dyn}, \tag{2.54}$$

with

$$p_{dyn} = \frac{1}{2}\rho W^2 . \tag{2.55}$$

2.4.1 Fundamental dimensionless equations

In order to transform the equations to their dimensionless forms, dimensionless variables are introduced. During the compression, the inlet velocity W_0 is considered as the characteristic velocity. Furthermore, in the x-direction the length of the autoclave L_0 is considered as the characteristic length. Thus, following dimensionless variables are defined:

$$x^* = \frac{x}{L_0} = 0(1), \tag{2.56}$$

$$t^* = \frac{t\,W_0}{L_0}, \tag{2.57}$$

$$W_x{}^* = \frac{W_x}{W_0} = 0(1). \tag{2.58}$$

The inner diameter of the autoclave is chosen as the characteristic length of the y-direction. Thus, the dimensionless length scale in the y-direction can be described as:

$$y^* = \frac{y}{D} = 0(1). \tag{2.59}$$

With equations (2.56), (2.57), (2.58) and the continuity equation

$$\frac{\partial W_x}{\partial x} + \frac{\partial W_y}{\partial y} = 0, \tag{2.60}$$

can be rewritten as:

$$\frac{W_0}{L_0}\frac{\partial W_x^*}{\partial x^*} + \frac{1}{D}\frac{\partial W_y}{\partial y^*} = 0. \tag{2.61}$$

After multiplying the previous equation with $\frac{L_0}{W_0}$, this equation takes the form:

$$\frac{\partial W_x^*}{\partial x^*} + \frac{L_0}{D W_0}\frac{\partial W_y}{\partial y^*} = \frac{\partial W_x^*}{\partial x^*} + \frac{\partial W_y^*}{\partial y^*} = 0. \tag{2.62}$$

Thus, it becomes obvious that

$$\frac{L_0}{D W_0}\frac{\partial W_y}{\partial y^*} = \frac{\partial W_y^*}{\partial y^*}. \tag{2.63}$$

The dimensionless velocity in the y-direction of the system can then be described as:

$$W_y^{\ *} = \frac{W_y L_0}{W_0 D} = 0(1) . \tag{2.64}$$

Furthermore, the dimensionless density is defined as:

$$\rho^* = \frac{\rho}{\rho_0} = 0(1) . \tag{2.65}$$

2.4.1.1 *Dimensionless equation of mass conservation for forced convection*

After the substitution of the dimensionless variables, the equation (2.36) takes the form:

$$\frac{\rho_0 W_0}{L_0}\frac{\partial \rho^*}{\partial t^*} + \frac{\rho_0 W_0}{L_0}\frac{\partial}{\partial x^*}\left(\rho^* W_x^{\ *}\right) + \frac{\rho_0 D W_0}{D L_0}\frac{\partial}{\partial y^*}\left(\rho^* W_y^{\ *}\right) = 0 . \tag{2.66}$$

Multiplying the last equation with $\frac{L_0}{\rho_0 W_0}$, following equation could be obtained:

$$\frac{\partial \rho^*}{\partial t^*} + \frac{\partial}{\partial x^*}\left(\rho^* W_x^{\ *}\right) + \frac{\partial}{\partial y^*}\left(\rho^* W_y^{\ *}\right) = 0 . \tag{2.67}$$

Thus, the dimensionless equation of mass conservation can be written as:

$$\frac{\partial \rho^*}{\partial t^*} + \nabla^* \bullet \left(\rho^* \vec{W}^*\right) = 0 . \tag{2.68}$$

The significance of each term in the dimensionless equation of mass conservation for forced convection can be found in Table 1.

Table 1: Importance of each term in the equation of mass conservation

Term	Importance
$\frac{\partial \rho^*}{\partial t^*}$	Local temporal density change in a constant control volume

$\nabla^* \bullet \left(\rho^* \vec{W}^*\right)$	Specific mass flux through the surfaces of the control volume

2.4.1.2 Dimensionless equation of momentum conservation for forced convection

In order to derive the dimensionless equation of momentum conservation, the following dimensionless variables are introduced additionally:

$$\eta^* = \frac{\eta}{\eta_0} = 0(1)\,, \tag{2.69}$$

$$\vec{g}^* = \frac{\vec{g}}{g_0} = 0(1)\,. \tag{2.70}$$

Furthermore, since the static pressure does not appear in the equation of the momentum conservation, the dimensionless pressure $p*$ introduced as

$$p^* = \frac{p}{\rho_0 {W_0}^2} = 0(1) \tag{2.71}$$

describes the dynamic pressure only.

With the mentioned dimensionless variables, the momentum conservation equation (2.43) can be rewritten as:

$$\begin{aligned}
&\rho_0\rho^*\left[\frac{W_0^2}{L_0}\frac{\partial W_x^*}{\partial t^*}+\frac{{W_0}^2}{L_0}W_x^*\frac{\partial W_x^*}{\partial x^*}+\frac{{W_0}^2 D}{DL_0}W_y^*\frac{\partial W_x^*}{\partial y^*}\right]=-\frac{\rho_0 {W_0}^2}{L_0}\frac{\partial p^*}{\partial x^*}\\
&+2\frac{\eta_0 W_0}{{L_0}^2}\frac{\partial}{\partial x^*}\left(\eta^*\frac{\partial W_x^*}{\partial x^*}\right)+\frac{\eta_0 W_0}{D^2}\frac{\partial}{\partial y^*}\left(\eta^*\frac{\partial W_x^*}{\partial y^*}\right)+\frac{\eta_0 W_0 D}{L_0^2 D}\frac{\partial}{\partial y^*}\left(\eta^*\frac{\partial W_y^*}{\partial x^*}\right)\\
&+\frac{\eta_0' W_0}{{L_0}^2}\frac{\partial}{\partial x^*}\left(\eta'^*\frac{\partial W_x^*}{\partial x^*}\right)+\frac{\eta_0' W_0 D}{{L_0}^2 D}\frac{\partial}{\partial x^*}\left(\eta'^*\frac{\partial W_y^*}{\partial y^*}\right)+\rho_0 g_0\rho^*\vec{g}^*
\end{aligned} \tag{2.72}$$

for the x-direction and

$$\rho_0\rho^*\left[\frac{{W_0}^2 D}{L_0^2}\frac{\partial {W_y}^*}{\partial t^*}+\frac{{W_0}^2 D}{L_0^2}W_x^*\frac{\partial W_y^*}{\partial x^*}+\frac{{W_0}^2 D^2}{DL_0^2}W_y^*\frac{\partial W_y^*}{\partial y^*}\right]=-\frac{\rho_0 W_0^2}{D}\frac{\partial p^*}{\partial y^*}$$

$$+\frac{\eta_0 W_0}{DL_0}\frac{\partial}{\partial x^*}\left(\eta^*\frac{\partial W_x^*}{\partial y^*}\right)+\frac{\eta_0 W_0 D}{L_0^3}\frac{\partial}{\partial x^*}\left(\eta^*\frac{\partial W_y^*}{\partial x^*}\right)+2\frac{\eta_0 W_0 D}{D^2 L_0}\frac{\partial}{\partial y^*}\left(\eta^*\frac{\partial W_y^*}{\partial y^*}\right)$$

$$+\frac{\eta_0'\,W_0}{L_0 D}\frac{\partial}{\partial y^*}\left(\eta'^*\frac{\partial W_x^*}{\partial x^*}\right)+\frac{\eta_0'\,W_0 D}{L_0 D^2}\frac{\partial}{\partial y^*}\left(\eta'^*\frac{\partial W_y^*}{\partial y^*}\right)$$

for the y-direction.

It should also be mentioned that the gravitation term does not appear in the y-direction, because the gravity effect is assumed to act in the x-direction. The previous equations are now multiplied with $\frac{L_0}{\rho_0 W_0^2}$. Hence, the following equations could be obtained:

$$\rho^*\left[\frac{\partial {W_x}^*}{\partial t^*}+W_x^*\frac{\partial W_x^*}{\partial x^*}+W_y^*\frac{\partial W_x^*}{\partial y^*}\right]=-\frac{\partial p^*}{\partial x^*}$$

$$+2\frac{\eta_0}{\rho_0 W_0 L_0}\frac{\partial}{\partial x^*}\left(\eta^*\frac{\partial W_x^*}{\partial x^*}\right)+\frac{\eta_0 L_0}{D^2\rho_0 W_0}\frac{\partial}{\partial y^*}\left(\eta^*\frac{\partial W_x^*}{\partial y^*}\right)+\frac{\eta_0}{\rho_0 W_0 L_0}\frac{\partial}{\partial y^*}\left(\eta^*\frac{\partial W_y^*}{\partial x^*}\right)$$

$$-\frac{2}{3}\frac{\eta_0}{\rho_0 W_0 L_0}\frac{\partial}{\partial x^*}\left(\eta^*\frac{\partial W_x^*}{\partial x^*}\right)-\frac{2}{3}\frac{\eta_0}{\rho_0 W_0 L_0}\frac{\partial}{\partial x^*}\left(\eta^*\frac{\partial W_y^*}{\partial y^*}\right)+\frac{L_0 g_0}{W_0^2}\rho^*{g_x}^*$$

in the x-direction and

$$\rho^*\left[\frac{D}{L_0}\frac{\partial {W_y}^*}{\partial t^*}+\frac{D}{L_0}W_x^*\frac{\partial W_y^*}{\partial x^*}+\frac{D}{L_0}W_y^*\frac{\partial W_y^*}{\partial y^*}\right]=-\frac{L_0}{D}\frac{\partial p^*}{\partial y^*} \tag{2.73}$$

$$+\frac{\eta_0}{\rho_0 L_0 W_0}\frac{L_0}{D}\frac{\partial}{\partial x^*}\left(\eta^*\frac{\partial W_x^*}{\partial y^*}\right)+\frac{D}{L_0}\frac{\eta_0}{\rho_0 L_0 W_0}\frac{\partial}{\partial x^*}\left(\eta^*\frac{\partial W_y^*}{\partial x^*}\right)$$

$$+2\frac{\eta_0}{\rho_0 L_0 W_0}\frac{L_0}{D}\frac{\partial}{\partial y^*}\left(\eta^*\frac{\partial W_y^*}{\partial y^*}\right)$$

$$-\frac{2}{3}\frac{\eta_0}{\rho_0 L_0 W_0}\frac{L_0}{D}\frac{\partial}{\partial y^*}\left(\eta^*\frac{\partial W_x^*}{\partial x^*}\right)-\frac{2}{3}\frac{\eta_0}{\rho_0 L_0 W_0}\frac{L_0}{D}\frac{\partial}{\partial y^*}\left(\eta^*\frac{\partial W_y^*}{\partial y^*}\right)$$

in the y-direction.

In the previous equations, the following nondimensional numbers appear:

- Reynolds number

$$\mathrm{Re} = \frac{\rho_0 W_0 L_0}{\eta_0}, \tag{2.74}$$

which indicates the relative significance of the viscous effect compared to the inertia effect. However, the Reynolds number can also be calculated with the characteristic length during the compression, which is the diameter d of the inlet of the autoclave. Therefore, the dimensionless number Re_d can be introduced as:

$$\mathrm{Re}_d = \frac{\rho_0 W_0 d}{\eta_0} = \mathrm{Re} \cdot \frac{d}{L_0} = \mathrm{Re} \cdot d^*. \tag{2.75}$$

- Froude number

$$Fr = \frac{W_0^2}{L_0\, g} \tag{2.76}$$

describing the ratio of the inertial force to the gravitational force.

Thus, the dimensionless equation of mass conservation for forced convection can be described as follows:

$$\begin{aligned}
&\rho^* \left[\frac{\partial {W_x}^*}{\partial t^*} + W_x^* \frac{\partial W_x^*}{\partial x^*} + W_y^* \frac{\partial W_x^*}{\partial y^*} \right] = -\frac{\partial p^*}{\partial x^*} \\
&+ \frac{1}{\mathrm{Re}_d} \frac{d}{L_0} \left[2 \frac{\partial}{\partial x^*} \left(\eta^* \frac{\partial W_x^*}{\partial x^*} \right) + \left(\frac{L_0}{D} \right)^2 \frac{\partial}{\partial y^*} \left(\eta^* \frac{\partial W_x^*}{\partial y^*} \right) + \frac{\partial}{\partial y^*} \left(\eta^* \frac{\partial W_y^*}{\partial x^*} \right) \right. \\
&\left. - \frac{2}{3} \frac{\partial}{\partial x^*} \left(\eta^* \frac{\partial W_x^*}{\partial x^*} \right) - \frac{2}{3} \frac{\partial}{\partial x^*} \left(\eta^* \frac{\partial W_y^*}{\partial y^*} \right) \right] + \frac{1}{Fr} \rho^* {g_x}^*
\end{aligned}$$

in the x-direction and (2.77)

$$\begin{aligned}
&\rho^* \left[\frac{D}{L_0} \frac{\partial {W_y}^*}{\partial t^*} + \frac{D}{L_0} W_x^* \frac{\partial W_y^*}{\partial x^*} + \frac{D}{L_0} W_y^* \frac{\partial W_y^*}{\partial y^*} \right] = -\frac{L_0}{D} \frac{\partial p^*}{\partial y^*} \\
&+ \frac{1}{\mathrm{Re}_d} \frac{d}{L_0} \left[\frac{L_0}{D} \frac{\partial}{\partial x^*} \left(\eta^* \frac{\partial W_x^*}{\partial y^*} \right) + \frac{D}{L_0} \frac{\partial}{\partial x^*} \left(\eta^* \frac{\partial W_y^*}{\partial x^*} \right) + 2 \frac{L_0}{D} \frac{\partial}{\partial y^*} \left(\eta^* \frac{\partial W_y^*}{\partial y^*} \right) \right. \\
&\left. - \frac{2}{3} \frac{L_0}{D} \frac{\partial}{\partial y^*} \left(\eta^* \frac{\partial W_x^*}{\partial x^*} \right) - \frac{2}{3} \frac{L_0}{D} \frac{\partial}{\partial y^*} \left(\eta^* \frac{\partial W_y^*}{\partial y^*} \right) \right]
\end{aligned}$$

in the y-direction.

It should be noted that D and L_0 have the same magnitude, so that the terms $\frac{D}{L_0}\ and\ \frac{L_0}{D}$ alsways have the order of magnitude of 1. The importance of each term in the dimensionless equation of momentum conservation for forced convection can be found in Table 2.

Table 2: Importance of each term in the equation of momentum conservation

a) x-momentum	
Term	Importance
$\frac{\partial\left(\rho^* W_x{}^*\right)}{\partial t^*}$	Local acceleration
$W_x^*\frac{\partial\left(\rho^* W_x^*\right)}{\partial x^*}+W_y^*\frac{\partial\left(\rho^* W_x^*\right)}{\partial y^*}$	Convective momentum transport
$\frac{\partial p^*}{\partial x^*}$	Pressure gradient
$\frac{1}{\mathrm{Re}_d}\frac{d}{L_0}\left[2\frac{\partial}{\partial x^*}\left(\eta^*\frac{\partial W_x^*}{\partial x^*}\right)+\left(\frac{L_0}{D}\right)^2\frac{\partial}{\partial y^*}\left(\eta^*\frac{\partial W_x^*}{\partial y^*}\right)+\frac{\partial}{\partial y^*}\left(\eta^*\frac{\partial W_y^*}{\partial x^*}\right)-\frac{2}{3}\frac{\partial}{\partial x^*}\left(\eta^*\frac{\partial W_x^*}{\partial x^*}\right)-\frac{2}{3}\frac{\partial}{\partial x^*}\left(\eta^*\frac{\partial W_y^*}{\partial y^*}\right)\right]$	Frictional tensions
$\frac{1}{\mathrm{Fr}}\rho^* g_x{}^*$	Mass force

b) y-momentum	
$\frac{D}{L_0}\frac{\partial W_y^*}{\partial t^*}$	Local acceleration
$\frac{D}{L_0}W_x^*\frac{\partial W_y^*}{\partial x^*}+\frac{D}{L_0}W_y^*\frac{\partial W_y^*}{\partial y^*}$	Convective momentum transport
$\frac{L_0}{D}\frac{\partial p^*}{\partial y^*}$	Pressure gradient
$\frac{1}{\mathrm{Re}_d}\frac{d}{L_0}\left[\frac{L_0}{D}\frac{\partial}{\partial x^*}\left(\eta^*\frac{\partial W_x^*}{\partial y^*}\right)+\frac{D}{L_0}\frac{\partial}{\partial x^*}\left(\eta^*\frac{\partial W_y^*}{\partial x^*}\right)+2\frac{L_0}{D}\frac{\partial}{\partial y^*}\left(\eta^*\frac{\partial W_y^*}{\partial y^*}\right) -\frac{2}{3}\frac{L_0}{D}\frac{\partial}{\partial y^*}\left(\eta^*\frac{\partial W_x^*}{\partial x^*}\right)-\frac{2}{3}\frac{L_0}{D}\frac{\partial}{\partial y^*}\left(\eta^*\frac{\partial W_y^*}{\partial y^*}\right)\right]$	Frictional tensions

2.4.1.3 Dimensionless equation of energy conservation for forced convection

The dimensionless equation of energy conservation is obtained by implementing the mentioned dimensionless variables and several following non-dimensional additional variables:

$$T^* = \frac{T}{T_0}, \tag{2.78}$$

$$h^* = \frac{h}{c_{p0}T_0}, \tag{2.79}$$

$$\lambda^* = \frac{\lambda}{\lambda_0}. \tag{2.80}$$

However, in the energy equation the effect of the dynamic pressure is negligible in comparison to the hydrostatic pressure, which can be written in dimensionless form as follows:

$$p^* = \frac{p}{\rho_0 \, c_{p0} \, T_0} \, . \tag{2.81}$$

Hence, with the defined variables the equation for the total enthalpy can be rewritten as:

$$\begin{aligned}
&\rho_0 \rho^* \left[\frac{c_{p0} T_0 W_0}{L_0} \frac{\partial h^*}{\partial t^*} + \frac{{W_0}^3}{L_0} \frac{\partial}{\partial t^*} \left(\frac{{W_x^*}^2}{2} \right) + \frac{{W_0}^3 D^2}{L_0^3} \frac{\partial}{\partial t^*} \left(\frac{{W_y^*}^2}{2} \right) \right.\\
&+ \frac{c_{p0} T_0 \, W_0}{L_0} W_x^* \frac{\partial h^*}{\partial x^*} + \frac{c_{p0} T_0 \, W_0 D}{L_0 D} W_y^* \frac{\partial h^*}{\partial y^*}\\
&+ \frac{{W_0}^3}{L_0} W_x^* \frac{\partial}{\partial x^*} \left(\frac{{W_x^*}^2}{2} \right) + \frac{{W_0}^3 D^2}{L_0^3} W_x^* \frac{\partial}{\partial x^*} \left(\frac{{W_y^*}^2}{2} \right)\\
&\left. + \frac{{W_0}^3 D}{L_0 D} W_y^* \frac{\partial}{\partial y^*} \left(\frac{{W_x^*}^2}{2} \right) + \frac{{W_0}^3 D^3}{L_0^3 D} W_y^* \frac{\partial}{\partial y^*} \left(\frac{{W_y^*}^2}{2} \right) \right] =\\
&\frac{\rho_0 c_{p0} T_0 W_0}{L_0} \frac{\partial p^*}{\partial t^*} + \frac{\lambda_0 T_0}{{L_0}^2} \frac{\partial}{\partial x^*} \left(\lambda^* \frac{\partial T^*}{\partial x^*} \right) + \frac{\lambda_0 T_0}{D^2} \frac{\partial}{\partial y^*} \left(\lambda^* \frac{\partial T^*}{\partial y^*} \right)\\
&+ \frac{W_0}{L_0} W_x^* \frac{\partial}{\partial x^*} \eta_0 \eta^* \left[2 \frac{W_0}{L_0} \frac{\partial W_x^*}{\partial x^*} - \frac{2}{3} \left(\frac{W_0}{L_0} \frac{\partial W_x^*}{\partial x^*} + \frac{W_0 \, D}{L_0 D} \frac{\partial W_y^*}{\partial y^*} \right) \right]\\
&+ \frac{W_0 D}{L_0 D} W_y^* \frac{\partial}{\partial x^*} \eta_0 \eta^* \left[\frac{W_0}{D} \frac{\partial W_x^*}{\partial y^*} + \frac{W_0 D}{L_0^2} \frac{\partial W_y^*}{\partial x^*} \right]\\
&+ \frac{W_0}{D} W_x^* \frac{\partial}{\partial y^*} \eta_0 \eta^* \left[\frac{W_0}{D} \frac{\partial W_x^*}{\partial y^*} + \frac{W_0 D}{L_0^2} \frac{\partial W_y^*}{\partial x^*} \right]\\
&+ \frac{W_0 D}{L_0 D} W_y^* \frac{\partial}{\partial y^*} \eta_0 \eta^* \left[2 \frac{W_0 D}{L_0 D} \frac{\partial W_y^*}{\partial y^*} - \frac{2}{3} \left(\frac{W_0}{L_0} \frac{\partial W_x^*}{\partial x^*} + \frac{W_0 \, D}{L_0 D} \frac{\partial W_y^*}{\partial y^*} \right) \right]\\
&+ \rho_0 \, g_0 W_0 \, \rho^* {g_x}^* \bullet W_x^* .
\end{aligned} \tag{2.82}$$

.

Multiplying the previous equation with $\frac{L_0}{\rho_0 W_0^3}$ the former equation can be described in its dimensionless form as:

$$
\begin{aligned}
&\rho^{*}\left[\frac{1}{Ec}\frac{\partial h^{*}}{\partial t^{*}}+\frac{\partial}{\partial t^{*}}\left(\frac{{W_x}^{*2}}{2}\right)+\frac{D^2}{L_0^2}\frac{\partial}{\partial t^{*}}\left(\frac{{W_y}^{*2}}{2}\right)\right.\\
&+\frac{1}{Ec}W_x^{*}\frac{\partial h^{*}}{\partial x^{*}}+\frac{1}{Ec}W_y^{*}\frac{\partial h^{*}}{\partial y^{*}}\\
&+W_x^{*}\frac{\partial}{\partial x^{*}}\left(\frac{W_x^{*2}}{2}\right)+\frac{D^2}{L_0^2}W_x^{*}\frac{\partial}{\partial x^{*}}\left(\frac{W_y^{*2}}{2}\right)\\
&\left.+W_y^{*}\frac{\partial}{\partial y^{*}}\left(\frac{W_x^{*2}}{2}\right)+\frac{D^2}{L_0^2}W_y^{*}\frac{\partial}{\partial y^{*}}\left(\frac{W_y^{*2}}{2}\right)\right] \quad =\\
&\frac{1}{Ec}\frac{\partial p^{*}}{\partial t^{*}}+\frac{1}{\Pr \mathrm{Re}_d\, Ec}\frac{d}{L_0}\left[\frac{\partial}{\partial x^{*}}\left(\lambda^{*}\frac{\partial T^{*}}{\partial x^{*}}\right)+\left(\frac{L_0}{D}\right)^2\frac{\partial}{\partial y^{*}}\left(\lambda^{*}\frac{\partial T^{*}}{\partial y^{*}}\right)\right]\\
&+\frac{1}{\mathrm{Re}_d}\frac{d}{L_0}\left\{W_x^{*}\frac{\partial}{\partial x^{*}}\eta^{*}\left[2\frac{\partial W_x^{*}}{\partial x^{*}}-\frac{2}{3}\left(\frac{\partial W_x^{*}}{\partial x^{*}}+\frac{\partial W_y^{*}}{\partial y^{*}}\right)\right]\right.\\
&+W_y^{*}\frac{\partial}{\partial x^{*}}\eta^{*}\left[\frac{L_0}{D}\frac{\partial W_x^{*}}{\partial y^{*}}+\frac{D}{L_0}\frac{\partial W_y^{*}}{\partial x^{*}}\right]+W_x^{*}\frac{\partial}{\partial y^{*}}\eta^{*}\left[\left(\frac{L_0}{D}\right)^2\frac{\partial W_x^{*}}{\partial y^{*}}+\frac{\partial W_y^{*}}{\partial x^{*}}\right]\\
&\left.+W_y^{*}\frac{\partial}{\partial y^{*}}\eta^{*}\left[2\frac{\partial W_y^{*}}{\partial y^{*}}-\frac{2}{3}\left(\frac{\partial W_x^{*}}{\partial x^{*}}+\frac{\partial W_y^{*}}{\partial y^{*}}\right)\right]\right\}\\
&+\frac{1}{Fr}\rho^{*}{g_x}^{*}\bullet W_x^{*}.
\end{aligned}
\tag{2.83}
$$

In the dimensionless equation of total enthalpy, the following additional dimensionless numbers appear:

- Eckert number

$$Ec=\frac{W_0^2}{c_{p0}\,T_0}, \tag{2.84}$$

which describes the relation between the kinetic energy and the enthalpy. It represents a measure for the compressibility of the fluid.

- Prandtl number

$$\Pr=\frac{\eta_0 c_{p0}}{\lambda_0}, \tag{2.85}$$

which characterizes the ratio of the thermal and viscous diffusion.

To identify the importance of each term in the equation (2.83), it is multiplied with Ec. Thus, following equation can be obtained:

$$
\begin{aligned}
&\rho^*\Bigg[\frac{\partial h^*}{\partial t^*}+Ec\frac{\partial}{\partial t^*}\left(\frac{{W_x}^{*2}}{2}\right)+Ec\frac{D^2}{L_0^2}\frac{\partial}{\partial t^*}\left(\frac{{W_y}^{*2}}{2}\right)\\
&+W_x^*\frac{\partial h^*}{\partial x^*}+W_y^*\frac{\partial h^*}{\partial y^*}\\
&+EcW_x^*\frac{\partial}{\partial x^*}\left(\frac{W_x^{*2}}{2}\right)+Ec\frac{D^2}{L_0^2}W_x^*\frac{\partial}{\partial x^*}\left(\frac{W_y^{*2}}{2}\right)\\
&+EcW_y^*\frac{\partial}{\partial y^*}\left(\frac{W_x^{*2}}{2}\right)+Ec\frac{D^2}{L_0^2}W_y^*\frac{\partial}{\partial y^*}\left(\frac{W_y^{*2}}{2}\right)\Bigg] \quad =\\
&\frac{\partial p^*}{\partial t^*}+\frac{1}{\Pr\mathrm{Re}_d}\frac{d}{L_0}\left[\frac{\partial}{\partial x^*}\left(\lambda^*\frac{\partial T^*}{\partial x^*}\right)+\left(\frac{L_0}{D}\right)^2\frac{\partial}{\partial y^*}\left(\lambda^*\frac{\partial T^*}{\partial y^*}\right)\right]\\
&+\frac{Ec}{\mathrm{Re}_d}\frac{d}{L_0}\Bigg\{W_x^*\frac{\partial}{\partial x^*}\eta^*\left[2\frac{\partial W_x^*}{\partial x^*}-\frac{2}{3}\left(\frac{\partial W_x^*}{\partial x^*}+\frac{\partial W_y^*}{\partial y^*}\right)\right]\\
&+W_y^*\frac{\partial}{\partial x^*}\eta^*\left[\frac{L_0}{D}\frac{\partial W_x^*}{\partial y^*}+\frac{D}{L_0}\frac{\partial W_y^*}{\partial x^*}\right]+W_x^*\frac{\partial}{\partial y^*}\eta^*\left[\left(\frac{L_0}{D}\right)^2\frac{\partial W_x^*}{\partial y^*}+\frac{\partial W_y^*}{\partial x^*}\right]\\
&+W_y^*\frac{\partial}{\partial y^*}\eta^*\left[2\frac{\partial W_y^*}{\partial y^*}-\frac{2}{3}\left(\frac{\partial W_x^*}{\partial x^*}+\frac{\partial W_y^*}{\partial y^*}\right)\right]\Bigg\}\\
&+\frac{Ec}{Fr}\rho^*{g_x}^*\bullet W_x^*.
\end{aligned}
\tag{2.86}
$$

Furthermore, another dimensionless number can be found. The ratio of the thermal energy convected to the fluid to the thermal energy conducted within the fluid is defined as the Peclet number, which is the product of the Reynolds number and the Prandtl number:

$Pe=\mathrm{Re}\Pr$.

The importance of each term in the dimensionless equation of energy conservation for forced convection can be found in Table 3.

Table 3: Importance of each term in the equation for total enthalpy

Term	Importance
$\frac{\partial h^*}{\partial t^*}$	Local enthalpy change
$Ec\frac{\partial}{\partial t^*}\left(\frac{{W_x^*}^2}{2}\right)+Ec\frac{D^2}{L_0^2}\frac{\partial}{\partial t^*}\left(\frac{{W_y^*}^2}{2}\right)$	Local change of the kinetic energy
$W_x^*\frac{\partial h^*}{\partial x^*}+W_y^*\frac{\partial h^*}{\partial y^*}$	Convective energy transport in a control volume
$EcW_x^*\frac{\partial}{\partial x^*}\left(\frac{{W_x^*}^2}{2}\right)+Ec\frac{D^2}{L_0^2}W_x^*\frac{\partial}{\partial x^*}\left(\frac{{W_y^*}^2}{2}\right)$ $+EcW_y^*\frac{\partial}{\partial y^*}\left(\frac{{W_x^*}^2}{2}\right)+Ec\frac{D^2}{L_0^2}W_y^*\frac{\partial}{\partial y^*}\left(\frac{{W_y^*}^2}{2}\right)$	Convective transport of kinetic energy in a control volume
$\frac{\partial p^*}{\partial t^*}$	Local pressure change
$\frac{1}{\Pr \mathrm{Re}_d}\frac{d}{L_0}\left[\frac{\partial}{\partial x^*}\left(\lambda^*\frac{\partial T^*}{\partial x^*}\right)+\left(\frac{L_0}{D}\right)^2\frac{\partial}{\partial y^*}\left(\lambda^*\frac{\partial T^*}{\partial y^*}\right)\right]$	Diffusive transport of thermal energy (thermal conduction)

$\frac{Ec}{\mathrm{Re}_d}\frac{d}{L_0}\left\{W_x^*\frac{\partial}{\partial x^*}\eta^*\left[2\frac{\partial W_x^*}{\partial x^*}-\frac{2}{3}\left(\frac{\partial W_x^*}{\partial x^*}+\frac{\partial W_y^*}{\partial y^*}\right)\right]\right.$ $+W_y^*\frac{\partial}{\partial x^*}\eta^*\left[\frac{L_0}{D}\frac{\partial W_x^*}{\partial y^*}+\frac{D}{L_0}\frac{\partial W_y^*}{\partial x^*}\right]+W_x^*\frac{\partial}{\partial y^*}\eta^*\left[\left(\frac{L_0}{D}\right)^2\frac{\partial W_x^*}{\partial y^*}+\frac{\partial W_y^*}{\partial x^*}\right]$ $\left.+W_y^*\frac{\partial}{\partial y^*}\eta^*\left[2\frac{\partial W_y^*}{\partial y^*}-\frac{2}{3}\left(\frac{\partial W_x^*}{\partial x^*}+\frac{\partial W_y^*}{\partial y^*}\right)\right]\right\}$	Irreversible conversion of kinetic energy into thermal energy
$\frac{\mathrm{Ec}}{\mathrm{Fr}}\rho^* g_x{}^* \bullet W_x^*$	Work done by body forces

2.4.1.4 Dimensionless equation of mass conservation for free convection

During the pressure holding phase, free convection dominates due to the cooling process taking place at the wall of the autoclave. The comparatively colder steel wall removes heat from the fluid. Due to the density difference, the colder fluid flows downwards and the warmer fluid upwards.

In this case, the characteristic length for the flow during free convection is the length of the autoclave L_0. As found in the literature [78], the characteristic velocity during free convection, which is used to approximate the velocity and the significance of each term in the upcoming chapter 4.1 can be defined as:

$$W_{buoy}=\sqrt{g\,\alpha_0\Delta T L_0}\,. \tag{2.87}$$

Moreover, the characteristic length in the y-direction is not the diameter of the inlet but the diameter of the inner volume of the autoclave. Thus y^* can be defined as:

$$y^*=\frac{y}{D}=0(1)\,. \tag{2.88}$$

The dimensionless equation of mass conservation for free convection is the same one as for forced convection, which was shown in equation (2.68), and should not be shown again here.

2.4.1.5 Dimensionless equation of momentum conservation for free convection

One force that is prominent during the pressure holding phase is the buoyancy force $\nabla\rho \bullet \vec{g}$. The buoyant force is essentially caused by the density difference. Because the density of a compressible fluid is a function of pressure and temperature, the Boussinesq approximation should help to identify the pressure difference as a function of temperature and pressure:

$$(\rho - \rho_0) = \rho_0(\beta\Delta p - \alpha\Delta T) = \rho_0(\beta(p - p_0) - \alpha(T - T_0)). \tag{2.89}$$

The dimensionless thermal expansion coefficient must be defined as:

$$\alpha^* = \frac{\alpha}{\alpha_0}, \tag{2.90}$$

and the dimensionless compressibility coefficient as:

$$\beta^* = \frac{\beta}{\beta_0}. \tag{2.91}$$

Thus, the dimensionless equation of momentum conservation in x-direction can be described as:

$$\begin{aligned}
&\rho^* \left[\frac{\partial W_x^*}{\partial t^*} + W_x^* \frac{\partial W_x^*}{\partial x^*} + W_y^* \frac{\partial W_x^*}{\partial y^*}\right] = -\frac{\partial p^*}{\partial x^*} \\
&+ \frac{1}{\mathrm{Re}}\left[2\frac{\partial}{\partial x^*}\left(\eta^* \frac{\partial W_x^*}{\partial x^*}\right) + \frac{L_0^2}{D^2}\frac{\partial}{\partial y^*}\left(\eta^* \frac{\partial W_x^*}{\partial y^*}\right) + \frac{\partial}{\partial y^*}\left(\eta^* \frac{\partial W_y^*}{\partial x^*}\right)\right. \\
&\left. - \frac{2}{3}\frac{\partial}{\partial x^*}\left(\eta^* \frac{\partial W_x^*}{\partial x^*}\right) - \frac{2}{3}\frac{\partial}{\partial x^*}\left(\eta^* \frac{\partial W_y^*}{\partial y^*}\right)\right] \\
&+ \frac{g_x^*}{\mathrm{Re}^2} Ga(\alpha_0\Delta T + \beta_0\Delta p), with
\end{aligned} \tag{2.92}$$

the Galileo number, which is normally defined in the following form:

$$Ga = \frac{\rho_0 g_0 L_0^3}{\eta_0} = \frac{\mathrm{Re}^2}{Fr}. \tag{2.93}$$

During the pressure holding phase, especially in the adiabatic case $\Delta p = 0$, so that the term $\beta_0 \Delta p$ is negligible. Thus, another dimensionless number called Grashof number can be introduced:

$$Gr = Ga\alpha_0 \Delta T = \frac{\rho_0^2 \alpha_0 g_0 \Delta T L_0^3}{\eta^2}. \tag{2.94}$$

In particular, the last term of the equation (2.92) is of great importance for the buoyancy. The product of the Grashof and Reynolds number seen in this last term can also be defined as the Archimedes number:

$$Ar = \frac{Gr}{\mathrm{Re}^2}, \tag{2.95}$$

which determines the motion of the fluid due to density differences.

The significance of each term in the dimensionless equation of momentum conservation for free convection can also be found in Table 2. The significance of an additional term appearing in the equation for free convection can be found in Table 4.

Table 4: Importance of an additional term in the equation of momentum conservation for free convection

Term	Importance
$\frac{g_x^*}{\mathrm{Re}^2} Ga(\alpha_0 \Delta T + \beta_0 \Delta p)$	Buoyancy force due to the change of temperature and pressure

2.4.1.6 Dimensionless equation of energy conservation for free convection

The dimensionless equation of energy conservation for free convection has the following form:

$$
\begin{aligned}
&\rho^*\Bigg[\frac{\partial h^*}{\partial t^*}+Ec\frac{\partial}{\partial t^*}\left(\frac{{W_x}^{*2}}{2}\right)+Ec\frac{D^2}{L_0^2}\frac{\partial}{\partial t^*}\left(\frac{{W_y}^{*2}}{2}\right) \\
&+W_x^*\frac{\partial h^*}{\partial x^*}+W_y^*\frac{\partial h^*}{\partial y^*} \\
&+EcW_x^*\frac{\partial}{\partial x^*}\left(\frac{W_x^{*2}}{2}\right)+Ec\frac{D^2}{L_0^2}W_x^*\frac{\partial}{\partial x^*}\left(\frac{W_y^{*2}}{2}\right) \\
&+EcW_y^*\frac{\partial}{\partial y^*}\left(\frac{W_x^{*2}}{2}\right)+Ec\frac{D^2}{L_0^2}W_y^*\frac{\partial}{\partial y^*}\left(\frac{W_y^{*2}}{2}\right)\Bigg]= \\
&\frac{\partial p^*}{\partial t^*}+\frac{1}{Gr\,\Pr}\left[\frac{\partial}{\partial x^*}\left(\lambda^*\frac{\partial T^*}{\partial x^*}\right)+\frac{L_0^2}{D^2}\frac{\partial}{\partial y^*}\left(\lambda^*\frac{\partial T^*}{\partial y^*}\right)\right] \\
&+\frac{Ec}{\mathrm{Re}}\Bigg\{W_x^*\frac{\partial}{\partial x^*}\eta^*\left[2\frac{\partial W_x^*}{\partial x^*}-\frac{2}{3}\left(\frac{\partial W_x^*}{\partial x^*}+\frac{\partial W_y^*}{\partial y^*}\right)\right] \\
&+W_y^*\frac{\partial}{\partial x^*}\eta^*\left[\frac{L_0}{D}\frac{\partial W_x^*}{\partial y^*}+\frac{D}{L_0}\frac{\partial W_y^*}{\partial x^*}\right]W_x^*\frac{\partial}{\partial y^*}\eta^*\left[\frac{L_0^2}{D^2}\frac{\partial W_x^*}{\partial y^*}+\frac{\partial W_y^*}{\partial x^*}\right] \\
&+W_y^*\frac{\partial}{\partial y^*}\eta^*\left[2\frac{\partial W_y^*}{\partial y^*}-\frac{2}{3}\left(\frac{\partial W_x^*}{\partial x^*}+\frac{\partial W_y^*}{\partial y^*}\right)\right]\Bigg] \\
&+\frac{Ec}{Fr}\rho^*{g_x}^*\bullet W_x^*\,.
\end{aligned}
\tag{2.96}
$$

Herein, the characteristic dimensionless number called Rayleigh number is introduced as:

$$Ra=\Pr Gr\,. \tag{2.97}$$

The Rayleigh number is associated with the heat transfer within the fluid. In cases where the temperature gradient is not totally parallel to the gravity vector, the critical Rayleigh number of 0 is considered and free convection always occurs. However, if the temperature and density gradient of the fluid is totally parallel to the gravity vector $\vec{g}$ and the Rayleigh number is below a critical value of $657-2710$ depending on the boundary conditions for a fluid, heat transfer is primary in the form of conduction. Only if the critical Rayleigh number is exceeded in such cases, heat transfer is primary in the form of convection.

The importance of each term in the dimensionless equation of energy conservation for forced convection can also be found in Table 3. The importance of an additional term is shown in the following Table 5.

Table 5: Importance of an additional term in the equation of energy conservation for free convection

Term	Importance
$\frac{1}{Ra}\left[\frac{\partial}{\partial x^*}\left(\lambda^*\frac{\partial T^*}{\partial x^*}\right)+\frac{L_0^2}{D^2}\frac{\partial}{\partial y^*}\left(\lambda^*\frac{\partial T^*}{\partial y^*}\right)\right]$	Thermal conduction

2.4.2 Dimensionless equation for the temperature change

The energy equation (2.52) can be written in its dimensionless form as:

$$\begin{aligned}
&c_p^*\rho^*\left[\frac{\partial T^*}{\partial t^*}+W_x^*\frac{\partial T^*}{\partial x^*}+W_y^*\frac{\partial T^*}{\partial y^*}\right]=\\
&\Pi_T\left\{\alpha^*T^*\frac{\partial p^*}{\partial t^*}+\alpha^*T^*\left[W_x^*\frac{\partial p^*}{\partial x^*}+W_y^*\frac{\partial p^*}{\partial y^*}\right]\right\}\\
&+\frac{1}{\mathrm{Re}\,\mathrm{Pr}}\left[\frac{\partial}{\partial x^*}\left(\lambda^*\frac{\partial T^*}{\partial x^*}\right)+\frac{L_0^2}{D^2}\frac{\partial}{\partial y^*}\left(\lambda^*\frac{\partial T^*}{\partial y^*}\right)\right]\\
&+\frac{Ec}{\mathrm{Re}}\left\{2\eta^*\left[\left(\frac{\partial W_x^*}{\partial x^*}\right)^2+\left(\frac{\partial W_y^*}{\partial y^*}\right)^2+\frac{1}{2}\left(\frac{L_0^2}{D^2}\frac{\partial W_x^*}{\partial y^*}+\frac{\partial W_y^*}{\partial x^*}\right)^2\right]\right.\\
&\left.-\frac{2}{3}\eta^*\left[\frac{\partial W_x^*}{\partial x^*}+\frac{\partial W_y^*}{\partial y^*}\right]\right\}
\end{aligned} \quad . \tag{2.98}$$

Next, the dimensionless temperature increase as the relation between the actual temperature increase and adiabatic temperature increase, which is the maximum possible temperature increase in the adiabatic case, is defined as follow:

$$(\Delta T)^*=\frac{T-T_0}{T_{AdMax}-T_0}=\frac{T^*-1}{T_{AdMax}^*-1}=\frac{T^*-1}{\Delta T_{Ad\max}^*}=0(1)\,. \tag{2.99}$$

Thus, after differentiating this equation, dT^* can also be substituted according to this relation:

$$d(\Delta T)^*=\frac{1}{\Delta T_{Ad\max}^*}dT^*\,. \tag{2.100}$$

Thus, the dimensionless equation for the dimensionless temperature distribution can be described as:

$$\begin{aligned}
&c_p^* \rho^* \Delta T^*_{Ad\,\max} \left[\frac{\partial (\Delta T)^*}{\partial t^*} + W_x^* \frac{\partial (\Delta T)^*}{\partial x^*} + W_y^* \frac{\partial (\Delta T)^*}{\partial y^*} \right] = \\
&\Pi_T \left[\Delta T^*_{Ad\,\max} \cdot (\Delta T)^* + 1 \right] \left\{ \alpha^* \frac{\partial p^*}{\partial t^*} + \alpha^* \left[W_x^* \frac{\partial p^*}{\partial x^*} + W_y^* \frac{\partial p^*}{\partial y^*} \right] \right\} \\
&+ \frac{\Delta T^*_{Ad\,\max}}{\mathrm{Re}\,\mathrm{Pr}} \left[\frac{\partial}{\partial x^*} \left(\lambda^* \frac{\partial (\Delta T)^*}{\partial x^*} \right) + \frac{L_0^2}{D^2} \frac{\partial}{\partial y^*} \left(\lambda^* \frac{\partial (\Delta T)^*}{\partial y^*} \right) \right] \quad . \\
&+ \frac{Ec}{\mathrm{Re}} \left\{ 2\eta^* \left[\left(\frac{\partial W_x^*}{\partial x^*} \right)^2 + \left(\frac{\partial W_y^*}{\partial y^*} \right)^2 + \frac{1}{2} \left(\frac{L_0^2}{D^2} \frac{\partial W_x^*}{\partial y^*} + \frac{\partial W_y^*}{\partial x^*} \right)^2 \right] \right. \\
&\left. - \frac{2}{3} \eta^* \left[\frac{\partial W_x^*}{\partial x^*} + \frac{\partial W_y^*}{\partial y^*} \right] \right\}
\end{aligned} \tag{2.101}$$

Furthermore, the importance of each term of this equation is explained in the following Table 6.

Table 6 : The importance of each term of the dimensionless equation for the temperature change

Term	Importance
$c_p^* \rho^* \left[\frac{\partial T^*}{\partial t^*} \right]$	Local temperature change
$c_p^* \rho^* \left[W_x^* \frac{\partial T^*}{\partial x^*} + W_y^* \frac{\partial T^*}{\partial y^*} \right]$	Convective temperature change
$\Pi_T \ \alpha^* T^* \left\{ \frac{\partial p^*}{\partial t^*} + \left[W_x^* \frac{\partial p^*}{\partial x^*} + W_y^* \frac{\partial p^*}{\partial y^*} \right] \right\}$	Temperature change due to density change

$\frac{Ec}{Re}\left\{2\eta^*\left[\left(\frac{\partial W_x^*}{\partial x^*}\right)^2+\left(\frac{\partial W_y^*}{\partial y^*}\right)^2+\frac{1}{2}\left(\frac{L_0^2}{D^2}\frac{\partial W_x^*}{\partial y^*}+\frac{\partial W_y^*}{\partial x^*}\right)^2\right] -\frac{2}{3}\eta^*\left[\frac{\partial W_x^*}{\partial x^*}+\frac{\partial W_y^*}{\partial y^*}\right]\right\}$	Irreversible conversion of kinetic energy into thermal energy

2.5 Characteristics of Buoyant Turbulent Free Shear Flows

As mentioned before, there are two different methods to generate the desired pressure level for the high pressure treatment. The first way is to reduce the inner volume of the high pressure chamber mechanically with a piston until the desired pressure level is reached. This method was partly studied by Kowalczyk [54] and is being investigated in detail by Rauh [87] with numerical approaches. The second way is to force a defined amount of the pressure fluid to penetrate the inner chamber of the autoclave with a pump. The volume change work done during the compression of the pressure fluid results in an increase of both pressure and temperature inside the autoclave. This pressure build-up method and its characteristics are subjects of interest in this thesis and shall be discussed in detail.

At the beginning of the pressure treatment, there is no movement of the fluid inside of the autoclave, and the start temperature of both the pressure fluid and the material of the autoclave is constant. As soon as the pressure fluid enters the inner chamber of the autoclave, a round and axisymmetric “free jet” or “free shear flow”, which can be defined as a fluid jet without solid boundaries such as fluid discharging into the open, occurs. In this case, it is the pressure fluid that is pumped through the small inlet into the comparatively larger inner volume of the autoclave.

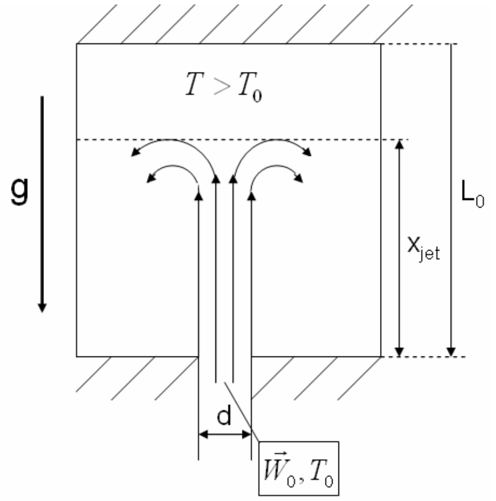

Figure 9 : During the compression of the pressure fluid, the pressure fluid is pumped through an inlet into the inner volume of the autoclave, causing free shear jet.

The mixing behavior of a free jet with its environment is of great interest. It can be observed that the dynamic pressure profile spreads to the side of the free jet, and that the original inlet velocity is maintained only in the middle of the free jet. The radius of the free jet then increases linearly with its length, where the region with the original inlet velocity becomes smaller. The length of this "near field" is about four to five times the height of the nozzle outlet. The free jet also spreads out to the side with the shape of a conus, as more fluid from the environment is carried along by the jet (Figure 10). After this the velocity on the axis decreases in a transition field until the distribution of the velocity becomes that of the "far field" ~ $(x - x_0)^{-1/2}$.

Figure 10 : Turbulent free jet: near, transition and far field [88].

Hence, most of the flow can be either described as laminar or turbulent. Turbulent flow occurs when the boundary layer of the flow becomes unstable. There is a critical Reynolds number, above which the inertia forces dominate over the viscous forces and flow instabilities grow, resulting in turbulence. In pipe flow, for instance, the critical Reynolds number, where the flow becomes turbulent, is generally accepted at 2300. However, the critical Reynolds number of each flow application is different, so that it has to be determined for each flow type separately. In the literatures, there are studies, where experiments and numerical simulations were carried out to determine the correct critical Reynolds number in an incompressible jet flow, for instance the contribution of Sato [89] and Morgan and Armfield [90]. It is assumed that the first instabilites of the free jet flow occur at a Reynolds number as small as 33 [111]. During the high pressure treatment, it is of interest to build up the pressure quickly to reduce the processing time that the fluid requires to enter the high pressure chamber at higher Reynolds numbers. The approximation of the Reynolds number in the high pressure treatment will be carried out at a later point. In order to explain the laminar-turbulent transition, the topology of the flow must be considered. Figure 11 (left) illustrates an example of a laminar free jet of a sugar solution, where the mixing of the jet with the surrounding fluid is almost not recognizable, and the jet remains stable. However, as soon as the first vortices appear (Figure 11 right), the stability of the jet is destroyed. Furthermore, the periodic “Von Kármán” Vortices can be observed, and the total length of the jet stream is not as long as that of the laminar free jet.

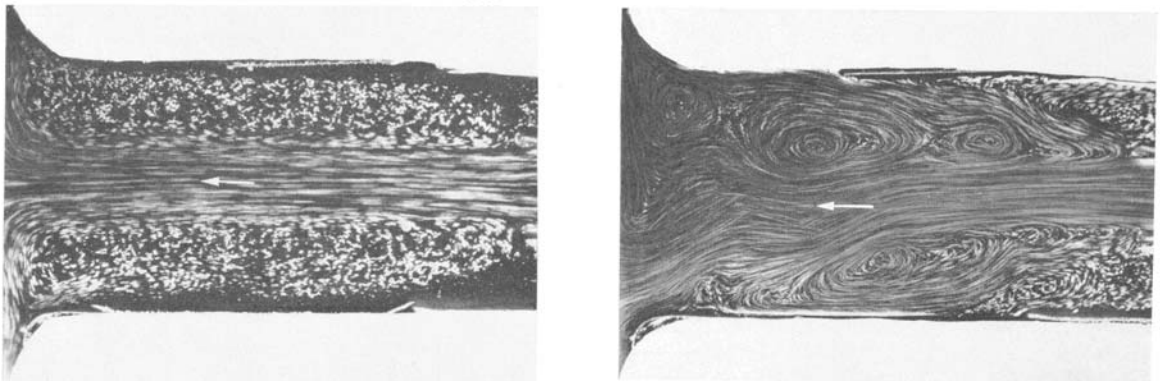

Figure 11 : Pictures of a laminar free jet on the left side. As soon as the first vortices appear, the jet becomes unstable as can be seen on the right side, and periodic vortices, so called v on Kármán Vortices, can be observed [91].

Hence, it is characteristic for a round free jet to have periodic ring-shape vortices at Reynolds numbers between 2000 and 40000. However, this vortex structure is destroyed as soon as turbulence occurs, and the classic structure of the free jet as shown in Figure 10 can then be observed. Furthermore, it is known that the relation between the density of the jet and that of the surrounding fluid has strong influences on the shape and the length scale of the jet and its core length (see Figure 12).

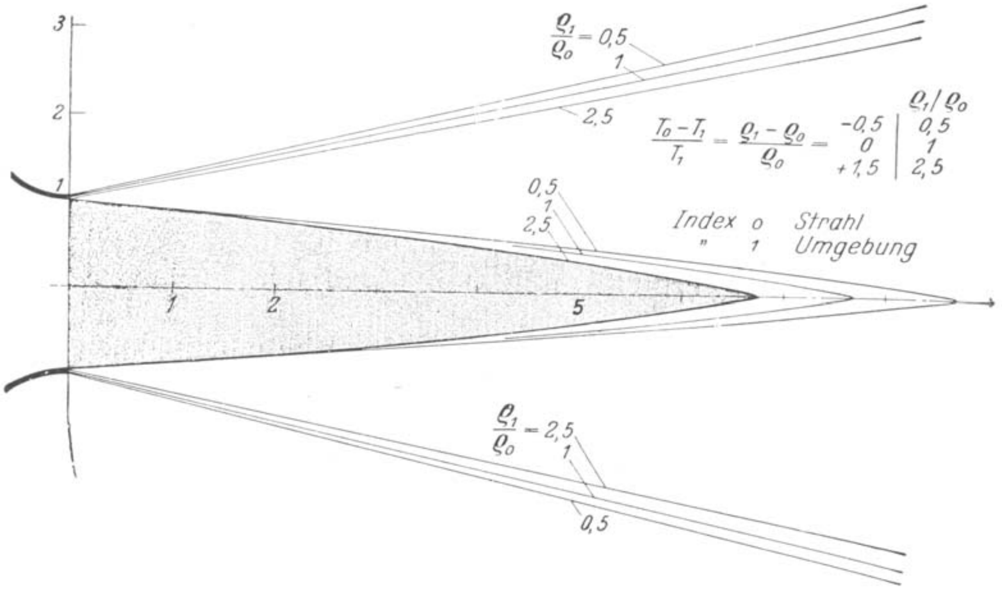

Figure 12 : Density difference between the jet and its surrounding fluid has significant influences on the shape and the length of the free jet [91].

As the high pressure autoclave used in this thesis is a vertical one with an inlet at its bottom, the pressure fluid will be pumped vertically against the gravitation (compare Figure 9). As the fluid is pumped in and the volume change work is transformed to increasing pressure levels and also to higher temperatures, temperature gradients occur. Although pressure spreads out with the speed of sound, the thermal compensation process does not occur instantaneously, so that thermal equilibrium is not present. This was explained by Delgado and Hartmann thoroughly [33]. And due to this temperature and density difference between the colder jet and warmer surrounding fluid, buoyancy takes place. Therefore, the penetration length of the jet does not only depend on the Reynolds number of the flow and its momentum, but also on the buoyancy forces acting upon the jet. The relation between the buoyancy and the momentum force is described with the dimensionless group called Archimedes number

$$Ar = \frac{L_0 \cdot g \cdot \Delta T}{W_0^{\ 2} T}, \text{ with } L_0 \text{ as the characteristic length and } W_0 \text{ as the velocity.} \tag{2.102}$$

With numerical simulations taking into account both forces, the total length of the jet (x_{jet}) can then be determined at the point, where the velocity component in the direction of the flow tends to zero (compare Figure 9). This jet length is expected to be transient, as the momentum of the jet is given and constant due to the constant pressure build-up rate, but the buoyancy forces are transient, as the temperature gradient inside the autoclave is also transient.

2.6 Computation with Turbulence Models

In general, there are three basic numerical simulation concepts available to compute the three-dimensional and time-dependent topology of a turbulent flow based on the solution of the Navier-Stokes equations. The first concept is the Direct Numerical Simulation (DNS), which resolves all the relevant scales in a turbulent flow, but its application is limited to only small Reynolds numbers. For instance, Moin and Mahesh [92] illustrated the complementary nature of experiment and direct numerical simulation in turbulence research. Significant knowledge of the turbulence physics has been gained from DNS of certain idealized flows, which cannot be easily obtained in experiments. Furthermore, the contribution of Friedrich et al. [93] gives a good overview and discussed recent achievements of direct numerical simulation (DNS) of incompressible flows.

The second concept called Large-Eddy simulation (LES) delivers directly the spatial and transient behaviour of large-scale structures also at higher Reynolds number, and the effects of small-scale motions which cannot be resolved on a given numerical grid need to be modelled with a so-called subgrid-scale (SGS) model. The LES concept was applied by Murakami et al. [94], who calculated the flow over a periodic arrangement of cubes in a simulated atmospheric boundary layer.

As a third way, turbulence models are used to predict the effects of turbulence in fluid flow by time averaging the flow variables. A number of turbulence models was developed that can be used to approximate turbulence based on the Reynolds averaged Navier-Stokes (RANS) equations.

The uncertainty of mathematically modelling turbulence is reflected in the large variety of models available. These range from Prandtl's zero-equation mixing length model [95] to more complex higher order models. Nowadays, two-equation turbulence models are widely used, since they offer a good compromise between numerical effort and numerical accuracy. Two equation models solve both the turbulent kinetic energy and the turbulent length scale using separate transport equations, hence the term "two-equation".

In two-equation models the velocity scale of the turbulence is calculated from the turbulent kinetic energy, which is provided from the solution of its transport equation. The length scale is estimated from two properties of the turbulence field, usually the turbulent kinetic energy and its dissipation rate. The dissipation rate of the turbulent kinetic energy is provided from the solution of its transport equation.

At present the majority of CFD calculations are carried out using Launder and Spalding's k-ε model [96], which is optimized for flows with high Reynolds number. In this model, k is the turbulence kinetic energy and is defined as the variance of the fluctuations in velocity. Furthermore, ε is the turbulence eddy dissipation, which is the rate at which the velocity fluctuations dissipate. Another interesting model called k-ω model was developed by Wilcox [97, 98] introducing the turbulent frequency ω and gives accurate results at near wall regions.

Menter's Shear Stress Transport model [99] combines the advantages of both the k-ε and the k-ω models and results in better predictions for heat transfer and the transition between laminar and turbulent flow. This could be confirmed by the work done by Vieser et al. [100], who carried out numerical investigations of different flow types with various turbulence models. However, the SST model will cause a slight additional computational cost over other two equation models as more equations are solved. But memory requirement increase should be small. The accuracy of the SST model in both the near wall regions and at some distance away from the wall could be confirmed. Thus, the SST model is considered suitable for the numerical simulations in this thesis and should be explained briefly.

2.6.1 Shear Stress Transport (SST) Model

The SST model accounts for the transport of the turbulent shear stress and gives highly accurate predictions of the onset and the amount of flow separation under adverse pressure gradients. The formulation of this two-equation type turbulence model is shown below.

k-equation:

$$\frac{\partial(\rho k)}{\partial t}+\nabla\bullet\left(\rho\vec{W}k\right)=\widetilde{P}_k-\beta'\rho k\omega+\nabla\bullet\left[\left(\eta+\frac{\eta_t}{\sigma_{k3}}\right)\nabla k\right] \tag{2.103}$$

ω-equation:

$$\frac{\partial(\rho\omega)}{\partial t}+\nabla\bullet\left(\rho\vec{W}\omega\right)=\alpha_3\frac{\omega}{k}\widetilde{P}_k-\beta_3\rho\omega^2+\nabla\bullet\left[\left(\eta+\frac{\eta_t}{\sigma_{\omega3}}\right)\nabla\omega\right] \\ +(1-F_1)2\rho\frac{1}{\sigma_{\omega2}\omega}\nabla k\nabla\omega \tag{2.104}$$

All coefficients, which are given by the model, are listed again in sake of completeness:

$\beta'=0.09$

$\alpha_1=\frac{5}{9}$

$\beta_1=0.075$

$\sigma_{k1}=2$

$\sigma_{\omega1}=2$

$\alpha_2=0.44$

$\beta_2=0.0828$

$\sigma_{k2}=1$

$\sigma_{\omega2}=1/0.856$

The model constants are calculated using the F_1 blending function.

$$\Phi_3=F_1\Phi_1+(1-F_1)\Phi_2 \tag{2.105}$$

The blending functions represent the core feature of this method. Their formulation is based on the distance to the nearest surface and on the flow variables. The blending function F1 is defined as

$$F_1 = \tanh\left(\arg_1^4\right) \text{, with} \tag{2.106}$$

$$\arg_1 = \min\left(\max\left(\frac{\sqrt{k}}{\beta'\omega y}, \frac{500\nu}{y^2\omega}\right), \frac{4\rho k}{CD_{k\omega}\sigma_{\omega 2}y^2}\right) \tag{2.107}$$

where y is the distance to the nearest wall and ν is the kinematic viscosity and

$$CD_{k\omega} = \max\left(2\rho\frac{1}{\sigma_{\omega 2}\omega}\nabla k\nabla\omega, 1.0\times 10^{-10}\right). \tag{2.108}$$

Furthermore, the blending factor F2 can be defined as

$$F_2 = \tanh\left(\arg_2^2\right) \text{, } with \tag{2.109}$$

$$\arg_2^2 = \max\left(\frac{2\sqrt{k}}{\beta'\omega y}, \frac{500\nu}{y^2\omega}\right). \tag{2.110}$$

To prevent the build-up of turbulence in the stagnation regions, a turbulence production limiter is used.

$$\widetilde{P}_k = \min\left(P_k, 10\beta'\rho k\omega\right) \tag{2.111}$$

with turbulence production:

$$P_k = \eta_t\nabla\vec{W}\bullet\left(\nabla\vec{W}+\left(\nabla\vec{W}\right)^T\right)-\frac{2}{3}\nabla\bullet\vec{W}\left(3\eta_t\nabla\bullet\vec{W}+\rho k\right)+P_{kb} \tag{2.112}$$

including the buoyancy production term P_{kb} that is modelled as:

$$P_{kb} = -\frac{\eta_t}{\rho\,\mathrm{Pr}_t}\vec{g}\bullet\nabla\rho \tag{2.113}$$

During the simulation with the SST model, a wall scale equation is solved additionally. This is due to the blending between *k-ε* and *k-ω*, which requires the distance of the node to the nearest wall. The wall scale equation is the equation solved to get the wall distance:

$$\nabla^2 \phi = -1 \tag{2.114}$$

where ϕ is the value of the wall scale. The wall distance is calculated from the wall scale through:

$$\text{Wall Distance} = \sqrt{\left(\left|\nabla\phi\right|^2 + 2\phi\right)} - \left|\nabla\phi\right| \tag{2.115}$$

Due to the lack of information about turbulence intensity under high pressure, the default inlet turbulence intensity of CFX is selected. The value is set to

$$I = \frac{w}{W} = 0.037\,. \tag{2.116}$$

Herein, w represents the fluctuating velocity component in the turbulent flow, and the magnitude of the velocity is denoted by W. The inlet turbulence energy is then calculated using

$$k_{inlet} = \frac{3}{2} I^2 W^2\,. \tag{2.117}$$

And the turbulence dissipation is calculated using

$$\varepsilon_{inlet} = \rho C_\eta \frac{k^2}{\eta_t}\ \varepsilon_{inlet} = \rho\, C_\eta \frac{k^2}{\eta_t} \tag{2.118}$$

with the k-ε Turbulence model constant C_η = 0.09, and

$$\eta_t = 1000 I \eta\,. \tag{2.119}$$

2.7 Equations for the Pressure Induced Biotechnological Conversion Process

In order to examine the consequences of the thermofluiddynamical processes during the high pressure processing onto the desired biotechnological conversion, especially the thermally induced process heterogeneity of the conversion process, additional variables must be introduced. In this work, additional variables are treated as scalar components which are subject to convective transport. They can be used to model, for example, the distribution of high pressure-inactivated substances.

The general form of the transport equation for an additional scalar is

$$\frac{\partial \phi}{\partial t} + \nabla \bullet \left[\phi \vec{W}\right] = \nabla \bullet \left(D_\phi \phi\right) + S_\phi \tag{2.120}$$

and in the presence of turbulence, the equation can be modelled as

$$\frac{\partial \phi}{\partial t} + \nabla \bullet \left[\phi \vec{W}\right] = \nabla \bullet \left(\left(\rho D_\phi + \frac{\eta_t}{Sc_t} \right) \nabla \bullet \left(\frac{\phi}{\rho} \right) \right) + S_\phi , \tag{2.121}$$

where ϕ represents the scalar solved in the equation. The kinematic diffusivity is denoted by D_ϕ. Sc_t is the turbulence Schmidt number, the density and the turbulence viscosity are denoted by ρ and η_t respectively. On the left side, the scalar is coupled with the velocity field, which is also coupled with the temperature field due to the buoyancy flow behaviour. The term S_ϕ on the right hand side represents the source term. In this case, this term can be implemented as the sinking term representing the inactivation of biological substances due to pressure and temperature.

The non-uniformity of the conversion process is substantially related to the time scale of the involved thermofluiddynamical processes. Since most conversion processes under high pressure are also temperature dependent, the existence of gradients during the entire high pressure process might lead to substantial non-uniformity in the conversion process. Generally, the risk of substantial heterogeneity is high if the time scale of hydrodynamic motion is small and the time scale of heat conduction is large compared to the time scale of the high pressure conversion process. This was discussed in detail by Hartmann and Delgado [46].

2.7.1 Inactivation of *Bacillus subtilis* α-Amylase

During the high pressure treatments, the disulfide bonds, which are very important to the folding, structure, and function of proteins, are disturbed. As a result of this, the three-dimensional structure of protein molecules are modified, and the protein molecules cannot maintain some of their functions. As in the case of enzymes, if the mentioned disturbances on the disulfide bonds occur, enzymes may lose their ability to convert substances into products. In other words, the enzyme activity is reduced due to high pressures and temperatures. Therefore, it is obvious that the structural change of the enzyme molecule directly correlates with the reduction of the enzyme activity. However, as it is difficult to measure the structural changes of the enzyme molecules, it is more convenient to measure the enzyme activity due to their direct correlation.

In this study, the effect of thermally induced non-uniformity is investigated using a high pressure conversion model of Denys et al. [32]. This model describes the inactivation kinetics of an enzyme called *Bacillus subtilis* α-Amylase dissolved in a 0.01 M Tris-HCl buffer (pH 8.6) at a concentration of 15 g/l. The inactivation of this enzyme obeys the 1st order kinetics as examined by Ludikhuyze et al. [29, 30], and its inactivation rate depends on both pressure and temperature (see also Figure 13).

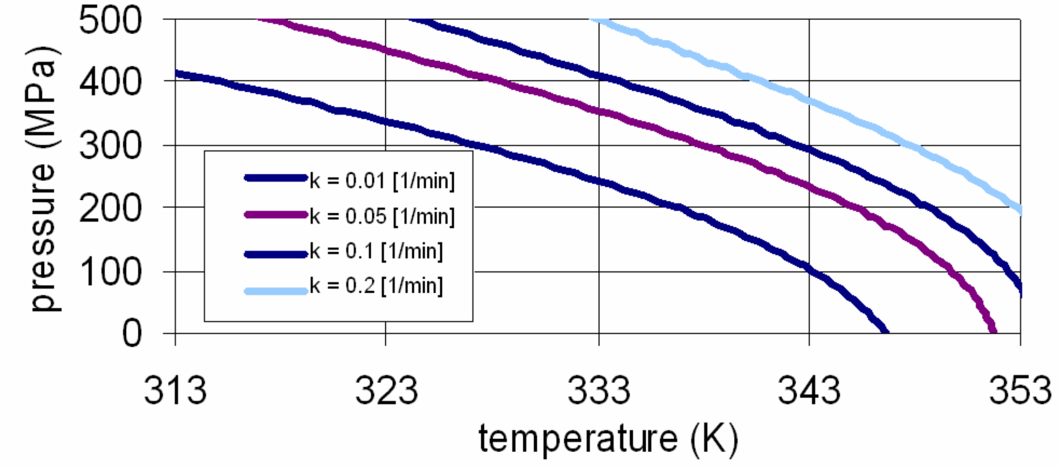

Figure 13: Inactivation rate k of the enzyme *Bacillus subtilis* α-Amylase in dependence of temperature and pressure [32]

The relative activity A (actual activity related to the initial activity) can vary between 1 (100%) and value close to zero. The inactivation rate k depends on the pressure level and the temperature and, therefore, is transient.

Furthermore, it is assumed that the enzymes are dissolved in water homogeneously, so that no concentration gradient occurs. As mentioned earlier, enzyme molecules are destroyed or split during the high pressure treatment, as high pressure induces structural changes of the enzyme molecules only. As no enzyme molecules are destroyed, no concentration gradient of the enzyme molecules can be expected here either. Therefore, the kinematic diffusivity of this enzyme is assumed to be zero in the numerical simulation.

2.7.2 Inactivation of lactic acid bacteria

Furthermore, the inactivation process of microorganisms in an industrial-scale high pressure autoclave should also be studied. *L. lactis* is a bacteria that can be found in different types of food, thus the behaviour of this bacteria under high pressure was studied by several authors:

According to Kilimann et al. [101], *L. lactis* exhibits maximum resistance to pressure when treated at a temperature of approximately 10 K below the growth temperature, resulting in the strong baroprotective population exhibiting the so called “tailing” behavior. The population exhibiting the tailing behavior is resistant to a level of pressure at a certain temperature. No matter how long the population is exposed to pressure, no increased inactivation can be achieved. This survival population of bacteria can be crucial when the safe design of high pressure process is considered.

However, it could be shown that a temperature upshift from ambient temperature of 293 K to 313 K virtually eliminated the tailing behavior. A significant tailing in bacterial pressure inactivation kinetics was frequently reported, and the level of the pressure resistant fraction of the population was found to be independent of the medium pH, the ethanol concentration, and sucrose levels [102, 103, 104]. Because the presence of pressure-resistant fractions within populations of target organisms may hinder the application of pressure processes in food production, the possibility of eliminating strong tails in survivor curves by a mildly elevated temperature seems to be necessary.

Thus, the inactivation kinetics of the lactic acid bacteria *Lactococcus lactis* ssp. *cremoris* MG 1363 developed by Kilimann et al. [119] will be additionally implemented to demonstrate the effects of thermofluiddynamical heterogeneities on the inactivation process of bacteria. This model, developed at the Chair of Fluidmechanics and Process Control, can describe the inactivation process of *L. lactis* in three different matrices; neutral matrix, one with 4M NaCl and with 1.5 M sucrose addition. Furthermore, this model is capable of predicting both the viable cell counts and stress resistant cell counts of *L. lactis*, thus suitable for discussing the issues concerning the safe design of a high pressure system in industrial applications.

2.7.3 Dimensionless transport equation for an additional scalar

In order to obtain the dimensionless transport equation for an additional variable, an additional dimensionless number must be defined.

$$\phi^* = \frac{\phi}{\phi_0}. \tag{2.122}$$

With this dimensionless variable for an additional variable, i.e. activity of enzymes for the cell counts of microorganisms, the dimensionless transport equation with a 1st-order kinetic inactivation source term with the inactivation rate $k = k_0 k^*$ can be described as:

$$\begin{aligned} &\frac{W_0\phi_0}{L_0}\frac{\partial \phi^*}{\partial t^*} + \frac{W_0\phi_0}{L_0}\frac{\partial \phi^* W_x^*}{\partial x^*} + \frac{W_0\phi_0 D}{L_0 D}\frac{\partial \phi^* W_y^*}{\partial y^*} = \\ &\frac{D_{\phi 0}\phi_0}{L_0}\frac{\partial}{\partial x^*}\left(D_\phi^*\frac{\partial \phi^*}{\partial x^*}\right) + \frac{D_{\phi 0}\phi_0}{L_0}\frac{\partial}{\partial x^*}\left(\frac{L_0}{D}D_\phi^*\frac{\partial \phi^*}{\partial y^*}\right) - k_0 k^* \phi_0 \phi^*. \end{aligned} \tag{2.123}$$

By multiplying the equation (2.122) with $\frac{L_0}{W_0\phi_0}$, the equation can be rewritten as:

$$\begin{aligned} &\frac{\partial \phi^*}{\partial t^*} + \frac{\partial \phi^* W_x^*}{\partial x^*} + \frac{\partial \phi^* W_y^*}{\partial y^*} = \\ &\frac{D_{\phi 0}}{W_0}\left[\frac{\partial}{\partial x^*}\left(D_\phi^*\frac{\partial \phi^*}{\partial x^*}\right) + \frac{L_0}{D}\frac{\partial}{\partial x^*}\left(D_\phi^*\frac{\partial \phi^*}{\partial y^*}\right)\right] - \frac{L_0}{W_0}k_0 k^* \phi^*. \end{aligned} \tag{2.124}$$

The importance of each term of this equation is explained in the following Table 7.

Table 7: Importance of each term in the dimensionless transport equation of for a 1st order kinetic inactivation

Term	Importance
$\frac{\partial \phi^*}{\partial t^*}$	Local change of the additional variable
$\frac{\partial \phi^* W_x^*}{\partial x^*} + \frac{\partial \phi^* W_y^*}{\partial y^*}$	Convective transport
$\frac{D_{\phi 0}}{W_0}\left[\frac{\partial}{\partial x^*}\left(D_\phi^* \frac{\partial \phi^*}{\partial x^*}\right) + \frac{L_0}{D}\frac{\partial}{\partial x^*}\left(D_\phi^* \frac{\partial \phi^*}{\partial y^*}\right)\right]$	Diffusive transport
$-\frac{L_0}{W_0} k_0 k^* \phi^*$	Source term

3 NUMERICAL METHODS

3.1.1 Meshing

The geometry of a vertical 3.3-liter autoclave is recreated and meshed with the commercial software ICEM CFD4.CFX. This autoclave, in courtesy of Institut ENITIAA, Nantes, has an inner diameter of D = 12 cm and an inner height of L_0 = 31 cm. The inlet of this autoclave has a diameter of d = 3 mm and is placed at the bottom in the middle of the autoclave. The wall of this autoclave is made of steel, and the distance between the inner walls to the temperature liquid is 9 cm.

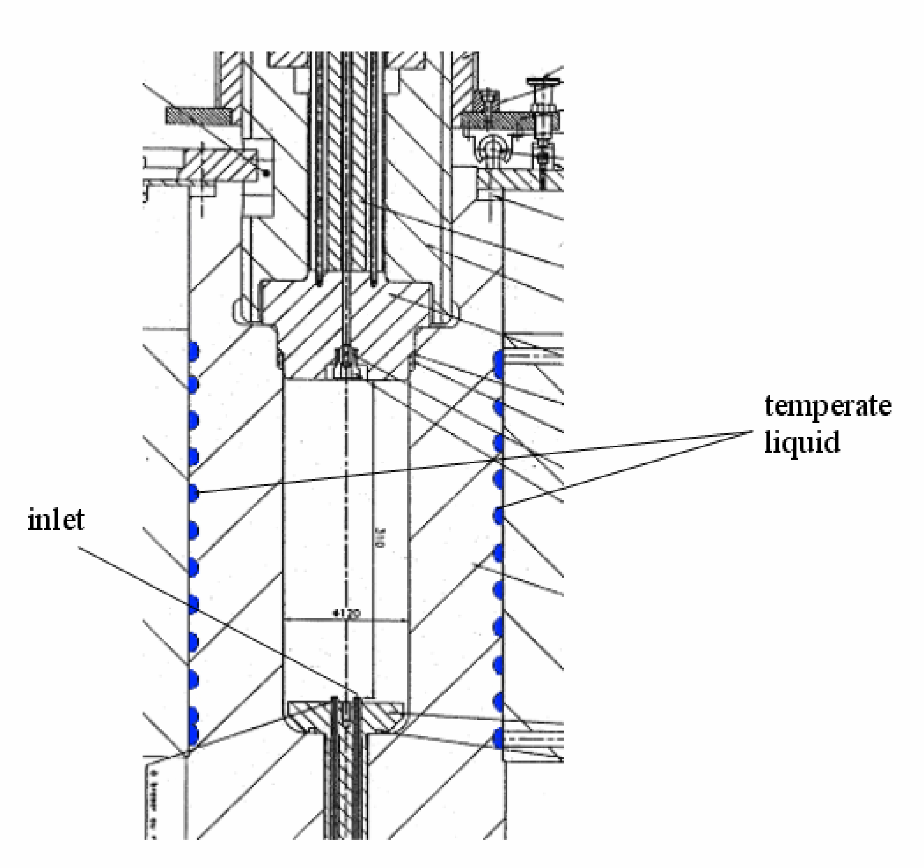

Figure 14: An engineering drawing of a 3.3-litre autoclave (Insitut ENITIAA, Nantes)

However, to make use of the rotational symmetry of the autoclave, only one twelfth of the model is considered, resulting in substantial reduction of computational costs. The mesh assemblies, which should represent both the pressure fluid and the wall of the autoclave, are created by the program ICEM CFD4.CFX^{TM} (compare Figure 15 and Figure 16).

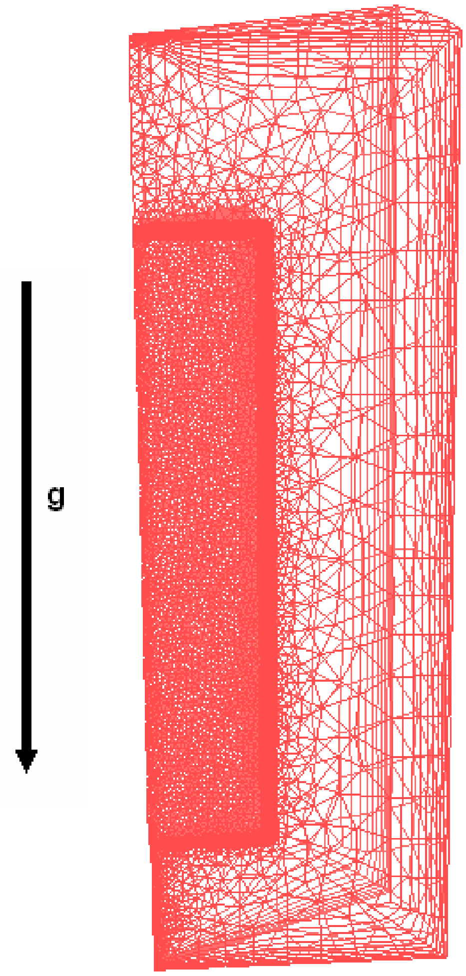

Figure 15: Mesh assembly representing 1/12 of a vertical high pressure autoclave

Firstly, the “fine” mesh shown in Figure 15 consists of 162,873 elements accounting for 57,389 nodes, of which approx. 2/3 represent the fluid and 1/3 the solid domain. As finer meshes with over approximately 200,000 elements constantly cause the used solver to experience memory overrun, this is the finest possible mesh at the moment. The memory overrun may be caused due to additional memory allocation for the own FORTRAN 90 subroutines used in this work, as the runs without these subroutines do not suffer from memory overruns even with significantly finer meshes.

Due to the transport equations solved in the fluid domain, the elements of the mesh must be smaller here compared to those in the solid domain, where only the heat transfer is considered. Most of the elements are tetrahedral, whereas prisms and wedges are implemented in regions, where a finer mesh is required in order to ensure the convergence. Also at the region next to the inlet at the bottom, the smallest tetrahedeal elements with 0.7 mm side length are used to ensure the correct calculation of the free jet. Particularly to ensure the accuracy of both the heat transfer between both domains and the wall scale equation solved in the SST-turbulence model, 10 layers of prisms, with heights of approx. 0.7 mm, are created at every boundary patch and especially at the interface between the fluid and the solid domain.

Secondly, the "coarse" mesh, which represents the same geometry as the fine mesh shown in Figure 15, consists of 49,046 elements accounting for 11,261 nodes (not shown here), of which approx. 2/3 represent the fluid and 1/3 the solid domain. This mesh is supposed to be used as a "fast solution" especially when the correctness of the fluid movement is not of great importance. However, the importance of the mesh refinement and its influences on the correctness of the solutions will be discussed at a later point.

Last but not least, a mesh assembly for a horizontal high pressure autoclave is generated. This mesh consists of approx. 205,926 elements accounting for 83,406 nodes. Despite the larger number of elements and nodes compared to the "fine" vertical mesh, this mesh represents only half of the autoclave, since no rotational but only an axisymmetry can be considered here. Therefore, most of the elements used in this mesh are larger than those used in the vertical meshes. Thus, the solutions gathered with this mesh might not be as accurate as those of the "fine" vertical mesh. However, a numerical simulation of a horizontal autoclave with this mesh should give first impressions of which thermofluiddynamical processes can occur during the high pressure treatments of food in such autoclaves.

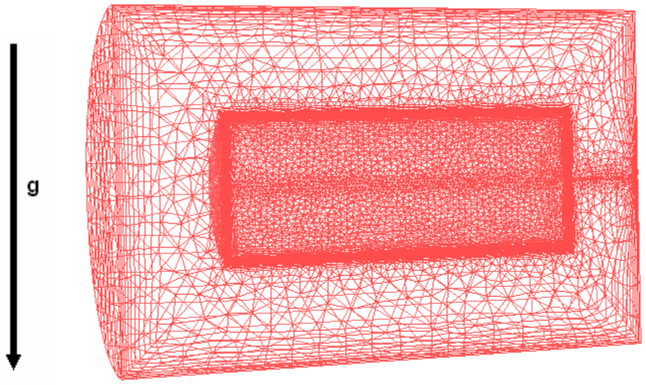

Figure 16 : Mesh assembly representing half of a horizontal high pressure autoclave

3.1.2 Solution Technique

The commercial finite volume code CFX-5.7 is employed in this work. The numerical simulation is carried out using both personal computers with Windows XP and Linux workstations with SUSE Linux-9.3. The general solution procedure of this code is shown in Figure 17.

The CFX-package includes the pre-processor CFX-Pre, where the geometry and the boundary conditions can be defined. The non-structured grid based double precision CFX-Solver is subsequently used to solve all the equations for the high pressure processes. Depending on the geometry, the defined conditions and the computer used, a simulation of a high pressure treatment with compression, pressure holding time and decompression can be carried out within 2 weeks with a normal Pentium IV personal computer or within three days with a dual-processor Linux machine.

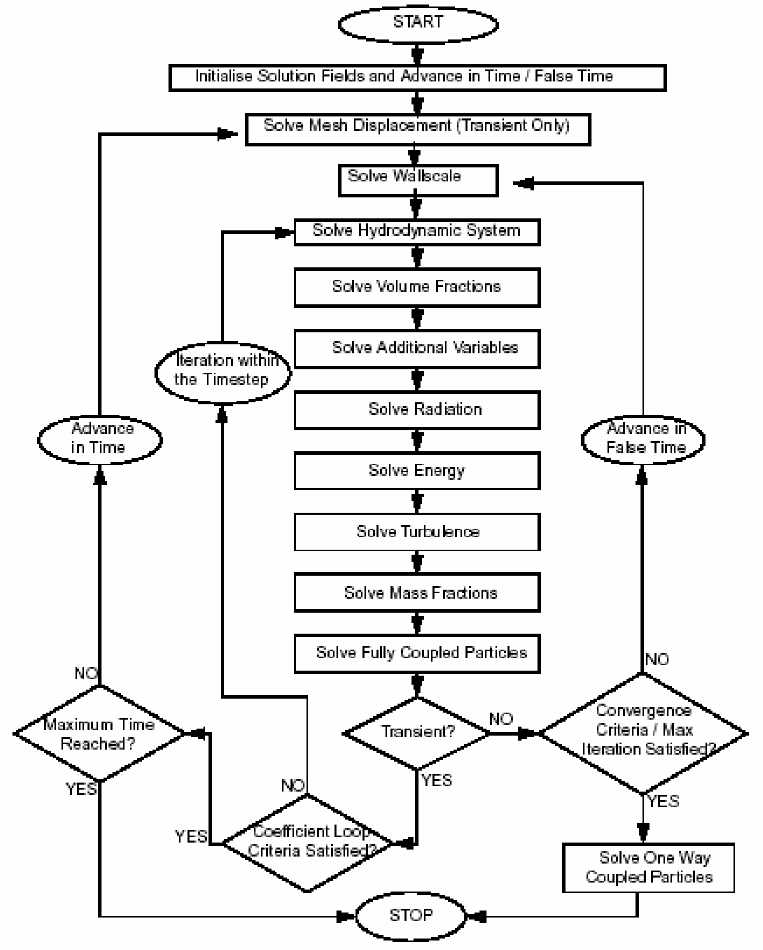

Figure 17: General solution procedure of CFX-Solver

The main reason for the long computational time is the difficulty in reaching the convergence solving the energy equation during the compression and the decompression phase. This requires the solver to solve the equations with a small timestep of 0.1 seconds in order to ensure the convergence. Even with this small timestep, the solver requires more than 10 iterations for each timestep. On the contrary, during the pressure holding phase larger timesteps of up to 0.5 seconds can be chosen, and only 2 or 3 iterations are required to acquire the convergence.

The analysis of the result files is carried out with the post processing program CFX-Post, which allows for a detailed analysis of the transient results obtained from CFX-Solver.

3.1.3 Discretisation of the governing equations

Advection scheme

The advection schemes implemented in CFX-5 can be cast in the form:

$$\phi_{ip} = \phi_{up} + \beta \nabla \phi \cdot \Delta \vec{r} \, , \tag{3.1}$$

where ϕ_{up} is the value at the upwind node, $\nabla \phi$ is the gradient of ϕ and $\vec{r}$ is the vector from the upwind node to the integration point *ip*. Particular choices for β give rise to different schemes.

A value of $\beta = 0$ leads to the first order Upwind Difference Scheme (UDS). Many difference schemes developed for CFD are based on series expansion approximations (such as the Taylor series) for continuous functions. The more terms of the expansion used in the difference scheme, the more accurate the approximation will be. The order of the scheme used is denoted by the order of the largest term in the truncated part of the series expansion. UDS is very robust and guarantees to not introduce non-physical overshoots and undershoots. However, it is also susceptible to a phenomenon known as Numerical Diffusion or “gradient smearing”.

By choosing a value for β between 0 and 1, the diffusive properties of UDS are reduced. The quantity $\beta \nabla \phi \cdot \Delta \vec{r}$, called the Numerical Advection Correction, may be viewed as an anti-diffusive flux added to the upwind scheme. The choice β = 1 is formally second order accurate. The disadvantages of these schemes are that they may be less robust than UDS and may display non-physical overshoots and undershoots in the solution, especially in the regions of sharp gradients.

The High Resolution Scheme computes β locally to be as close to 1 as possible without violating boundedness principles. The recipe for β is based on that of Barth and Jesperson [105]. The high resolution scheme is therefore both accurate (reducing to first order near discontinuities and in the free stream where the solution has little variation) and produces bounded solutions. Note that for vector quantities it is the components that are bounded between 0 and 1. Therefore the magnitude of β for a vector quantity can be as large as $\sqrt{3}$.

Transient scheme

The transient scheme defines the discretization algorithm for the transient term. Options available in CFX-5.7 are First Order Backward Euler and Second Order Backward Euler. The First Order Backward Euler scheme is an implicit time-stepping scheme which is first order accurate. Its behavior is analogous to the Upwind Differencing scheme for advection terms, and suffers from similar numerical diffusion. The First Order Backward Euler scheme approximates the transient term as:

$$\frac{\partial}{\partial t}\left(\int_v \rho\phi dv\right) = \rho V\left(\frac{\phi - \phi^0}{\Delta t}\right), \tag{3.2}$$

where ϕ^0 refers to the value of the variable at the prior time level.

The Second Order Backward Euler scheme is also an implicit time-stepping scheme, but is second order accurate, and is the default in CFX-5 applied in this work. This scheme approximates the transient term as:

$$\frac{\partial}{\partial t}\left(\int_v \rho\phi dv\right) = \frac{\rho V}{\Delta t}\left(\frac{3}{2}\phi - 2\phi^0 + \frac{1}{2}\phi^{00}\right). \tag{3.3}$$

where ϕ^{00} represents the solution field from the time step before the prior time level. This scheme is also robust, implicit, conservative in time, and does not create a time step limitation. It is applicable for constant and variable time step sizes. Like second-order advection schemes, however, it is not monotonic and is therefore inappropriate for some quantities which must remain bounded, such as turbulence quantities and volume fractions. Therefore, when running the Second Order Backward Euler scheme, the transient scheme for turbulence equations will remain First Order, and the transient scheme for volume fraction equations will be set to a bounded second order scheme, similar to the High Resolution scheme for advection.

3.1.4 Convergence Criteria

The residual is a measure of the local imbalance of each conservative control volume equation. It is the most important measure of convergence as it relates directly to whether the equations have been solved. If the normalized residuals are reduced in the iterations so that a desired level of convergence criteria is reached, the equations are solved for the current timestep, and the next timestep can begin.

In this work, the root mean square (RMS) residual is considered. For engineering applications, the convergence criterion of 10^{-4} is considered sufficient and, therefore, is applied in this work. The maximum number of iterations for each timestep is set at 25.

3.1.5 Initial and Boundary Conditions

At the beginning, the temperature of the whole system including both the fluid and the solid domain is set to the same constant value (see also Figure 18). The fluid is assumed to be at rest. The activity of the dissolved enzyme at the beginning is set to be at 1 (100%). The autoclave is tempered at a constant process temperature throughout the whole high pressure treatment. The pressure of $p^* = 1$ (500 MPa) is built up with inflowing fluid at a constant process temperature at different speeds in order to generate different flow behaviors.

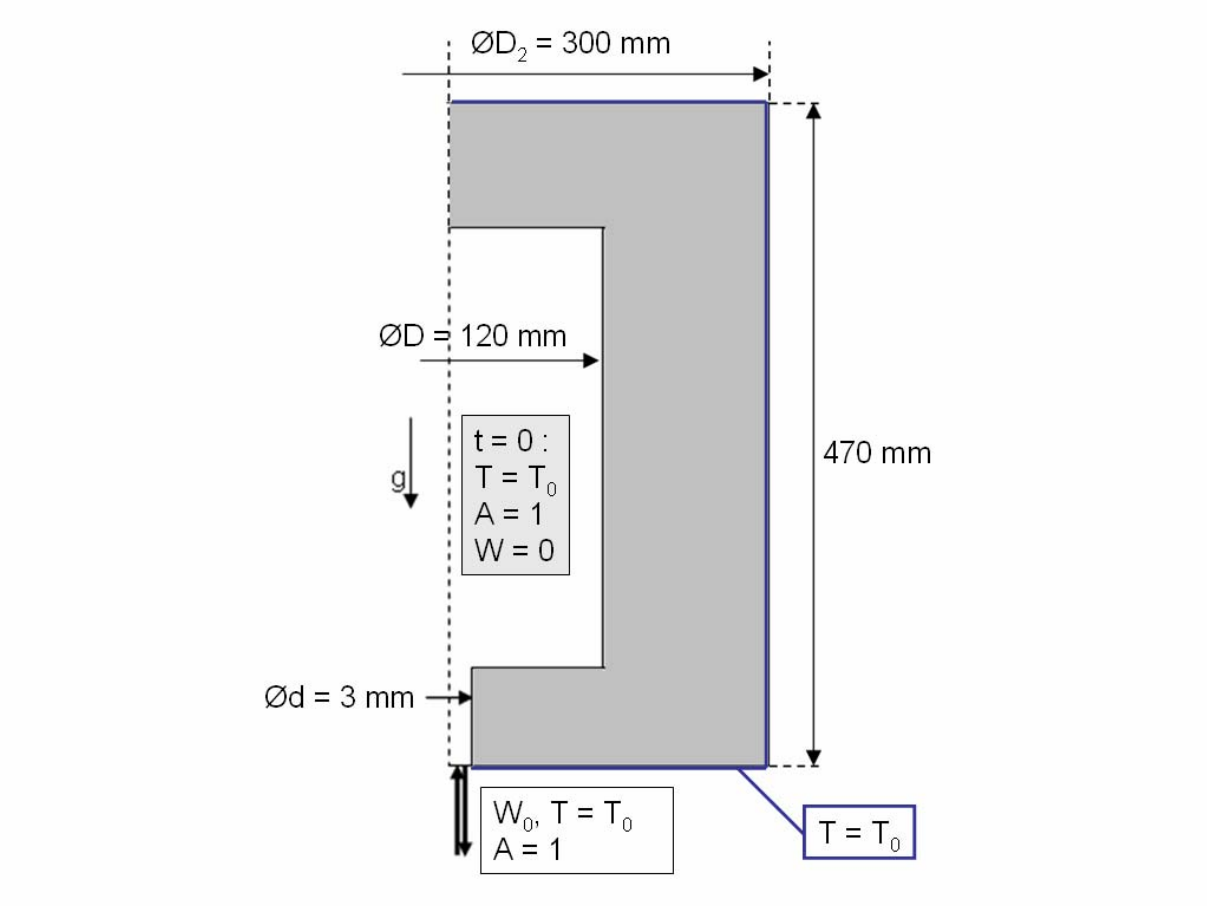

Figure 18: Initial and boundary conditions

Due to the temperature increase of the fluid inside of the autoclave, the inner steel wall of the autoclave also becomes warmer. This temperature increase of the steel wall is local and transient, and thus, needs to be calculated for each timestep. This, however, can also be solved with the CFX solver. By coupling the fluid and the solid domain together combined with the wall scale equation of the SST turbulence model used, an accurate solution of the flow throughout the whole high pressure chamber can be carried out.

3.1.6 Implementation of the fluid properties and additional source terms

The properties of water explained in section 2.3 and the inactivation kinetics for *L. lactis* and for the enzyme *Bacillus subtilis* α-Amylase explained in section 2.7.1 are implemented into the main CFX-code as FORTRAN90 routines. The FORTRAN files are compiled by the Compaq FORTRAN Compiler Version 6.0 as shared libraries, which can be linked to the main code at several interfaces. Figure 19 shows the concept of the linkage between the CFX-solver and the libraries.

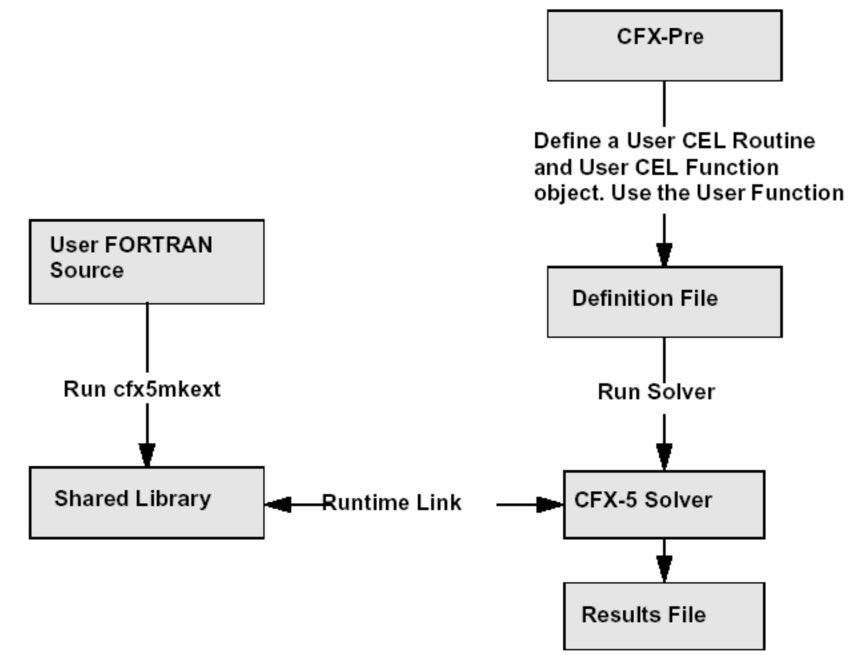

Figure 19: The concept of the linkage between CFX-Solver and the shared libraries.

The user-defined function passes an argument list to a subroutine, which contains the information of the quantity of interest and is compiled as a shared library by the compiler. Subsequently, the user-defined function then uses the returned values from the subroutine to set values for the quantity of interest.

3.1.7 Particle Tracking Simulation

A multiphase flow containing dispersed particles may be modelled using either the particle transport model or the Eulerian-Eulerian multiphase model. However, if complete information on behaviour and residence time of individual particles is of interest, the particle transport model must be considered.

In this work, the particle transport model of ANSYS CFX-10 is used for the simulation of the movements of dissolved particles in the fluid, i. e. enzyme molecules. Due to the small size of the enzyme molecules compared to the continuous phase “water”, one-way coupling is considered as the small molecules are dissolved completely by the continuous phase. It simply predicts the particle paths as a post-process based on the flow field and therefore it does not influence the continuous phase flow field. Therefore, one-way coupled particles are tracked only once, at the end of the solver run.

However, since the size of such enzyme molecules is so small in comparison to the grid size, it is assumed that the enzyme molecules travel with the same velocity as the surrounding water. Therefore, the simulation consists of water as both continuous and dispersed phase. The Schiller-Naumann scheme [106] is considered calculating the drag forces, and the interphase heat transfer is discretised according to the Ranz Marshall scheme [107]. The diameter of the dispersed “water particles” are set at 1 mm.

4 RESULTS

The results shown in this work are organized in three parts. The first part consists of an analysis of the dimensionless equations solved during the numerical simulations. By comparing the orders of magnitude of each term, a better understanding of the importance of each thermofluiddynamical sub-process during a high pressure treatment can be achieved.

The second part of this work concerns the thermofluiddynamical processes during the compression and the pressure holding phase of the high pressure treatment. Especially the generation of turbulence due to the free jet inflow is a subject of study. Due to the mixing effects of the turbulence, the process non-uniformity is expected to be reduced. But it is still unknown how the turbulence interacts with the free convection occurring due to the cooling process. For this part, 3 different pressure ramps were chosen representing different flow regimes including both laminar flow and turbulent flow with free jet. Especially the effects on the direct pressure treatment of an enzyme were considered. The inactivation kinetics of this enzyme obeys the 1st order kinetics, and therefore, can also be used as a guideline for other enzymes or microorganisms with the same inactivation kinetics.

Last but not least, the last part of this work will illustrate the non-uniformity of thermofluiddynamical processes in a medium-sized high pressure autoclave and how it influences the high-pressure inactivation process of a microorganism. The microorganism used in this part is a lactic acid bacteria widely used in the production of fermented food. This part of the work was carried out in cooperation with Dr.-Ing. Klaus Kilimann, who works at the same research group as the author. The experimental part was carried out at Institut ENITIAA, Nantes by Dr. Kilimann, who also modelled the inactivation kinetics of *L. lactis* under high pressure. By combining the predictive modeling techniques of the inactivation of bacteria together with the High Pressure Computer Fluid Dynamics HP-CFD techniques, highly accurate predictions of the high pressure induced inactivation of *L. lactis* in 3 different food matrices in a medium sized high pressure autoclave are carried out. This part of the work focuses on the validation of the process non-uniformity during a high pressure inactivation of *L. lactis*. Overall, this work should contribute to the understanding of high pressure processes in a medium-sized high pressure autoclave. The knowledge obtained from this work should act as basis for real industrial applications, where much larger autoclaves with volumes as large as 500 liters will be applied. Especially the food safety should be subject of interest in every high pressure application, and thus, will be discussed in the last chapter of this work.

4.1 Approximation of the dimensionless groups

In order to understand the thermofluiddynamical processes during the high pressure treatment, the fundamental dimensionless thermofluiddynamic equations were considered. Especially the dimensionless numbers or groups are decisive for the importance of each sub-process of the high pressure treatment. Table 8 represents the estimated orders of magnitudes of the dimensionless groups found in the governing equations for forced convection shown in the sections 2.4.1.1-2.4.1.3. The estimations are based on the following data: T_0= 313 K, W_0(compression)= 1.5 m/s, W_{buoy}(holding phase) = 0.1 m/s, L_0= 0.31 m, D= 0.12 m, d= 0.003 m, c_{p0}= 4179 J/kgK, λ_0= 0.63 W/mK, α_0= 0.385×10^{-3} 1/K, η_0= 653×10^{-6} kg/ms, ρ_0= 992.21 kg/m^3.

Table 8 : Estimated orders of magnitude of dimensionless numbers or groups during forced convection

Dimensionless number or group	Order of magnitude
Ec	10^{-6}
$\frac{1}{Pe}\frac{d}{L_0}=\frac{1}{\Pr\mathrm{Re}}\frac{d}{L_0}$	10^{-7}
$\frac{Ec}{\mathrm{Re}}\frac{d}{L_0}$	10^{-12}
$\frac{Ec}{Fr}$	10^{-6}
$\frac{1}{\mathrm{Re}}\frac{d}{L_0}$	10^{-6}
1/Fr	1

It is obvious that especially the terms with the Eckert number seem to be the smallest ones. This is due to the relatively small velocity of the fluid. Especially the term $\frac{Ec}{\mathrm{Re}}\frac{d}{L_0}$ is the smallest term found in all the equations and represents the dissipation due to fluid friction. Thus, it can be concluded that only a small amount of kinetic energy is transformed to thermal energy, so that this term can be neglected in this case. However, there are high pressure application concepts, which plan to use very high pressure build-up rates. The velocities in such cases will be much higher than those in this work. Even then, however, the dissipation effects will not be substantial, as the velocities are still not high enough. The effects of the Reynolds and the Eckert number will be discussed thoroughly in the chapter 4.2.7.

Furthermore, the biggest term found here is the term 1/Fr, which represents the importance of the gravitational force in relation to inertial forces. Thus, it can be concluded that the gravity has a strong influence on the high pressure treatment. Pressure treatments under compensated gravity, however, would then be completely different from those under normal gravitation. This should be also shown in the next chapter.

Further dimensionless groups found in the dimensionless equations for free convection are listed in Table 9. Again, the terms with the Eckert number seem to be of less importance. Another term, which is relatively small, is the term 1/Ra due to very high Rayleigh number. Such high Rayleigh number means that the buoyant force dominates over the viscous drag and the heat diffusion, so that the heat diffusion can be neglected. This is confirmed by another important dimensionless group $Ar = \frac{Gr}{\mathrm{Re}^2}$ representing the ratio between the buoyancy forces and the convection, which is the dimensionless group with the 2nd largest magnitude found during the free convection. This means that the buoyancy force dominates throughout the pressure holding phase. According to these numbers, it becomes obvious that the gravity plays an extremely important role in the high pressure process. This and the effects of other dimensionless groups should be studied in detail in the following chapter, where several configurations of high pressure treatments will be examined and the effects of these dimensionless groups and numbers will be discussed in detail. However, regarding numerical aspects, it can already be concluded that there are terms, which are not significant and can be neglected in future studies. In spite of this knowledge, the author decides to solve the equations as they are without any simplification, so that the effects of all the terms can be explained in detail. In the following chapters, the effects of the thermofluiddynamical processes on the high pressure treatment of biological substances shall then be studied with the aim to be able to predict and gain information about such processes with high precision.

Table 9 : Estimated orders of magnitude of dimensionless numbers or groups during free convection

Dimensionless number or group	Order of magnitude
Ec	10^{-9}
$\frac{1}{Pe}=\frac{1}{\mathrm{Pr}\,\mathrm{Re}}$	10^{-7}
$\frac{Ec}{\mathrm{Re}}$	10^{-14}
$\frac{Ec}{Fr}$	10^{-6}
$\frac{1}{\mathrm{Re}}$	10^{-5}
1/Fr	10^{3}
1/Ra	10^{-10}
$\frac{Gr}{\mathrm{Re}^2}=Ga\alpha\Delta T\frac{1}{\mathrm{Re}^2}$	1
$\alpha_0 T_0$	10^{-2}

4.2 Thermofluiddynamical non-uniformity during the high pressure treatment

High pressure treatment of food occurs in high pressure autoclaves, which are normally made of metals. To endure high pressure levels up to 1000 MPa, the walls of autoclaves are normally very thick. Although the worldwide high pressure research activity is at its peak, still only little is known about the thermofluiddynamical processes inside the autoclave. The main reason is the difficulty in gaining insight of the autoclave in-situ. Although there are works involving the in-situ measurements of thermofluiddynamical process parameters in smaller autoclaves [12, 37, 38, 39, 36], it is still impossible to gain insight into the processes in larger high pressure autoclaves. Thus, numerical simulation plays an important role in understanding the thermofluiddynamical processes during the high pressure treatment.

It is known from both experiments and numerical simulations that temperature inside the autoclave rises locally as the pressure level increases. How high the temperature increases depends on many factors: start and process temperature, available tempering equipments, size of the autoclave, wall thickness, heat transport property of the wall, heat damping, and last but not least the fluid properties. Thus, these parameters must be considered while building up a model for the numerical simulations.

In order to relate the dimensionless time to the actual process time, the dimensionless time is transformed to 0(1) by deviding it with the largest time scale available, which is the duration of the pressure holding phase. The time t_0 remarks the end of the compression and the beginning of the pressure holding phase. Therefore, the transformed dimensionless pressure application time t_t* is introduced as follow:

$$t_t^* = \frac{t^* - t_0^*}{t_{Max}^*} = \frac{t^* - t_0^*}{t_{pressure\ holding}^*}. \tag{4.1}$$

Thus, due to this definition the time scale shown during the compression phase will have negative values, whereas the time scale of the pressure holding phase will be positive.

4.2.1 Preliminary study and proposed improvements

The numerical technique used in this work is introduced by Hartmann et al. [45, 46, 47, 48]. In the mentioned publications, numerical simulations of the thermofluiddynamical processes during a high pressure treatment of an enzyme solution are carried out using the Finite Volume code CFX-4.4 enhanced with own FORTRAN subroutines. Both experimental and numerical results confirm the existence of temperature gradients throughout the entire high pressure treatment. The temperature increase due to the external work done during the compression of the fluid is local and transient, leading to temperature gradients especially at the wall and in the middle of the autoclave, where the cold inflow jet is prominent during the compression phase (Figure 20). However, as more heat is removed by the wall with increasing process duration, the temperature gradients become smaller but still exist even after 20 minutes of high pressure treatment. During the compression phase, forced convection dominates due to the inflow fluid movement in the middle part of the autoclave. During the pressure holding phase, however, the free jet dissolves and free convection dominates due to the cooling process at the wall. Despite the assumption that the free water jet during the compression can cause turbulence and that the free jet is not stable, no turbulence model is applied here. Furthermore, in one of the author's publication [49] the validation of the temperature distribution is also carried out with thermocouples at different positions in the autoclave.

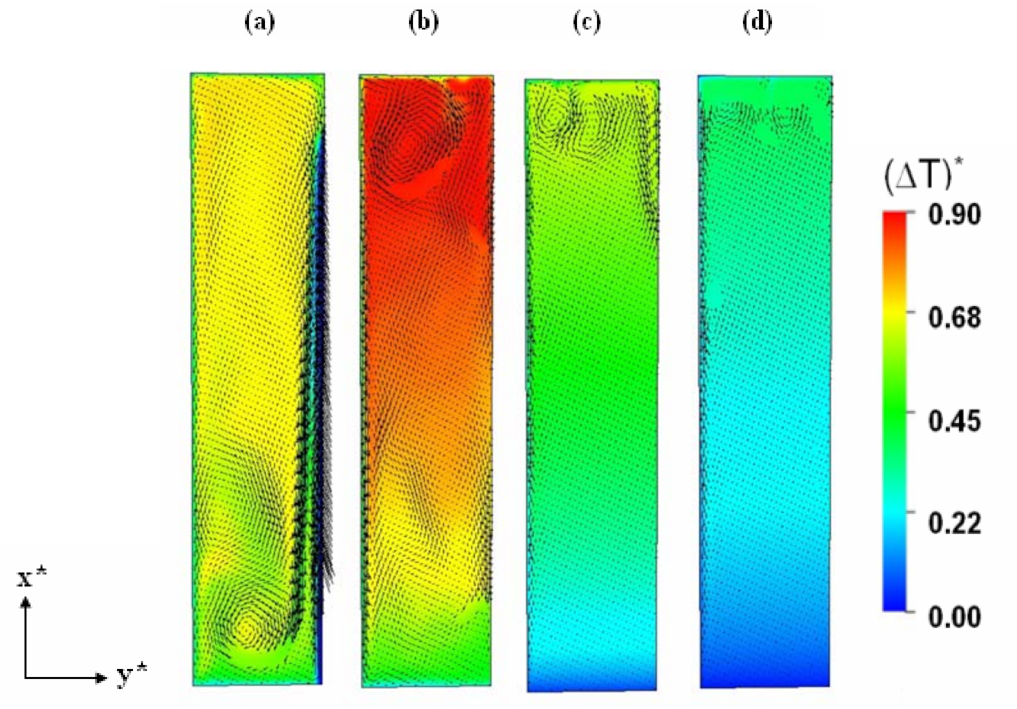

Figure 20 : Temperature and velocity at $t_t^* = -0.22$ (a), $t_t^* = 0.0$ (b), $t_t^* = 0.39$ (c) and $t_t^* = 0.78$ (d) for process with p* = 1 final pressure and a linear pressure ramp at $Re_d = 1900$ [49]. $(\Delta T)^*$ is according to the definition the actual temperature increase in relation to the adiabatic temperature increase. The negative time value of t_t^* for (a) and (b) is a consequence of the definition according to the equation (4.1), which imposes the time level at the end of pressurization.

For the first time, the thermal non-uniformity in a medium-sized high pressure autoclave can be both experimentally and numerically confirmed. Excellent agreement between the calculated and the measured temperature can also be observed (see also Figure 21).

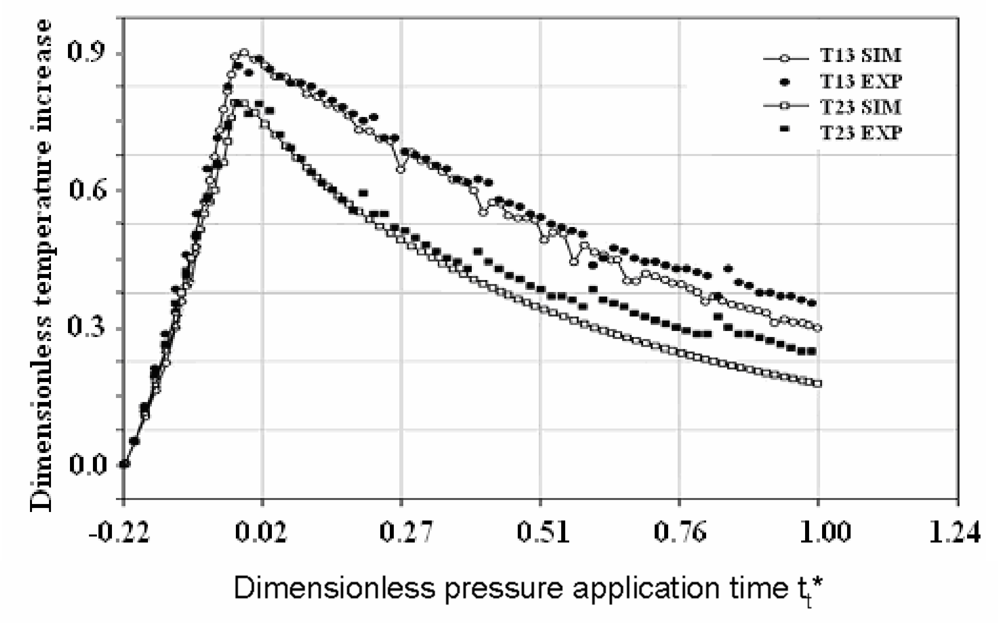

Figure 21: Temperature comparison between the experiments (EXP) and the numerical simulations (SIM) at two measurement points show good agreement [49]. T13 and T23 denotes the measuring positions at the upper end and at half the height of the autoclave respectively.

However, the numerical model proposed in the mentioned contribution has some flaws. Firstly, although the flow in the autoclave is supposed to be turbulent, no turbulence model is used due to some restrictions of the models. Furthermore, due to the absence of the turbulence model, the motions of the free jet of the inflowing fluid can not be satisfactorily solved. Secondly, temperature of the inner wall of the autoclave can be calculated with the finite difference method in an external program. However, it would be more convenient to have a single model which solves both the fluid motions and the heat transfer between the fluid and the solid structure at the same time. Last but not least, the model here works in two dimensions due to the rotational symmetry of the autoclave. However, there are autoclaves, whose geometry cannot be considered as a rotational symmetric one. In particular, the horizontal autoclaves have only an axisymmetry.

Therefore, the aim of this work is to optimise the methods proposed in the previous publication in order to study a three dimensional flow inside a 3.3 liter autoclave. One single model will be developed to solve both the fluid motions and the heat transfer between the fluid and the wall. Furthermore, a turbulence model shall be implemented in order to solve the motions of both the fluid jet during the compression phase and free convections throughout the entire high pressure processing. By implementing a model for a high pressure inactivation of enzymes, the influences of the thermofluiddynamical processes occuring during the pressure treatment on the mass conversion process can be discussed. Especially the effectivity and the heterogeneity of the mass conversion process must be examined thoroughly. In order to achieve this, several characteristic dimensionless groups of the fundamental equations solved during the simulations of high pressure processing will be discussed.

4.2.2 Mesh study

As mentioned in chapter 3.1.1 two different meshes for a 3.3 l vertical high pressure autoclave are created. The "fine" mesh consists of approx. 160,000 elements, whereas the "coarse" mesh includes approx. 50,000 elements. In order to examine the accuracy of these two meshes, numerical simulations for a high pressure processing with the same initial and boundary conditions are carried out with these meshes. The results shown in Figure 22 reveal some deviations of the fluid movements, particularly the generation and dissipation of vortices especially in the upper part of the autoclave cannot be solved with the "coarse" mesh.

Therefore, the "coarse" mesh fails to predict such cases, where the motions of the fluid are of interest. Here in particular, when the generations of vortices or the topology of the free jet must be considered, the finest possible mesh must be used.

However, considering the temperature distribution, the results of the two meshes are very similar. Therefore, in cases where only the temperature distribution of the fluid is of interest, the "coarse" mesh might also be considered. One advantage of chosing the "coarse" mesh is the huge reduction of the computational time and costs. Having only one third of the elements compared to the "fine" mesh, numerical simulations with the "coasen" mesh allowfor a reduction of computational time and costs by 67%.

For instance, if a pressure and temperature dependent inactivation process of microorganisms is not subject of diffusive and convective transport, this mesh can be used. At a later point of this work, the high pressure inactivation process of bacteria called *L. lactis*, which are immobilised in a small tube and not subject of diffusive or convective transport, this “coarse” mesh will be used. The decision to use this “coasen” mesh saves huge computational costs, while satisfactory results can also be obtained. Considering more than 50 simulations producing 50 GB of data are carried out only for this mentioned part with the “coarse” mesh, this would have produced much larger data with the “fine” mesh.

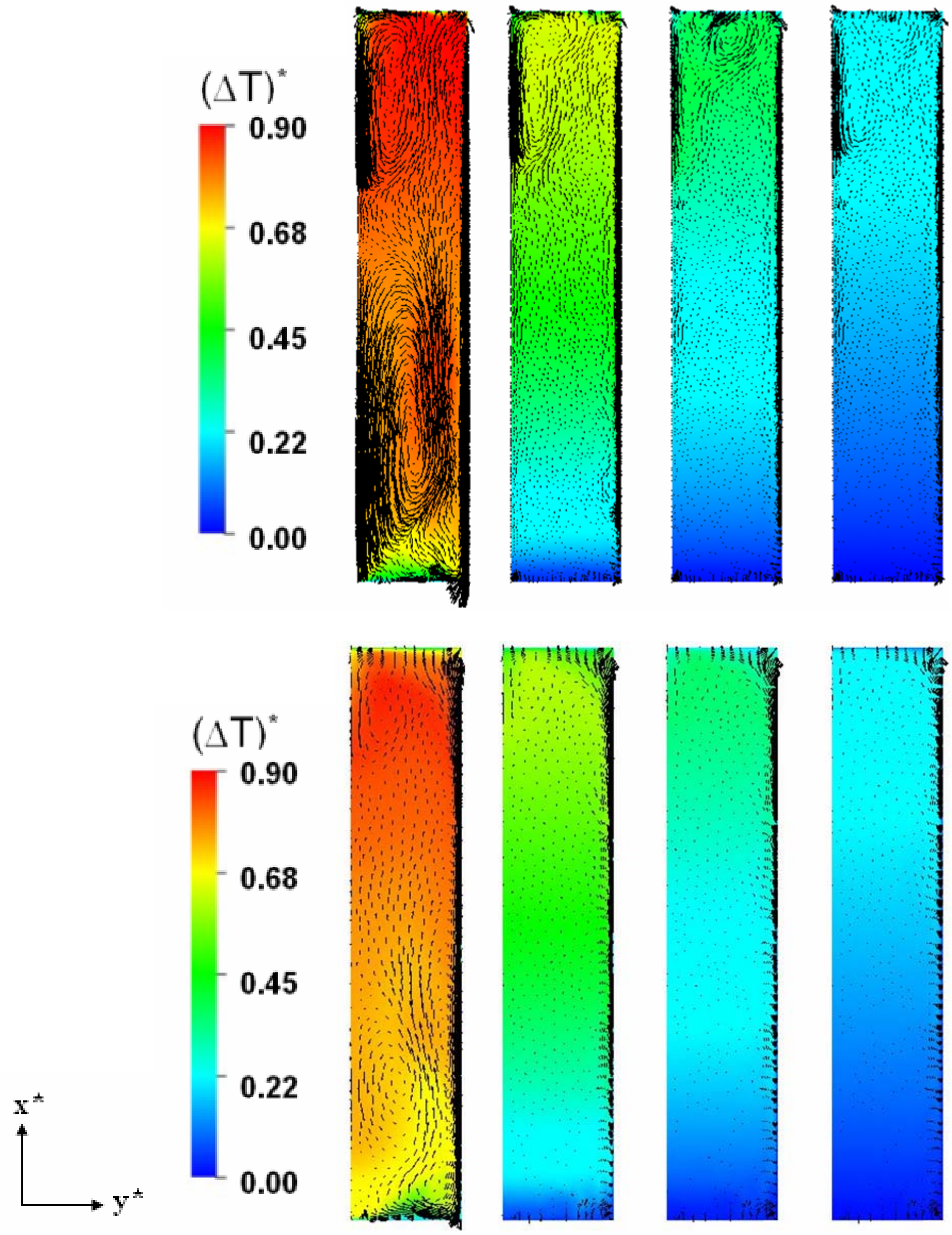

Figure 22: Comparison between the “fine” mesh with approx. 160,000 and “coarse” mesh with 50,000 elements reveals some deviations in the fluid movements but only minimal differences in the temperature distributions are observed.

4.2.3 Reference case

At the beginning of the simulation, the temperature of the whole system including the steel wall of the autoclave and the fluid inside the autoclave is constantly tempered. During the pressure treatment, the outer wall of the chamber and the inflowing fluid are also constantly tempered throughout the experiments, therefore the temperature increase at the outer wall of the autoclave is always at $(\Delta T)^* = 0$. The target pressure of $p^* = 1$ is built up by inflowing fluid of the same temperature at $\mathrm{Re_d} = 2279$.

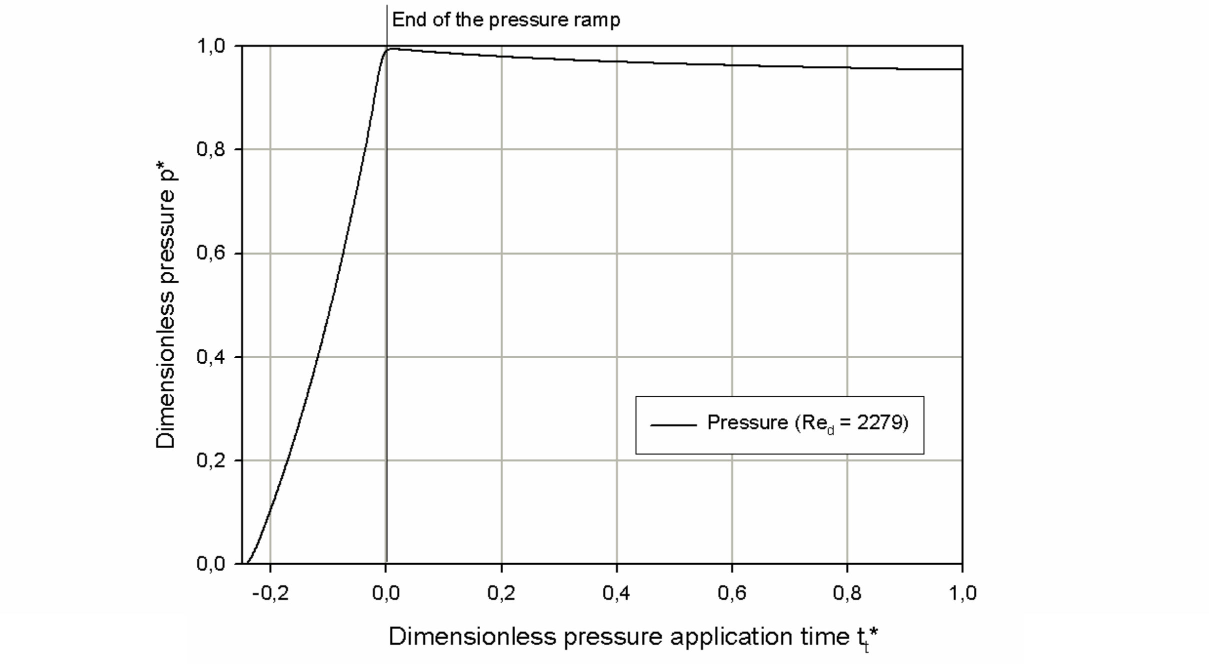

Figure 23 : Pressure history during the proposed reference model. The target pressure is built up within $t_t^* = 0.25$ and maintained for $t_t^* = 1.0$.

For the clarity of this work, the thermofluiddynamics of the reference case shall be treated in two separate parts: compression and the pressure holding phase. The decompression phase has the same characteristics as the compression phase and shall not be discussed here. During the compression phase, the flow is dominated by the forced convection due to the inflowing pressure fluid causing a free jet. However, as the temperature gradient inside the autoclave becomes prominent, free convections gain the upper hand during the pressure holding phase, where no additional pressure fluid enters into the autoclave.

4.2.3.1 Compression phase

The fluiddynamics of the process are dominated by the forced convection due to the inflowing fluid jet (see also [37, 38, 39]). The original inflow velocity of $W_x = 1$ gradually decreases with the height of the autoclave as the jet expands. This can be explained with the continuity equation (eq. 2.60). According to the numerical simulation, there appears to be a region between the inlet at the bottom and $x^* \approx 0.1$, where the velocity component in the x-direction of the free jet decreases almost linearly (compare Figure 24). Beyond this region, however, the velocity still decreases with different behaviors. This indicates the effects of additional forces during the compression phase, which must be considered.

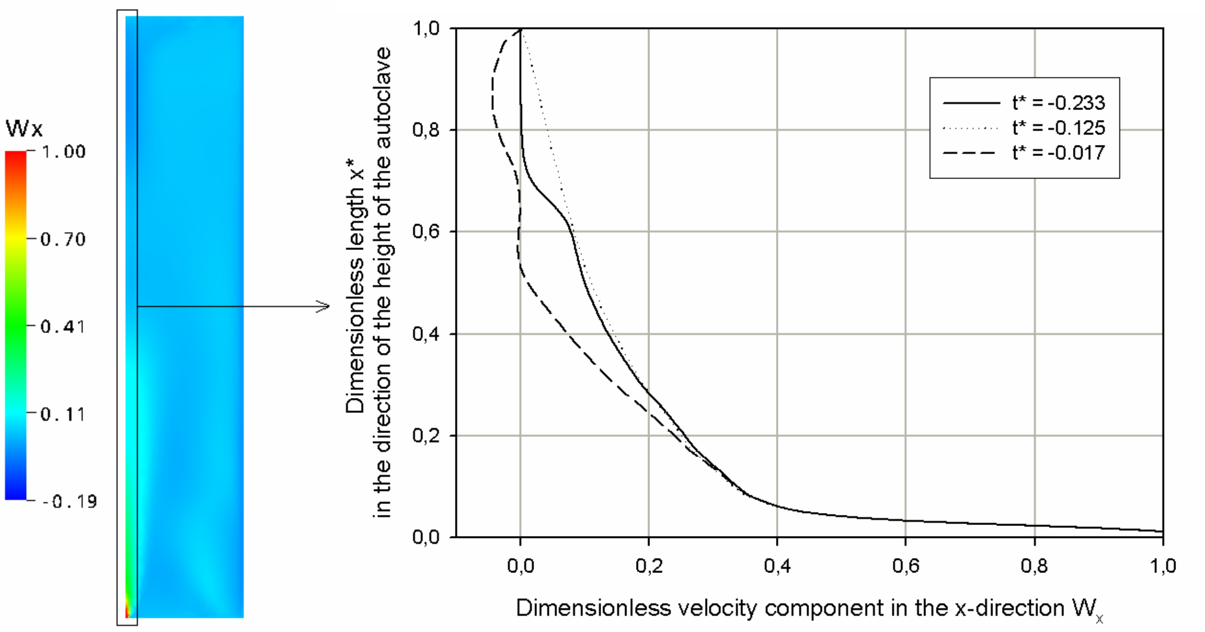

Figure 24 : Velocity distribution towards the end of the compression phase ($t_t^* = -0.017$) and velocity profiles in the middle of the autoclave (at $y^* = 0$) shortly after the beginning ($t_t^* = -0.233$), in the middle ($t_t^* = -0.125$) and towards the end of the compression phase ($t_t^* = -0.017$) from left to right respectively ($Re_d = 2279$).

Considering the penetration length of the free jet, transient jet penetration can be observed. At the beginning, the jet penetrates towards the top of the autoclave and reaches it at $t_t^* = -0.22$ (compare Figure 25). After reaching the top, the flow separates there and changes the movement towards the bottom of the autoclave again due to the lack of space. This vortex flow pattern dominates over the first half of the compression phase (compare Figure 28 left). However, as the pressure increases, and the temperature with it too, temperature gradients become prominent.

These temperature gradients lead to density differences of the fluid resulting in downwards directed movements of colder and upwards directed movements of warmer fluid. As the inflowing fluid always has lower temperatures than the surrounding fluid, whose temperature increases as long as the thermal expansion coefficient remains positive, the cold free jet is more and more influenced by the buoyancy forces. At $t_t^* = -0.1$, the buoyancy forces become prominent enough to prevent the free jet from reaching the top of the autoclave, and the jet penetration is reduced (compare Figure 25).

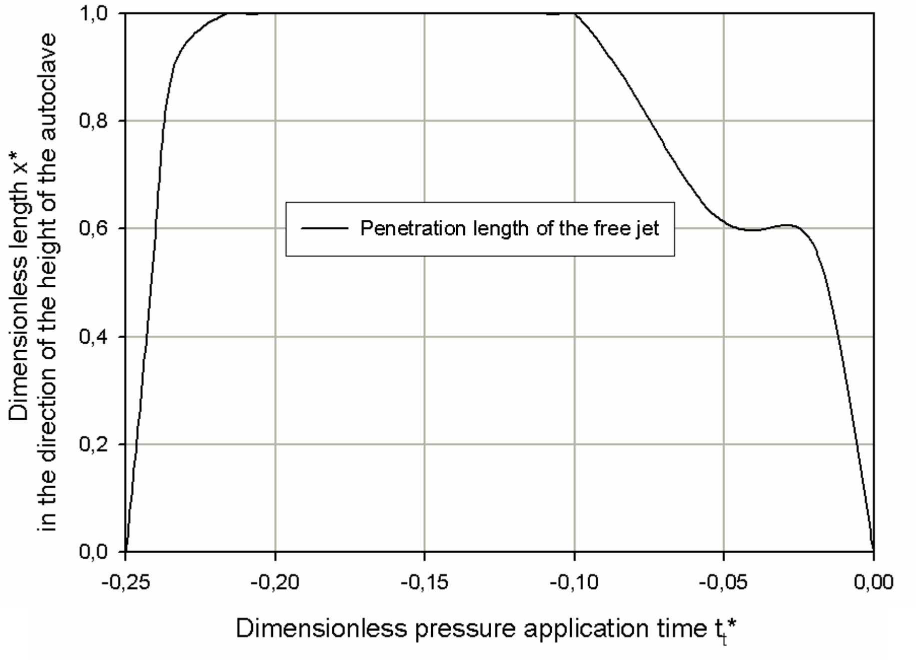

Figure 25 : The jet penetration in the high pressure autoclave in transient due to its interaction with the free convection caused by the density difference (due to the temperature gradient) of the fluid ($Re_d = 2279$).

The interaction between the free jet and the free convection can also be explained with Figure 26, where the overall kinetic energy inside the autoclave is shown. During compression ($t_t^* < 0$) the maximum of the kinetic energy of the flow is not at the end of the compression but at approx. $t_t^* = -0.1$. This is due to the downwards directed free convection caused by the density difference of the cold inflow fluid and the warm fluid residing in the autoclave, which locally act in the opposite direction to the free jet leading to smaller velocities in such regions. Due to smaller velocities the overall kinetic energy decreases too.

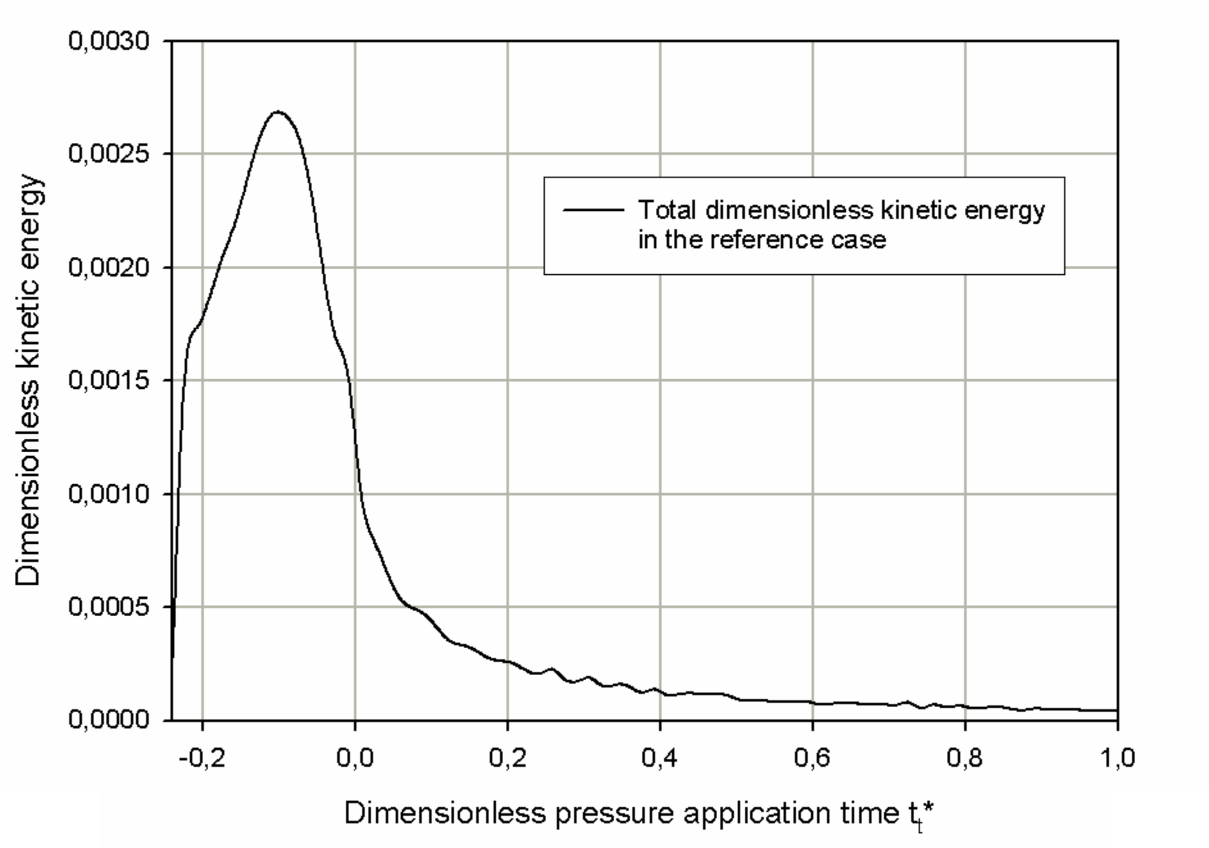

Figure 26 : Dimensionless kinetic energy during the pressure treatment.

To explain this in detail, in the second half of the compression phase the interactions between the free jet and the buoyant flow lead to the generation of several local vortices (compare Figure 27 and Figure 28). In the middle of the compression phase, as shown in Figure 28 (middle), two vortices of larger scales are visible: one in the lower part rotating clockwise and another one in the lower part of the autoclave rotating anti-clockwise. This happens due to the upward movement of the free jet and the buoyancy forces acting in the opposite direction.

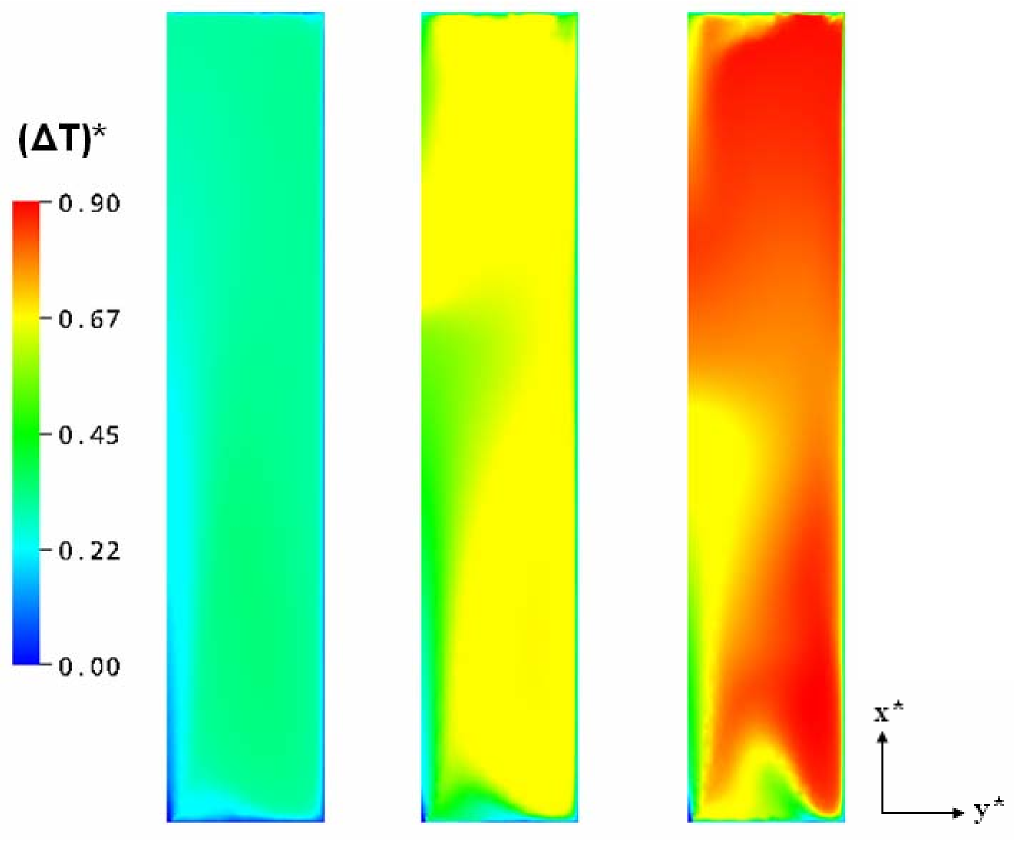

Figure 27 : Temperature distributions during the compression at $t_t^* =$ -0.233 , t_t^* = -0.125 and t_t^* = -0.017 from left to right respectively (Re_d = 2279).

However, towards the end of the compression phase, more vortices can be observed as the buoyancy effects (with a maximum temperature increase of up to $(\Delta T)^* = 0.9$) seem to gain the upper hand over the effects of the free jet (compare Figure 28 right), whereas the free jet and the fluid in regions next to the wall are significantly colder (with $(\Delta T)^* = 0.4 - 0.5$). Therefore, in the lower part, the interactions between the free jet and the buoyancy forces especially at the vertical wall and in the free jet region itself result in smaller vortices. In the upper part, two vortices can be observed, both being generated by the fluid being cooled down by the upper wall. These two vortices also rotate in opposite directions.

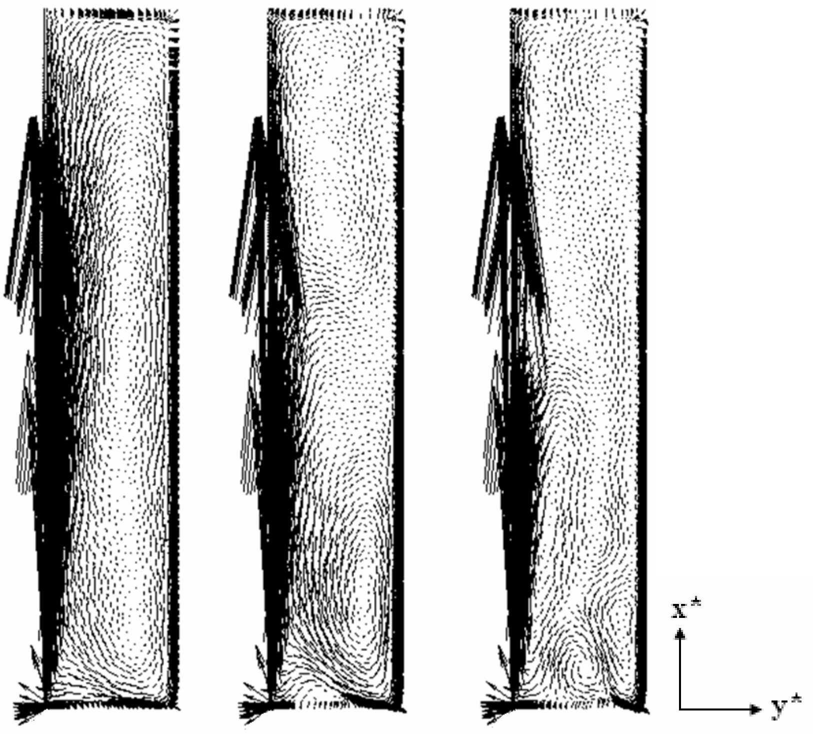

Figure 28 : Temperature distribution and velocity vectorial fields during the compression at $t_t^* = -0.233$, $t_t^* = -0.125$ and $t_t^* = -0.017$ from left to right respectively ($Re_d = 2279$).

To explain the flow behavior, it is useful to consider some dimensionless numbers. Firstly, although the critical Reynolds number, at which the flow becomes turbulent under high pressure is still unknown, there have been reports, where first instabilities of the free jet could be found at Re ~ 30 [109]. Here, the characteristics of the free jet is explained in chapter 2.5 thoroughly. However, it has been reported that the compressibility of the fluid might stabilize the free jet [108]. Therefore, further experimental and numerical studies on the stability of the free jet must be carried out here.

When heat transfer takes place, there is also a thermal wall layer which is affected by the thermal conductivity λ of the fluid. The ratio of the thickness between the viscous and thermal wall layers depends on the Prandtl number, which is a pure fluid property. For $Pr = 0(1)$, the thicknesses of both layers are of the same order of magnitude. If $Pr >> 1$, the thermal wall layer is then much smaller than the viscous wall layer. In this case, the Prandtl number of $Pr = 4.33$ can be calculated. Therefore, it can be concluded that the thickness of the thermal wall layer has the same order of magnitude as that of the viscous wall layer. The approximation of the temperature distribution of the fluid with analytical methods based on the Reynolds and Prandtl number can also be found in various works, i.e. [88].

Another important dimensionless number is the Eckert number, which represents the effects of the dissipation in the flow due to friction. Since it grows in proportion to the square of the velocity, it can be neglected for small velocities, i.e. velocity gradients. This can be confirmed with the calculated Eckert number of $\mathrm{Ec} = 1.9 \times 10^{-7}$. Therefore, it can be assumed that the temperature increase due to the dissipation of the fluid is minimal and can then be neglected.

In the cases, where both the kinetic and the potential energy play important roles, another dimensionless number called the Froude number, which is the ratio of inertial forces to gravity forces, is also considered. In this case, the Froude number of 0.08 shows that the gravity forces play an important role in this flow. Therefore, the flow pattern of the same case under compensated gravity would be different than the one shown. This shall then be studied in the next chapter.

The dimensionless group $\alpha_0 T_0$ is used to characterize the increase in enthalpy due to the compression work. This dimensionless group depends on the thermal expansion coefficient and the temperature of the fluid. In this case, $\alpha_0 T_0 = 0.112$ can be calculated. This indicates the importance of the thermal effects due to compression, which cannot be neglected. The larger this dimensionless group is, the higher the temperature increase of the fluid would be. For example, as for oils with higher thermal expansion coefficients, the temperature must increase higher than shown here with water. That would lead to larger heterogeneity of the temperature distribution also. Nevertheless, for the sake of completeness, all the considered dimensionless numbers and groups are listed in Table 10.

Table 10 : Characteristic dimensionless numbers and groups during the compression phase of the reference case.

$\mathrm{Re_d} = 2279$	$\mathrm{Pr} = 4.33$
$\mathrm{Ec} = 1.9 \times 10^{-7}$	$\mathrm{Fr} = 0.08$
$\alpha_0 T_0 = 0.112$	

Last but not least, the wall temperature must also be considered. On the one hand, in [49] Hartmann et al. introduced a finite difference solution to calculate the temperature of the wall. This finite difference program runs parallel to the main solver and feeds the solver code with the correct boundary conditions. The model used in this work is directly coupled with the main program and much easier to use while delivering the same results. As observed in [49] the temperature of the wall is also local and transient (compare Figure 29).

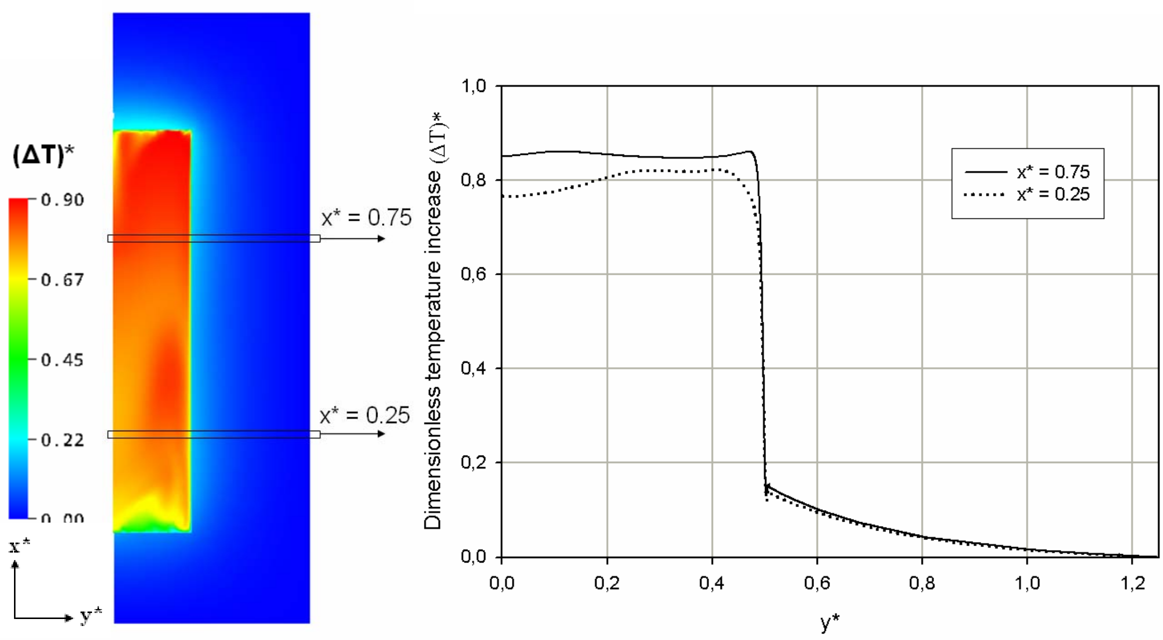

Figure 29 : Temperature increase in both the fluid (from y* = 0.0 to 5.0) and the solid (from y* = 5.0 to 1.25) at two different values of the height coordinate (x* = 0.25, 0.75) at the end of the compression phase (t_t^* = 0).

In detail, the temperature of the wall is always lower than the temperature of the fluid during the compression and the pressure holding phase, but still not constant. While the fluid has the temperature of $(\Delta T)^* \approx 0.8 - 0.9$, the temperature of the wall would amount up to only 0.08 – 0.17 at the highest. Generally speaking, it can be assumed that the temperature of the inner vertical wall is higher with increasing height. The hottest spot is the upper wall of the autoclave with $(\Delta T)^* = 0.22$, whereas the lowest temperature can be found in the lower corner with $(\Delta T)^* = 0.08$ (compare Figure 30). With increasing radius, the temperature of the wall decreases until it reaches the temperature T_0 or $(\Delta T)^* = 0$ of the tempering equipments at y* = 1.25.

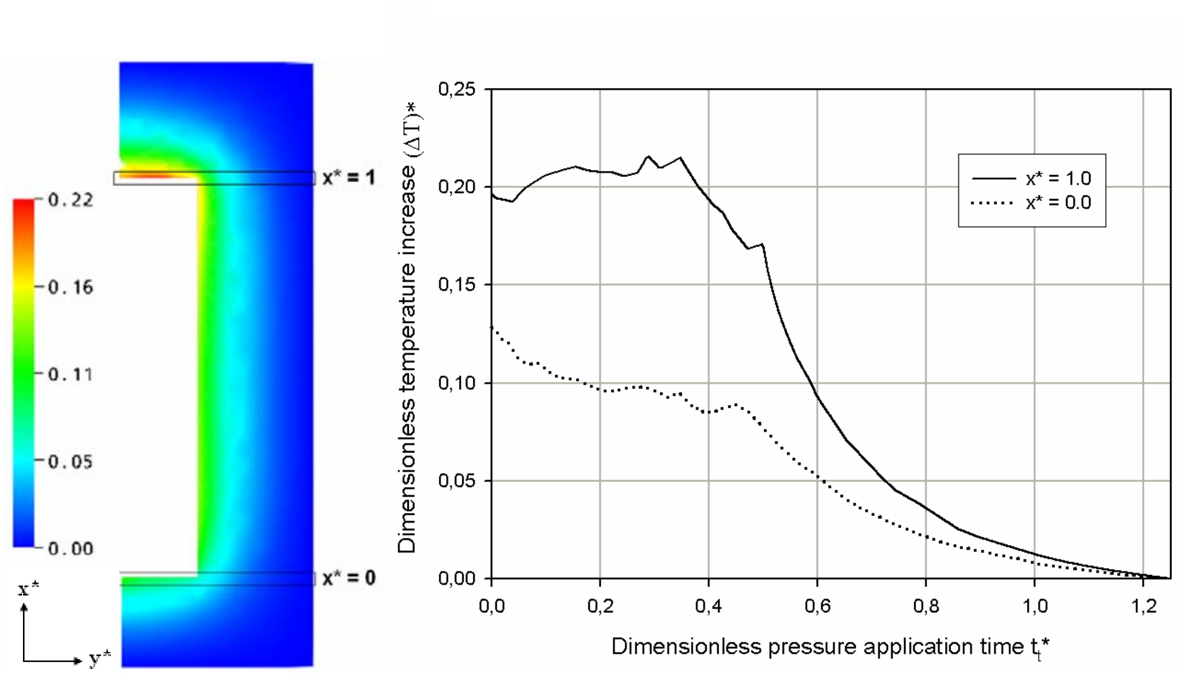

Figure 30 : Temperature increase of the wall at the bottom (x* = 0.0) and at the top of the inner chamber (x* = 1.0) at the end of the compression phase.

4.2.3.2 *Pressure holding phase*

During the pressure holding phase, where no additional pressure fluid enters the chamber, free convection dominates the flow pattern. As shown in Figure 31 and Figure 32, in the beginning of the pressure holding phase the flow pattern with larger vortices from the compression phase can still be seen. In detail, two larger vortices of opposite directions, one in the upper part and one in the inflow region in the lower part of the autoclave can be observed. Furthermore, the downward directed fluid movement at the wall regions can also be observed. The largest fluid velocities can be observed in both the vortices and the wall region. However, as the vortices decay and more heat is removed by the wall, only small vortices in the upper region can be observed. Due to reduced temperature gradient and, with it, smaller density differences, the velocities in both the vortices and the wall region are smaller than at the beginning of the holding phase.

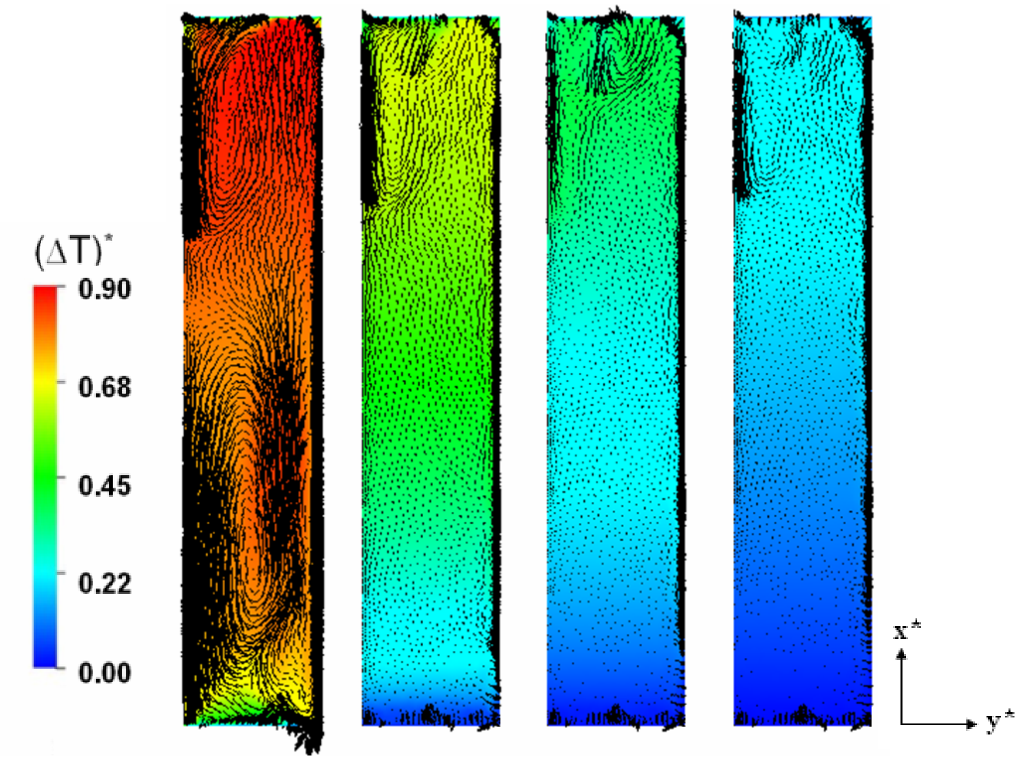

Figure 31: Temperature field at $t_t^* = 0.017$, $t_t^* = 0.33$, $t_t^* = 0.67$, and $t_t^* = 1$ (left to right) for process with $Re_d = 2279$

The Grashof number, which is used in characterizing free convection phenomena, is defined as the ratio between the buoyancy and the viscous forces (see also eq. 2.94). In this case, the Grashof number of $Gr = 3.33 \times 10^9$ can be calculated. In free convection, the Grashof number plays a similar role as the Reynolds number plays in forced convection. If the temperature gradient is totally parallel to the gravity vector, the critical Grashof number for a vertical flat plate, where the buoyancy forces overcome the viscous forces, is considered at approx. $Gr = 10^9$, where boundary layer could then be observed. However, as shown in Figure 31 the temperature gradient of the fluid is both in vertical and horizontal directions, so that free convection always occurs. Here, it is not yet adequately examined, if the flow at the vertical wall has boundary layer characteristics. Further numerical and experimental investigations can give more detailed information on this flow character.

Another dimensionless number, which is also considered in the natural convection, is the Rayleigh number, which is the product of the Prandtl and the Grashof numbers. It is the critical parameter in the theory of thermal instability for laboratory flow. In Figure 31, it can also be observed that the temperature gradient at the wall of the autoclave has its components in both vertical and horizontal direction. Therefore, free convection can always occur, as the temperature and also density gradient of the fluid is not totally parallel to the gravity vector (see also section 2.4.1.6), and the critical Rayleigh number of 0 is considered. Here, the Rayleigh number of $Ra = 1.44\times10^{10}$ can be calculated. For the sake of completeness, the numerical values of the considered characteristic numbers are shown in Table 11.

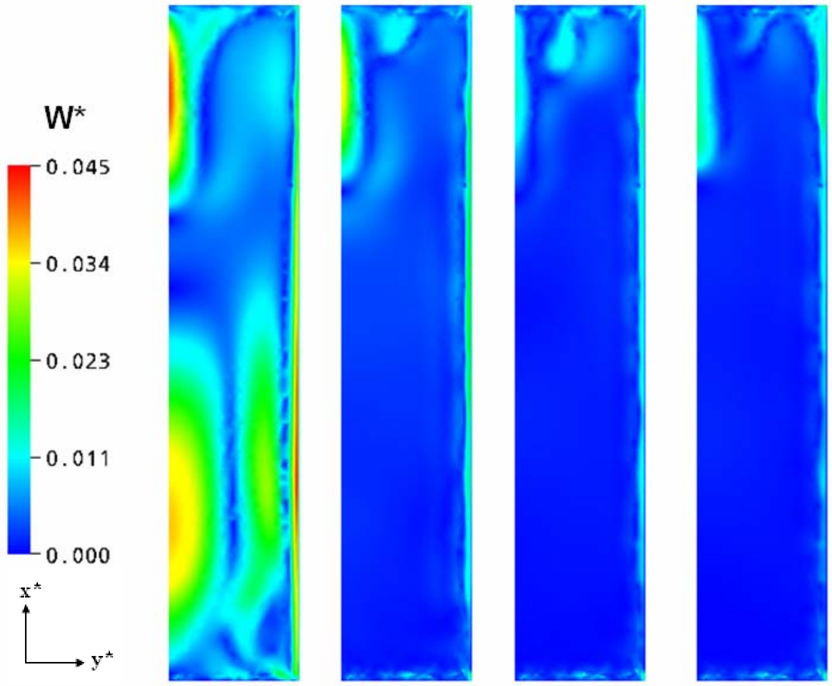

Figure 32 : Velocity field (lower) at $t_t^* = 0.017$, $t_t^* = 0.33$, $t_t^* = 0.67$, and $t_t^* = 1$ (left to right) for process with $Re_d = 2279$

Table 11 : Characteristic dimensionless numbers during the pressure holding phase of the reference case

$Gr = 3.33\times10^{9}$	$Ra = 1.44\times10^{10}$

4.2.4 Inactivation of enzyme Bacillus subtilis α-Amylase

The non-uniformity of the conversion process is substantially related to the thermofluiddynamical processes. Since most pressure induced biological conversion processes are also temperature dependent, the existence of gradients, especially of thermal gradients, during the whole high pressure process always leads to non-uniformity in the conversion process.

Generally, the risk of substantial heterogeneity is high if the time scale of hydrodynamic motion is small and the time scale of heat conduction is large compared to the time scale of the high pressure conversion process. This was discussed in detail by Hartmann and Delgado [46]. Therefore, it is essential to study the effects of the temperature gradients in the autoclave on the heterogeneity of the products in order to ensure the product safety.

As mentioned before, in this study the effect of thermally induced non-uniformity is investigated using a high pressure conversion model of Denys et al. [32]. This model describes the inactivation kinetics of an enzyme called *Bacillus subtilis* α-Amylase dissolved in a 0.01 M Tris-HCl buffer (pH 8.6) at a concentration of 15 g/l. The inactivation rate of this enzyme depends on both pressure and temperature, and its high pressure conversion time scale can be described as the reciprocal of its inactivation rate. It is assumed that the enzyme molecules are very small and dissolve completely and homogeneously in the solution. The diffusion coefficient of this enzyme is negligibly small, and therefore, will be assumed as zero. At the beginning of the high pressure treatment, it is assumed that the relative enzyme activity of the high pressure treatment is at 1 (100%) throughout the chamber. Additionally, the inflow stream is assumed to contain the same fluid with the same enzyme activity.

Firstly, a particle tracking simulation of dissolved enzyme molecules is carried out. Overall, 200 particles are tracked throughout the high pressure treatment. The information concerning the location, overall distance, pressure and temperature of the particles are obtained. In Figure 33, the particle tracks of 2 particles are shown on the left side. It becomes obvious that each dissolved enzyme molecule has a different path. Traveling through different regions, each molecule is opposed to different thermal conditions.

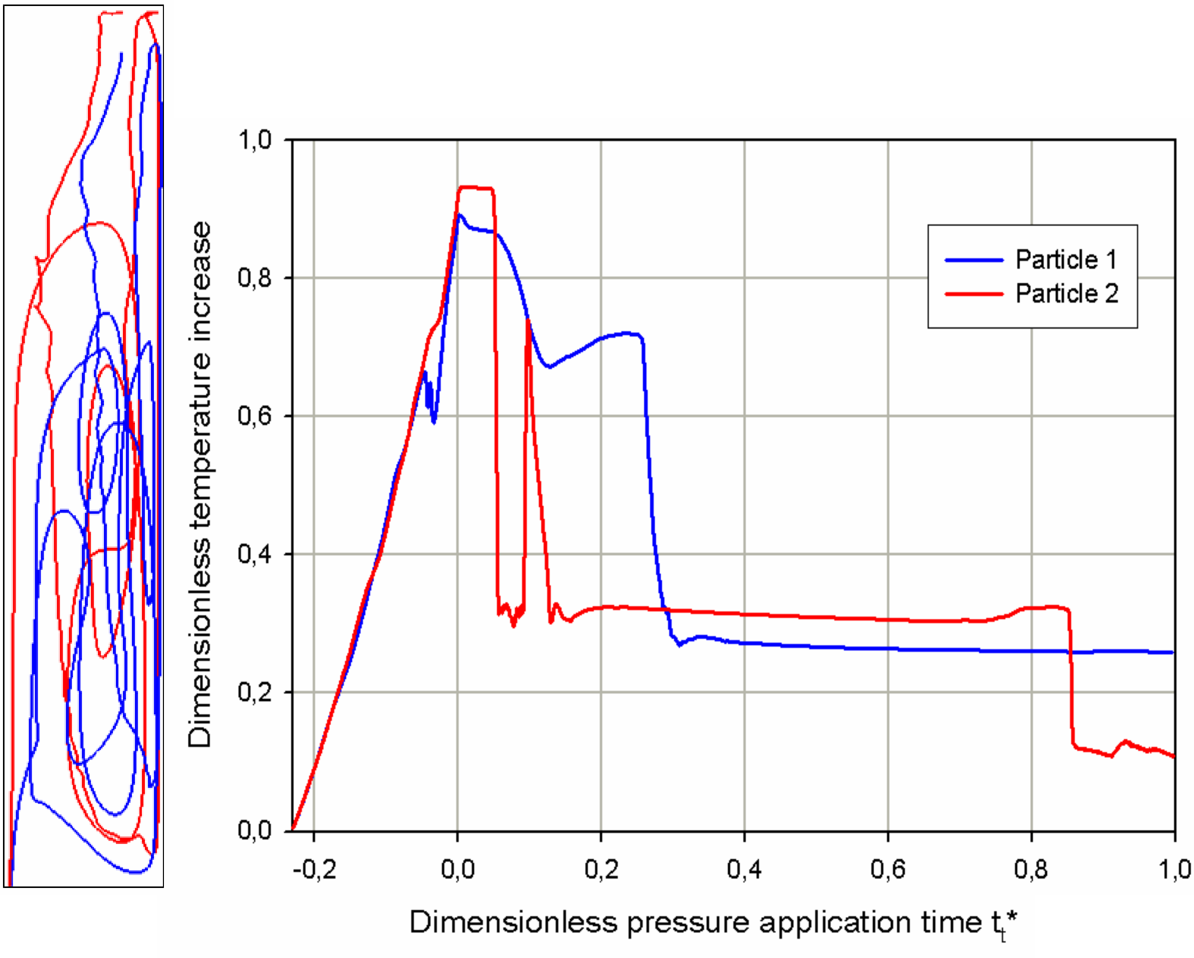

Figure 33 : Particle tracks of two enzyme molecules on the left. On the right side, the temperatures of the surrounding fluid of both molecules are displayed ($Re_d = 2279$).

Wandering through different regions with different temperatures, the enzyme molecules are opposed to different inactivation intensities. In Figure 34 it is shown that the two tracked molecules travel through different regions with different pressures, temperatures and, therefore, different inactivation rates. Therefore, it becomes obvious that the inactivation process of the enzyme BSA is inhomogeneous. This can also be implied to other temperature-dependent inactivation processes. To ensure the product quality, it is important to study not only the heterogeneity of the temperature distribution but also the mass conversion process coupled to it. In this case, it is assumed that the enzyme molecules dissolve completely in the solution. Therefore, the residual enzyme activity is subject of convective and diffusive transport. In this sense, Computational Fluid Dynamics proves itself as a sufficient tool predicting the heterogeneity of such mass conversion processes.

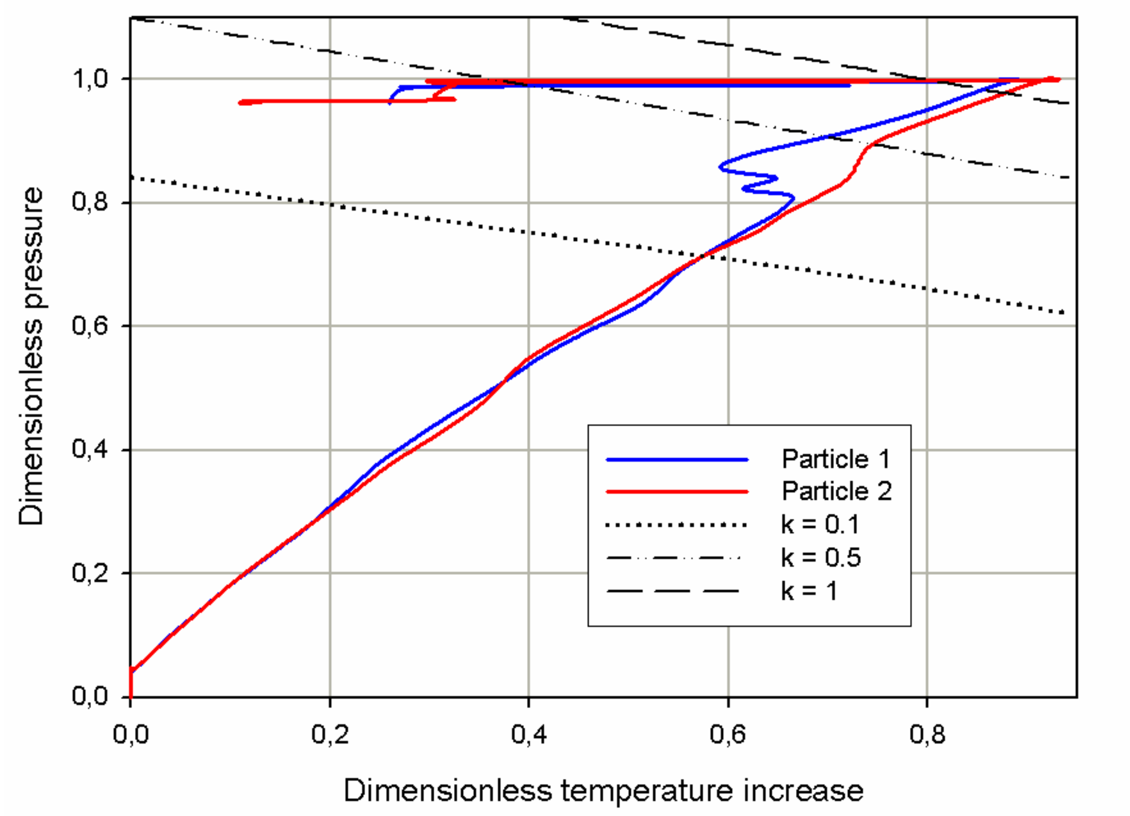

Figure 34 : Pressure-Temperature pair of the fluid surrounding the tracked molecules shown in Figure 33. The black lines shown represent the border lines for given inactivation rates of the enzyme BSA.

Considering the enzyme activity as a transport variable, the equation for the inactivation of the enzyme *Bacillus subtilis* α-Amylase can be solved within the solver as an additional transport equation. Figure 35 shows the distribution of the residual enzyme activity after a high pressure treatment at p* = 1 and $t_t^* = 1$. On the left the reference case with the standard configuration is shown. On the right side the configuration of the reference case is altered. In this “adiabatic” case no heat transfer between the wall and the fluid is considered. As no heat is removed by the wall, the overall temperature is higher in this case. In other words, the adiabatic temperature increase of $(\Delta T)^* = 1.0$ can be reached in most parts of the autoclave with an exception in the inlet region.

The adiabatic case is inspired by the work of De Heij et al. [40], who installed heat damping at the inner wall of the autoclave in order to maximize the performance of the high pressure autoclave by reducing the heat transfer between the fluid and the colder steel wall. This results in relatively homogeneous temperature and residual enzyme activity distributions.

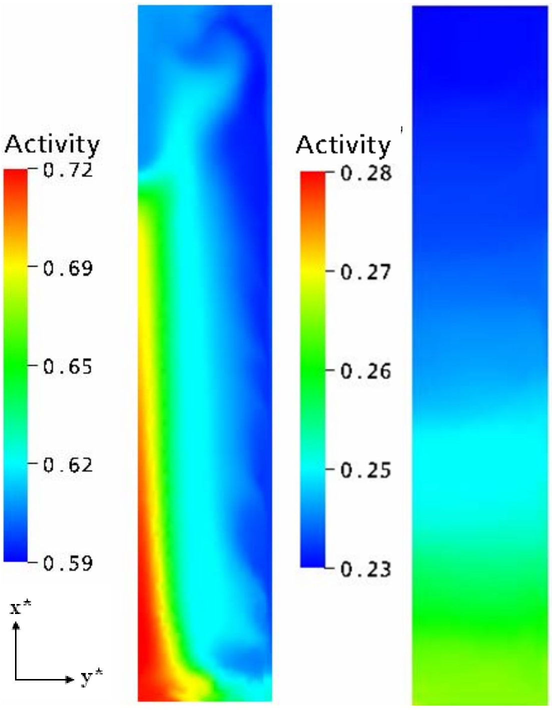

Figure 35 : Distribution of the residual enzyme activity in reference case (left) and adiabatic case (right) at $t_t^* = 1$.

Considering the reference case, it can be concluded that more enzymes can be inactivated in the upper region and the near wall region. On the contrary, highest residual enzyme activities can be found in the region near the inlet, where the cold water jet used to be. In this sense, it becomes obvious how a heterogeneous temperature distribution affects the uniformity of the product quality. The range of the residual enzyme activity of 0.59 to 0.72 is considerably large if compared to the adiabatic case on the right, where the residual activity of 0.23 – 0.28, which is much smaller, can be observed.

Moreover, the pattern of the residual activity distribution in the adiabatic case is different from that of the reference case. This is because the flow pattern in this case differs so much from that of the reference case (see section 4.2.3). Since the cooling process at the wall is missing, no prominent downward directed movement of the fluid at the wall due to free convection can be observed. And as no heat is removed by the wall due to the adiabatic condition, no significant temperature gradient can be observed. Only the cold inflow fluid remains one last reason for the thermal heterogeneity inside the autoclave, the inactivation process of the adiabatic case is much more homogeneous and effective than that in the reference case. This can also be shown in Figure 36 and Figure 37, where the averaged enzyme activity and the standard deviation of the residual activity of the enzyme BSA during a high pressure treatment at p* = 1 and t_t^* = 1 are shown. Whereas only 40% of the enzyme molecules can be inactivated after the treatment, the adiabatic condition can enable further reduction of enzyme activity of up to 75% during the same period of time. As no heat is removed by the wall in the adiabatic case, the temperature in this case is higher. Therefore, more enzyme molecules can be inactivated. If the same result is desired, the adiabatic condition can reduce the process duration by up to 60 %.

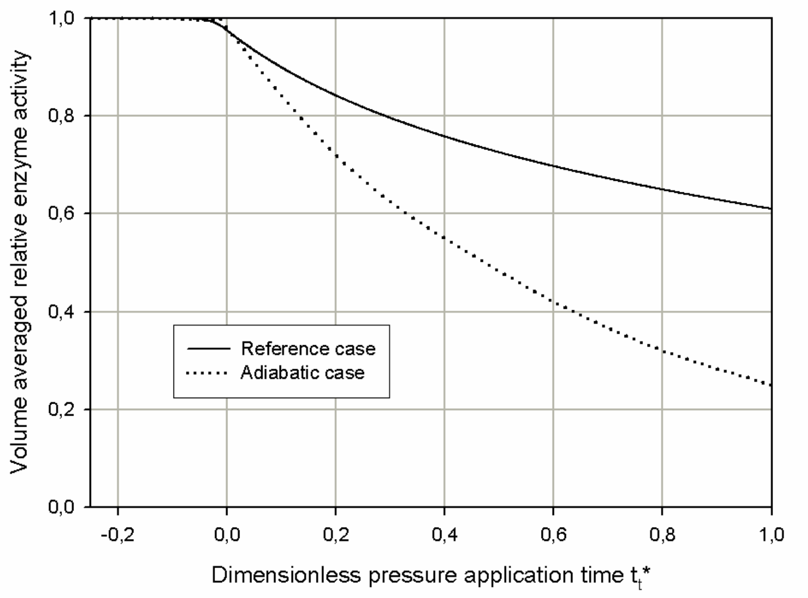

Figure 36 : Volume averaged residual enzyme activity of BSA during the high pressure treatment at p* = 1 and t_t^* = 1. Solid line represents the reference configuration, and the dotted line the adiabatic case.

Another advantage of the adiabatic condition can be shown in Figure 37, where the spatial standard deviation of this enzyme during the pressure treatment under the same condition is shown. The standard deviation of this enzyme is a tool to measure the heterogeneity of the product quality. Here, it can be observed that the adiabatic condition leads to less heterogeneity of the product quality, where the maximum of the standard deviation amounts up to approx. 1% only, compared to 2.3% in the reference case. This is due to the missing heat removal by the wall, so that the temperature gradient is not prominent in this case. The reason for the small yet visible non-uniformity in this case is the colder inflowing fluid, which can't mix with the warmer fluid inside the autoclave quickly. However, in real high pressure applications, the inflowing fluid might have higher temperatures than assumed in this work. How high the temperature is depends on many factors, i.e. if the inflowing fluid is tempered or if the piping is also insulated. If the pipes are also insulated, then it can be assumed that this small heterogeneity shown here will also disappear. Only then, total homogeneity of the temperature distribution and the product quality can be achieved.

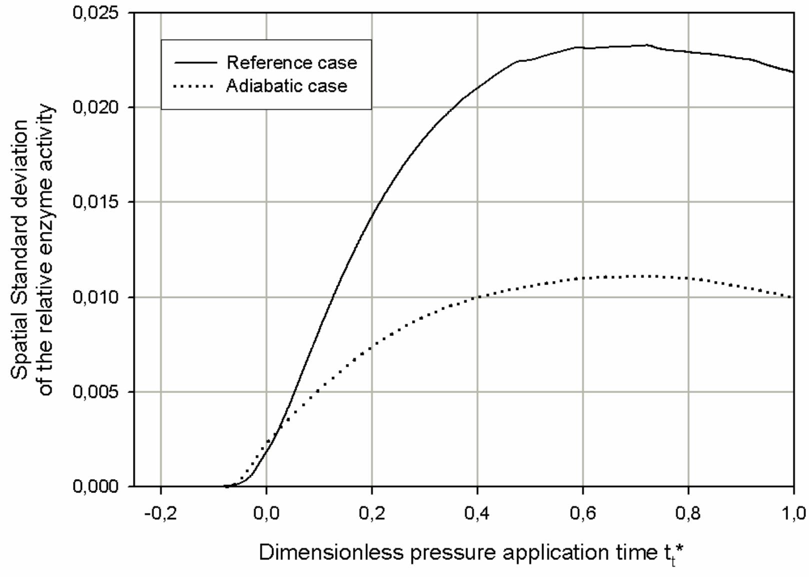

Figure 37 : Standard deviation of the residual enzyme activity of BSA during the high pressure treatment at p* = 1 and t_t^* = 1. Solid line represents the reference configuration, and the dotted line the adiabatic case. The spatial standard deviation is calculated by taken into consideration the difference between the enzyme activity at each point of the high pressure chamber and its spatial mean value.

Therefore, attempts to create such adiabatic conditions should be made to improve the effectiveness and the uniformity of the product quality. This can be made with, e.g., installation of an extra layer made of polymer such as POM or PEEK, which temperature increase during the high pressure treatment is higher than water. Moreover, it is also possible to use small polymer particles as hot spots. Such hot spots should be put directly into the treated fluid substances and should heat up the fluid during the high pressure treatment, thus the name “hot spots”, so that the adiabatic temperature can be reached throughout the high pressure autoclave. This possibility is being studied at our chair and represents an extremely interesing research field.

However, considering the standard deviation to be as low as 0.01 – 0.023 the inactivation process of the enzyme in this case can be considered homogeneous. This is due to the convection process taking place throughout the entire high pressure treatment. This becomes obvious by comparing the numerical groups of the inactivation equation (section 2.7.3) as shown in Table 12. The estimations are based on the following parameters: $D_{A0} = 0$, $W_0 = 0.01$ m/s, $L_0 = 0.31$ m, $k_0 = 0.04$.

Table 12: Orders of magnitudes of the dimensionless groups of the inactivation equation of *Bacillus subtilis* α-Amylase under high pressure.

Term	Importance	Order of magnitude
$\frac{\partial A^*}{\partial t^*}$	Local change of the relative enzyme activity	1
$\frac{\partial A^* W_x^*}{\partial x^*} + \frac{\partial A^* W_y^*}{\partial y^*}$	Convective transport	1
$\frac{D_{A0}}{W_0}\left[\frac{\partial}{\partial x^*}\left(D_A^*\frac{\partial A^*}{\partial x^*}\right) + \frac{L_0}{D}\frac{\partial}{\partial x^*}\left(D_A^*\frac{\partial A^*}{\partial y^*}\right)\right]$	Diffusive transport	0
$-\frac{L_0}{W_0}k_0 k^* A^*$	Source term	1

It is obvious that the source term and the convection term are of equal importance. Due to the small diffusion coefficient of this enzyme, it can be assumed that the diffusive term is zero. With such prominent convective transport, which term has the same order of magnitude as the other important terms, it is apparent that the convective transport of this enzyme contributes to increased uniformity of the inactivation process. However, if the convective transport is reduced, increased uniformity of the inactivation process of enzymes is expected.

An evidence for this statement above can be found in one of the author's previous publication, where three simulations for the direct inactivation of the same enzyme are carried out: one with water as pressure fluid, another with viscous oil ($\eta_{oil} = 100 \times \eta_{water}$) and an isentropic case with water (Figure 38).

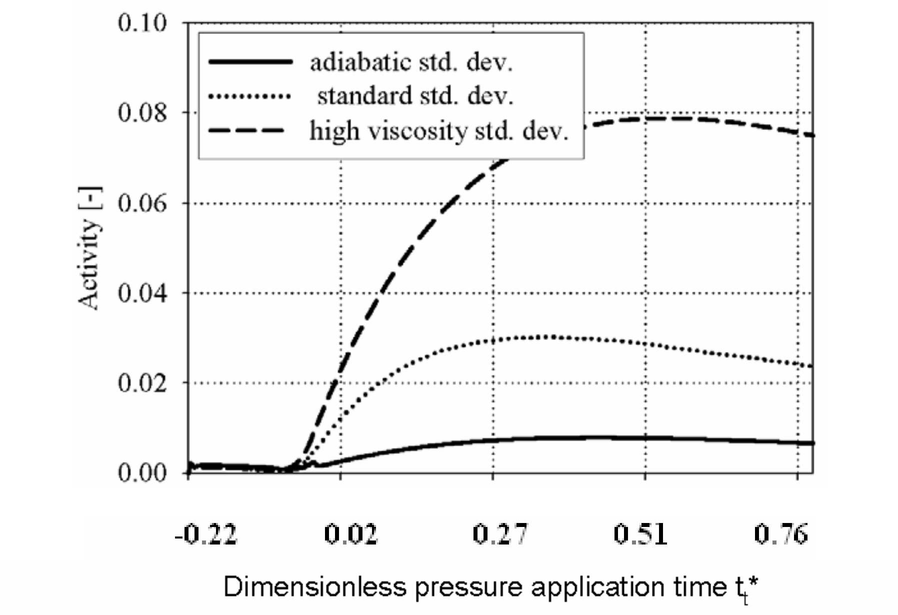

Figure 38 : Volume weighted standard deviation [49].

The standard deviation of the residual relative activity is the lowest in the adiabatic case. The largest standard deviation of 0.08 can be found in the case of highly viscous oil. This is approx. 3 times larger than that in the standard case and 8 times larger than that of the adiabatic case. Furthermore, the standard deviation of the high viscosity case reaches its maximum considerably later than the other cases (after 600 seconds). These are due to the reduced convective transport with the hydrodynamic compensation time scale being hundred times smaller than the standard case with water. Thus, it can be concluded that the convective transport is very important for the uniformity of the direct inactivation on enzymes or similar dissolved substances under high pressure.

Therefore, in indirect high pressure processes, where food is treated in packages, the package will act as an additional barrier for the fluid motion, so that the convective transport is reduced. As a result of this, the high pressure treatment of packed food at different locations on the autoclave may lead to strong heterogeneity of the product quality among all the packages. Thus, it can be concluded that the direct high pressure treatment of food is better than the indirect one, if the homogeneity of the treated substances is concerned.

4.2.5 Effects of buoyancy (compensated gravity case)

As mentioned in the previous chapter, free convection, which is driven by density differences due to temperature gradients, dominates the flow pattern during the pressure holding phase. The local changes in the density of the fluid result in buoyancy forces that cause currents in the fluid. In compensated gravity, however, buoyancy no longer becomes a factor. Therefore, no free convection occurs under compensated gravity. To examine the effects of free convection it is useful to compare the reference case with those under compensated gravity. To this end, a numerical simulation of a high pressure treatment of the same enzyme solution as in the reference case is repeated under compensated gravity conditions (Figure 39).

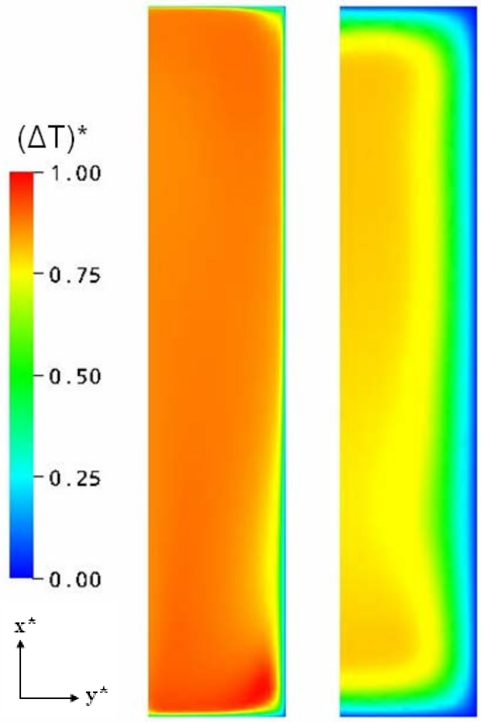

Figure 39 : Temperature distribution at the end of the compression phase ($t_t^* = 0$) on the left side and the pressure holding phase ($t_t^* = 1$) on the right side ($\mathrm{Re_d} = 2279$).

Firstly, it can be observed that the flow pattern is totally different from that of the reference case. First of all, due to missing free convection, the flow pattern during the compression phase is dominated by the flow resulting from the free inflow jet alone. The temperature in the lower-corner region can reach the adiabatic temperature, because the big vortex resulting from the cold inflow jet cannot reach this part due to the geometry. However, as heat is removed from the fluid by the wall but no free convection occurs, the fluid in the near wall region is cooled down, whereas the fluid in the middle of the autoclave stays warm. As no free convection occurs, almost no fluid motion can be observed during the holding phase. Therefore, almost no mixing of the cold with the warm fluid can happen, and, hence, the temperature gradient becomes prominent. In detail, at the end of the pressure holding phase ($t_t^* = 1$) the temperature range of $(\Delta T)^* = 0 - 0.75$ inside the fluid is extremely wide compare to 0 – 0.2 in the reference case (compare Figure 31). Furthermore, the characteristic dimensionless numbers and groups (Re_d, Pr and Ec) for this case are the same as those of the reference case shown in Table 10, only that the Froude, Grashof and Rayleigh numbers tend to zero, as no gravitational force exists and no free convection occurs. Therefore, the differences seen in this case to the reference case are due to the lack of the gravitation solely.

The lack of buoyancy forces also leads to different behaviour in the inactivation process of the enzyme solution. Firstly, as less mixing between the cold fluid in the wall region and the warm fluid in the middle can take place, heat can be removed only from the fluid in the near wall region, whereas the heat can be removed from the fluid in the middle only through direct conduction. Overall, less heat can then be removed from the fluid. Therefore, the averaged temperature increase in the compensated gravity case is always higher than that of the reference case (see Figure 40).

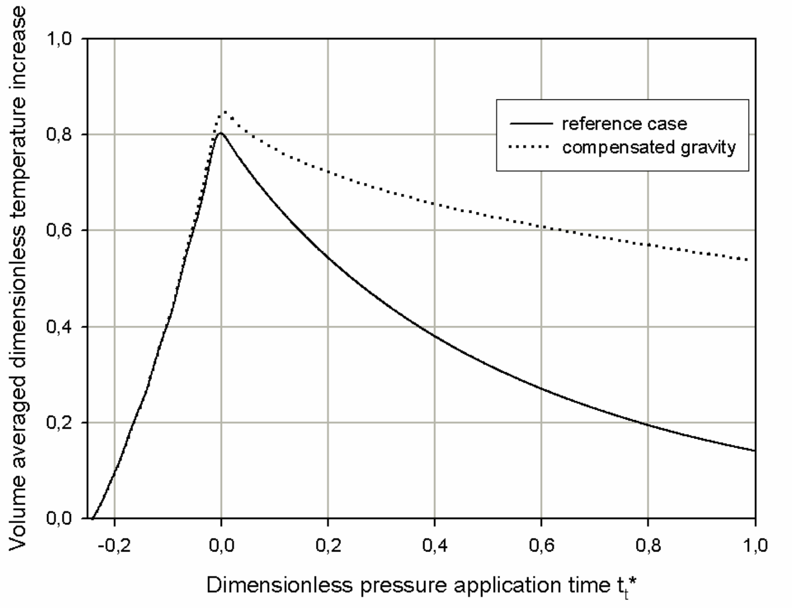

Figure 40 : Volume averaged temperature increase: solid line represents the reference case, whereas the dotted line represents the compensated gravity case ($Re_d = 2279$).

The differences in the temperature distributions of the two discussed cases also lead to different behaviours in the characteristics of the mass conversion process. As can be seen in Figure 41, the lack of the buoyancy forces results in a different pattern of the inactivation process of the enzyme BSA. Firstly, the range of the residual enzyme activity is much wider in the compensated gravity case (0.38 – 0.72) compared to that of the reference case (0.59 – 0.72). Furthermore, in the compensated gravity case more inactivation can be observed in the middle part of the autoclave. This represents just the opposite of what can be seen in the reference case, where more inactivation can be seen in the wall region and the inlet region has the highest residual enzyme activity due to the remaining influences of the inflow jet. This can be explained with a different temperature distribution and the lack of the convective mass transport in the compensated gravity case.

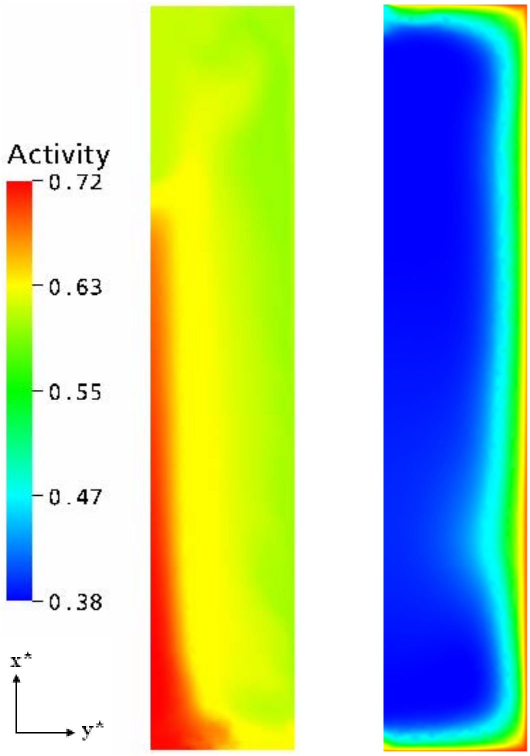

Figure 41 : Distribution of the residual enzyme activity of BSA. On the left: reference case. On the right: compensated gravity case ($Re_d = 2279$).

However, the compensated gravity case appears to be the more effective one, as the volume averaged residual activity at $t_t^* = 0$ is at 0.46 compared to approx. 0.6 in the reference case (compare Figure 42). This is due to the overall higher temperature as can be seen in Figure 40. Considering the heterogeneity of the product quality, however, the lack of buoyancy forces causes increased non-uniformity of the product. The first reason is the stronger temperature gradient in this case. The second reason is the lack of the convective mass transport, so that no mixing of the damaged and undamaged enzyme molecules can take place. Therefore, even at $t_t^* = 1$ the standard deviation of almost 9 % is much higher than the 2 % of the reference case, even that the maximum standard deviation of this case is not reached after this lengthy high pressure treatment.

Therefore, it can be concluded that the lack of buoyancy forces has positive influences on the effectiveness of the mass conversion process. However, the strong heterogeneity of the overall product quality is a great concern. If the high pressure treatment is going to be used in such extreme conditions, i. e. in space stations, there must be some attempts made in order to decrease the thermal heterogeneity. A good example is the heat damping as mentioned in the last chapter in order to reduce the heat removal by the wall. Only then can the uniformity of the high pressure treated products under such conditions be guarantied.

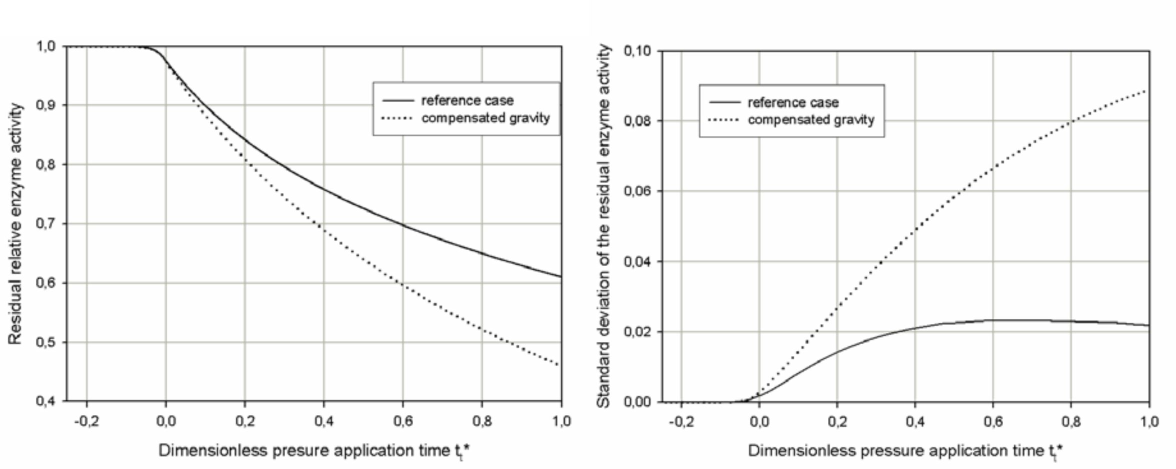

Figure 42 : Averaged residual activity (left) and standard deviation (right) during a high pressure treatment of p* = 1 and t_t^* = 1 of the reference case (solid line) and the compensated gravity case (dotted line) with linear pressure ramp at $Re_d = 2279$.

4.2.6 Effects of different length scales

Most of the experiments in the field of the high pressure treatment of biotechnological substances are carried out in small laboratory-scale autoclaves. However, thermofluiddynamical processes in lab-scale high pressure applications differ from those in industrial high pressure applications drastically. Especially, the effectiveness of the tempering devices differs due to different surface area to volume ratio as can be seen in Table 13. Due to smaller surface area to volume ratio in larger high pressure autoclaves, tempering devices will not function as optimally as in lab-scale autoclaves. In other words, at approximately the same heat flux less heat can then be removed from the same volume unit. Therefore, although tempering devices may be sufficient to control the temperature in lab-scale autoclaves, it is much harder to control the temperature inside larger autoclaves. Due to the differences in the temperature profile inside autoclaves of different sizes direct knowledge transfer from lab-scale autoclaves to industrial high pressure applications is problematic.

Table 13 : Surface area to volume ratio (m^{-1}) of the 3 investigated autoclave configurations.

		3.3 ml volume	3.3 l volume	3300 l volume
Surface area to volume ratio	$\frac{2\cdot(D+2L_0)}{D\cdot L_0}$	731.2	73.12	7.312

Therefore, it is essential to study the scale-up and scale-down effects in the high pressure application. Firstly, a concept to approximate the thermal heterogeneity is introduced. This model is based on the simplification of the regions inside of the autoclave into two regions with extreme thermal conditions: the near wall region with maximum cooling effects and the middle region with maximum effects due thermal expansion (Figure 43).

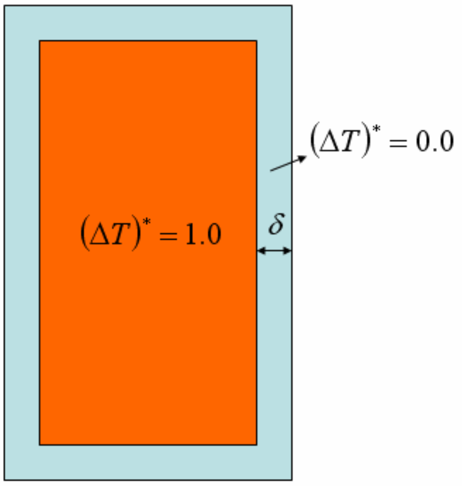

Figure 43 : The two volume model to approximate the effects of the temperature gradient.

The size of the near wall region is defined through the thickness of the thermal wall layer δ, which has the same order of magnitude as the viscous wall layer at Pr ≈ 1 (Pr = 4.3 in this case). The thickness of the thermal wall layer can then be calculated as:

$$\delta = \frac{3.464\cdot L_0}{\sqrt{\mathrm{Re}}} = 3.464\cdot\sqrt{\frac{\eta\cdot L_0}{\rho\cdot W}}\,. \tag{4.2}$$

With the given parameters, an approximated thickness of the thermal layer of $\delta / L_0 = 0.04$ (approx. 1.3 cm for water properties at 313 K and L_0 = 0.31 m) can be calculated. Defining the temperature increase $(\Delta T)^*$ of the fluid near to the wall at 0.0 and that of the middle region to be 1.0 as shown in Figure 43, the standard deviation of the temperature increase is then calculated for different autoclaves with different sizes. It can be seen that the highest standard deviation of the temperature can be found in middle size autoclaves around $V/V_{ref} = 1.0$, where V_{ref} denotes the volume of the autoclave in Nantes (Figure 44). In lab scale autoclaves, the cooling devices can act optimally and cool down the fluid inside the autoclave efficiently. In very large autoclaves, on the contrary, the thermal expansion dominates over the cooling process and the adiabatic temperature can be found throughout the autoclave, so that the standard deviation becomes smaller. Therefore, it can be concluded that the risks of non-uniform thermal treatments of high pressure products must be the largest in middle-sized autoclaves, which will be used in real industrial applications.

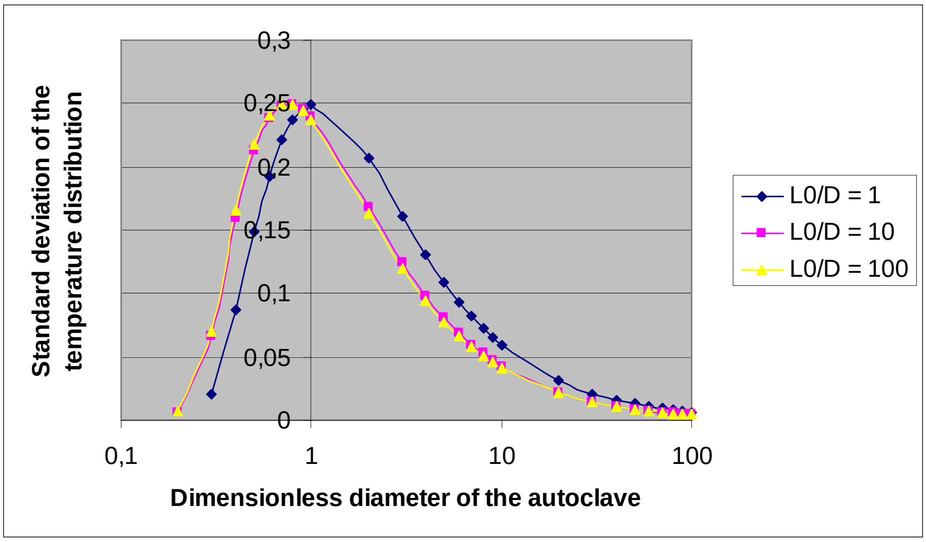

Figure 44 : Standard deviation of the dimensionless temperature increase in autoclaves of different sizes. The calculation shows that difference of the geometry of the autoclave has influences on the homogeneity of the inactivation process.

This is confirmed with by expanding the proposed simplified model by calculating the Damköhler number (DaI), which is a characteristic number used to relate the chemical reaction timescale to other phenomena occurring in a system. For a general chemical reaction of n-th order, the Damköhler number can be defined as:

$$DaI = k \cdot C_0^{n-1} \cdot t \, , \tag{4.3}$$

with k as the kinetics reaction rate constant, C_0 as the original concentration and t as the characteristic time scale. As the inactivation kinetics of the enzyme BSA used in this work is a first order one, the Damköhler number (DaI) can then be calculated as:

$$DaI = k \cdot t. \tag{4.4}$$

For a high pressure treatment of $t_t^* = 1$ (10 minutes) at p* = 1 (500 MPa), the standard deviation of the calculated Dammköhler number is then considered. Also here, it can be concluded that the highest heterogeneity of the product can be found in middle-sized autoclaves around $V/V_{ref} = 1$, where neither the thermal expansion effects nor the cooling processes at the wall regions dominate in the autoclave (Figure 45).

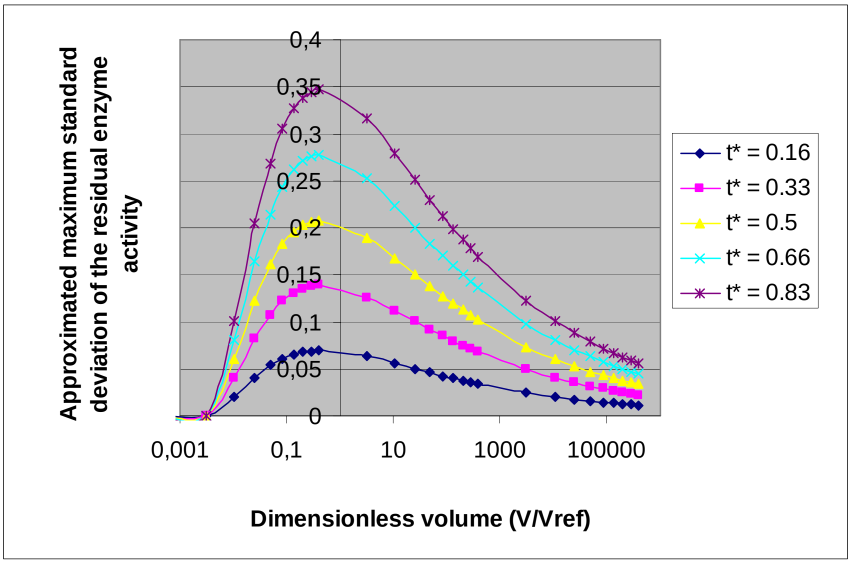

Figure 45 : Approximated maximum standard deviation of the residual enzyme activation after a pressure treatment at p* = 1 (500 MPa) and t* = 1 (10 minutes).

Therefore, it can be concluded that scaling up the experiments does not always lead to increased non-uniformity, and scaling down does not always correlate with less heterogeneity of the product. Homogeneous high pressure treatments can be achieved only in very small or very large autoclaves, but in middle-sized autoclaves, non-uniformity of the product must be considered. However, it must be kept in mind that this model does not include the effects of free convection, which contribute to better homogeneity of the system greatly. Therefore, this model can be used to approximate the effects of the temperature gradient, but is not capable of giving qualitative information in real high pressure treatments. Therefore, further numerical simulations must be carried out.

Numerical simulations in autoclaves of different size show similar results as can be seen in Figure 46. Firstly, it can be concluded that larger autoclaves are more effective as more enzymes could be inactivated due to worse cooling process and, thus, higher temperatures (compare Figure 47). Considering the homogeneity of the product, however, it can be concluded that the highest non-uniformity of the product quality is awaited in middle-scale autoclaves. In lab-scale autoclaves, the tempering devices can function optimally, and in large-scale autoclaves thermal expansion dominates. In middle-scale autoclaves, however, these two phenomena act against each other and none of them can dominate the flow pattern. Therefore, temperature gradients and non-uniformity of the product quality must be considered seriously in such middle scale-autoclaves.

Here, it should be stated that the simulation for the 3300 l autoclave, representing the amplification of the length scale of the geometry of the reference case by factor 10, was carried out with the same mesh used for the reference case but just 10 times larger in the length scale without further modifications. Therefore, there is a concern that the mesh density used in this case may not be sufficient to ensure the accuracy of the results. Thus, simulations for autoclaves with 26.4 and 412.5 l, representing the amplification of the length scale by factor 2 and 5 respectively, were carried out. They also confirmed the trend that more inactivation and less heterogeneity are awaited as the size of the autoclaves increase (Figure 46).

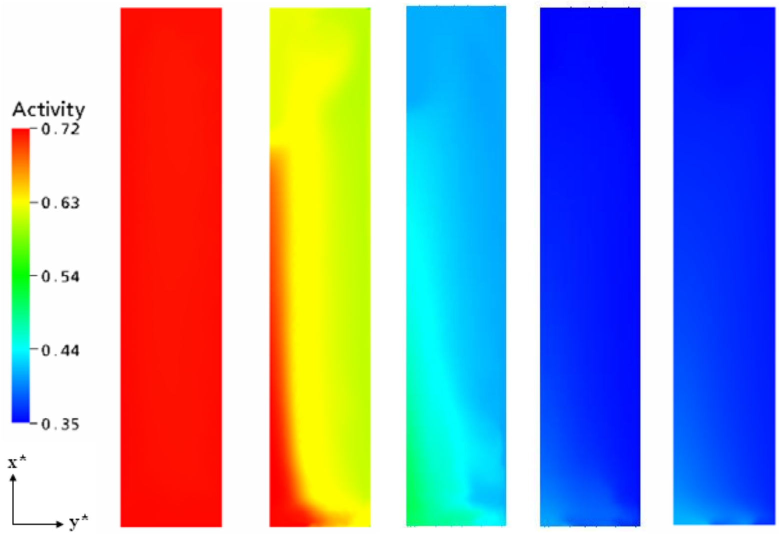

Figure 46 : Distribution of the residual activity of enzyme BSA in 3.3 ml, 3.3 l, 26.4 l, 412.5 l and 3300 l autoclave (from left to right respectively).

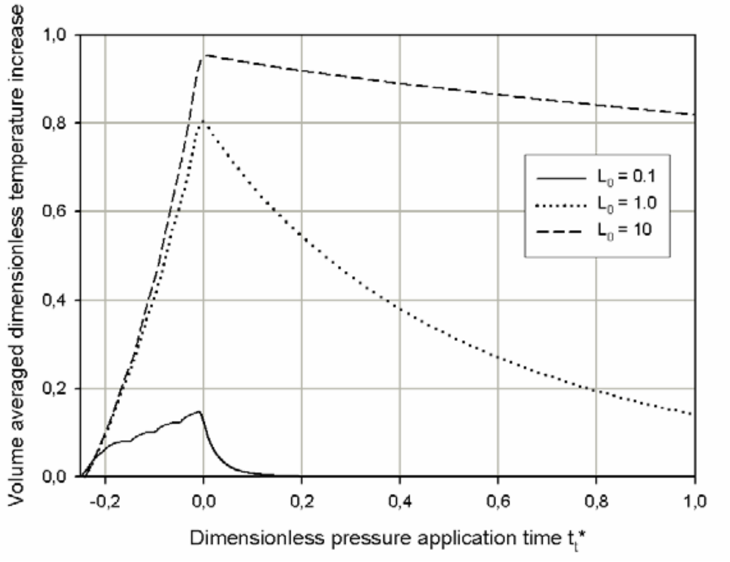

Figure 47 : Volume averaged temperature increase in 3 different autoclave configurations. The highest averaged temperature can be observed in the largest autoclave.

To discuss this in more detail, the volume averaged residual enzyme activity and its standard deviation is considered. In Figure 48 (left), it becomes obvious that the highest inactivation rate can be achieved in the largest autoclaves. Of all the 3 cases the standard deviation is the highest in the reference case with L_0 = 1 (0.31 m). In both the scale-down (L_0 = 0.1) and the scale-up cases (L_0 = 10), the standard deviations are significantly lower than that of the reference case (compare Figure 48 right).

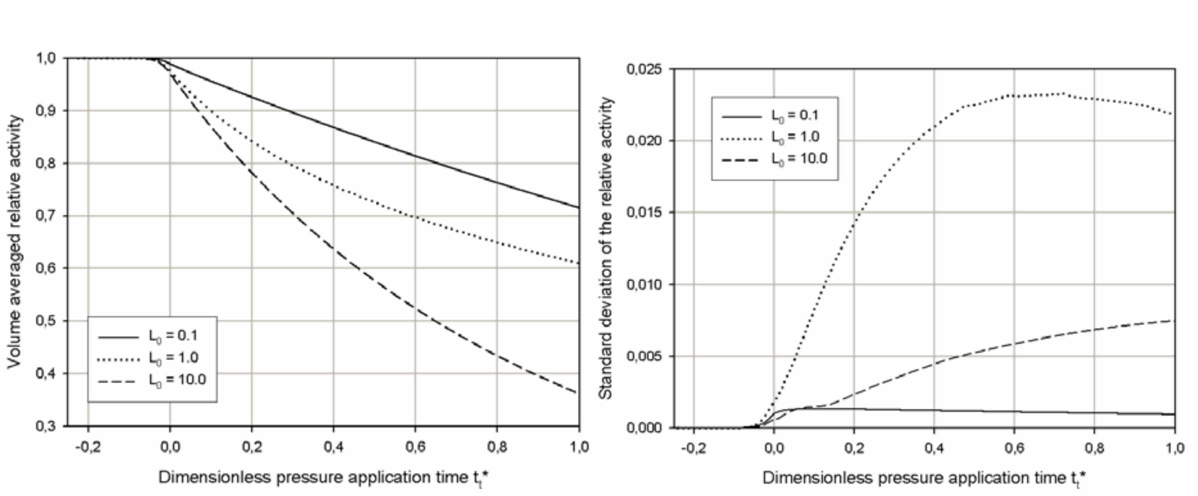

Figure 48 : Volume averaged residual enzyme activity (left) and the standard deviation (right) in the three autoclave configurations.

As can be seen in Table 14, the hydrodynamic and thermal compensation time scales have the same order of magnitude as the inactivation time scale in the lab-scale autoclave (3.3 ml volume). Thanks to this, the inactivation process is homogeneous as no larger differences in the time scales can be observed. In the 3.3 l autoclave, both the hydrodynamic and the thermal compensation time scales grow large compared to the inactivation time scale, where the hydrodynamic compensation scale is still relatively small compared to the thermal compensation time scale. Hence, heterogeneity of the products must then be awaited. In the 3300 l autoclave, however, the thermal compensation time and the hydrodynamic compensation time are both much larger (to be exact 5 orders of magnitude) than the inactivation time scale, so that the inactivation process is homogeneous here again. Hartmann [46] also considered these time scales for different configurations in order to explain the phenomenon of the heterogeneous mass conversion process, and similar results could also be observed. In general, it can be assumed that the risks of substantial heterogeneity of the product quality is high, when the time scale of the hydrodynamic compensation is small and the time scale of the thermal compensation is large compared to the time scale of the mass conversion process. However, since both the hydrodynamic and the thermal compensation time scales are subject to characteristic length scale (L_0), the values of both numbers might vary depending on the definition of the characteristic length scale. Therefore, these three characteristic numbers can only be considered as guidelines for the heterogeneity of the high process, but exact solutions can only be obtained with numerical simulations.

Table 14 : Time scales (s) for different configurations.

Process	Time scale	3.3 ml volume	3.3 l volume	3300 l volume
Hydrodynamic compensation	$\frac{\rho_0 L_0^2}{\eta_0}$	1,460 s	146,020 s	14,602,049 s
Thermal compensation	$\frac{\rho_0 L_0^2 c_{p0}}{\lambda_0}$	6,325 s	632,497 s	63,249,749 s
Inactivation	$\frac{1}{k_0}$	1,500 s	1,500 s	1,500 s

Therefore, it can be concluded that the uniformity of the high pressure treated products strongly depends on the size of the autoclave used. It becomes obvious that the scale-up process does not always lead to increased heterogeneity of the process. On the contrary, sometimes homogeneous product quality can also be reached even in very large autoclaves, where the compression induced temperature increase dominates. Therefore, significant non-uniformities of high pressure treated products can be found in middle-scale autoclaves, which will be used in industrial applications. In order to minimize the non-uniformity of the products, it is obvious that the thermal heterogeneity must be minimized first. The first way to achieve this is to try to gain better control of the given temperature. One might consider using inner tempering coils, which can temper the fluid from the inside of the autoclave, although the construction of autoclaves with inner tempering coils might prove to be problematic and not sufficient. The other way is to maximize the effects of the enthalpy increase due to compression. This can be achieved easily with the installation of a polymer layer to insulate the inner volume and reduce heat transfer between the wall and the fluid as discussed already in previous chapters.

4.2.7 Effects of the pressure ramps

As the devices used in the high pressure techniques are also improved, particularly the improvements in the mechanical engineering and the automation sector enable different configurations of how the high pressure treatment can be carried out. However, as different pressure ramps cause different temperature increase and might cause different flow behaviors, the effects of different pressure ramps must also be studied.

Therefore, the current part of the study is carried out with the aim to examine the effects of different pressure compression rates. Especially the effects due to the change of the inlet diameter based Reynolds number (Re_d) on other characteristic dimensionless groups should be examined in the first place. Furthermore, how these changes in the dimensionless numbers and groups affect the uniformity of the process shall also be studied. The configuration of the reference case with $Re_d = 2279$ is also used, but the simulations are carried out at different pressure ramps at $Re_d = 570$ and $Re_d = 6838$. Especially the change of the characteristic dimensionless numbers and groups are of interest in this case.

Firstly, it should be mentioned that the change of the Reynolds number also means the change of the flow pattern. With growing Reynolds numbers, the instability of the flow grows and the flow becomes turbulent. The critical Reynolds number of a plane jet depends on the shape of the exit jet profile, disturbance amplitude and dimensionality. The instability of axisymmetric jets was discussed by Sato [89], Batchelor and Gill [109], and Grant [110]. Although the critical Reynolds number, where the flow turns turbulent, under high pressure is not yet known, it is known from incompressible flows that the critical Reynolds number of jet flows are small, for Andrade [111] found the Reynolds number of a plane jet for transition to turbulence to be 33. However, the change from the laminar to the turbulent flow pattern is transitional. The intensity of the turbulence hence depends on the Reynolds number. The higher the Reynolds number, the more turbulent the flow pattern then is.

Concerning the free jet itself, the free jet reaches the top of the autoclave in every studied case. In the case with the lowest Reynolds number, the jet reaches the upper wall of the autoclave much slower than in the other two cases. In the case with the highest Reynolds number, the momentum of the free jet is high enough that the flow reaches the top of the autoclave throughout the entire compression phase. In the case with $Re_d = 2279$, however, the momentum is not as high and during the second half of the compression phase, the free jet is disturbed by the downward-directed flow movement of the fluid due to the free convection caused by the cooling of the fluid at the upper wall. Therefore, interactions can be observed in terms of counter-rotating vortices in the upper region of the autoclave.

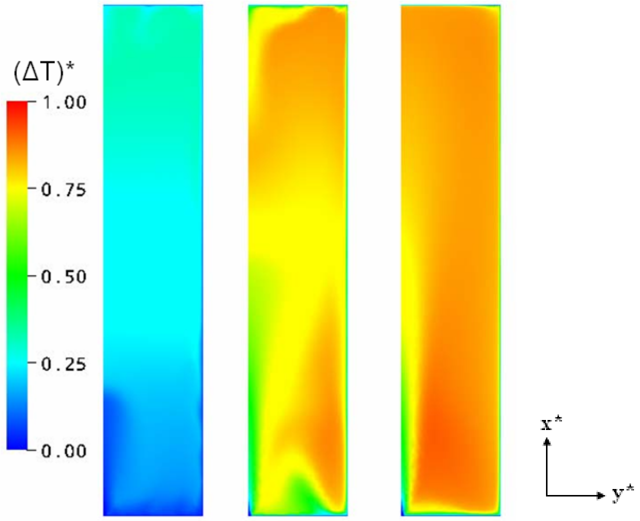

Figure 49 : Temperature distribution at the end of the compression phase of high pressure processes with Re = 570, 2279, 6838 from left to right respectively.

How the change of the Reynolds number affects the other thermofluiddynamical processes becomes visible in Table 15, where the other dimensionless numbers and groups are listed. It becomes obvious that the change of the Reynolds number affects all the terms with velocity components. Furthermore, it can also be observed that the terms representing the free convection also differ from the reference case.

Table 15 : Characteristic dimensionless numbers or groups during the high pressure applications at p* = 1 with three different pressure ramps.

Re_d	Pr	Fr	Ec	$\alpha_0 T_0$	Gr	Ra
570	4.33	5.14×10^{-3}	1.19×10^{-8}	0.112	2.37×10^{9}	1.03×10^{10}
2279	4.33	0.08	1.9×10^{-7}	0.112	3.33×10^{9}	1.44×10^{10}
6838	4.33	0.74	1.72×10^{-6}	0.112	3.58×10^{9}	1.55×10^{10}

With increasing Reynolds number, the Froude and the Eckert numbers grow due to larger velocities. In particular, the change of the Froude number is visible in the thermal and velocity distribution as the inertial forces becomes larger compared to the gravitational forces, which remain constant. Therefore, the flow pattern of each case is different as can be seen from the previous Figure 49. The change of the Eckert number, however, is not significant enough to become apparent. Even at $Re_d = 6838$, the velocities are still too slow (with $Ec = 1.72\times10^{-6}$), so that the dissipation effects can still be neglected. It is known that the Eckert number correlates with the quadratic Mach number. Only when the Mach number of $Ma \geq 0.3$ 10 % of dissipative effects can be reached ($Ec \approx 0.1$). As the speed of sound of water is at approximately 1500 m/s, to reach 10 % dissipative effects, water as pressure fluid must enter the chamber at approx. 500 m/s. This, however, is hardly possible at the moment due to restrictions of the pressure build-up machines. In order to reach this speed, water must be pumped into the studied chamber with a pump, which could pump at least 3.5 liters of water in one second, that means 12600 l/h (conventional pumps achieve up to 1000 l/h)! That is not possible at the moment. Therefore, it can be concluded that dissipation does not play an important role in the high pressure treatment, as the velocities of the fluid are much too small.

The change in the Grashof and the Rayleigh numbers are due to the change in the temperature increase. As higher Reynolds number also means faster pressure ramps, the same pressure can then be reached in shorter period of time. At approximately the same heat flux, this would lead to less heat loss at the wall and, therefore, higher temperatures and Grashof and Rayleigh numbers. The higher these two numbers are, the more unstable the free convective flow will be. Therefore, the flow might become more turbulent at the walls. In all the studied cases, the critical Grashof number of approx. 10^9 can be reached. Therefore, it can be assumed that turbulent flow conditions at the vertical wall of the autoclave can be found during the high pressure treatments.

How all these changes affect the uniformity of the conversion processes can be seen in Figure 50, which illustrates the distributed residual enzyme activity after 10 min of pressure holding at 500 MPa. In every case, more inactivation can be observed in the upper-corner region of the chamber due to generally higher temperatures. In the case with the slowest pressure ramp, the residual activity is the highest among the 3 cases due to lower temperature throughout the compression and holding phase (see also Figure 51) and varies between 70 – 74 % In the case with the fastest pressure ramp, the range of the residual activity between 58 – 72 % represents the lowest of the 3 cases examined here.

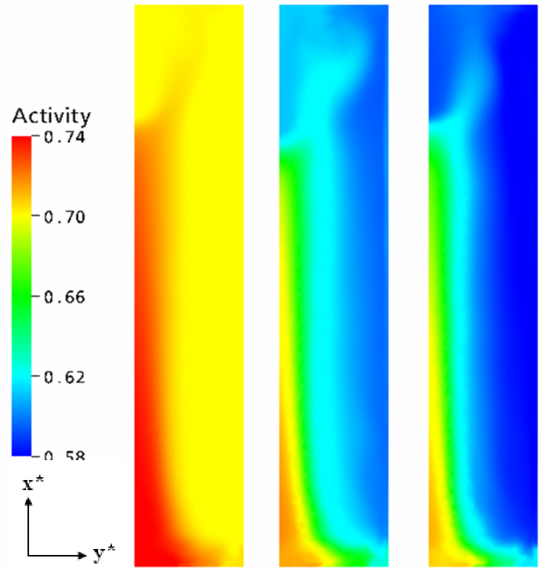

Figure 50 : Distributed residual enzyme activity at t_t^* = 1.0 at Re_d = 570, 2279 (reference case) and 6838 from left to right respectively.

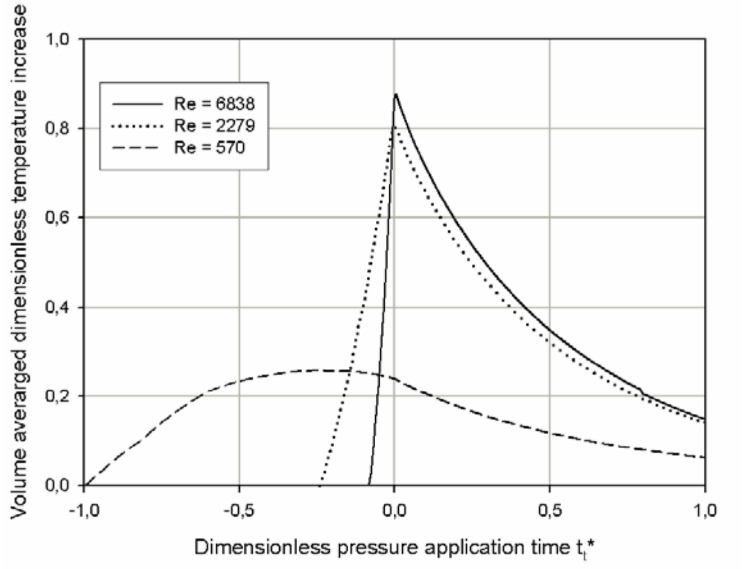

Figure 51 : Volume averaged temperature increase of the pressure fluid during a high pressure treatment of p* = 1.0 at Re_d = 570, 2279 (reference case) and 6838 from left to right respectively.

Figure 52 (left) shows the volume weighted-averaged results of the high pressure enzyme inactivation process at p* = 1.0 of all the 3 study cases. The time t_t^* = 0 marks the beginning to the holding phase, whereas the minus array represents the compression phase. Although the process with the slow pressure ramp with Re_d = 570 has a head start with more inactivation already during the compression phase (from 100 down to 95 %) thanks to the longer duration of its compression phase, the other cases with faster pressure ramps can both catch up with it and reach the same residual activity of approx. 87 % after t_t^* = 0.1. This is due to higher temperature increase during the compression phase in the cases with faster pressure ramps (see also Figure 51). At t_t^* = 1.0, the most enzyme inactivation with the final mediate residual enzyme activity of approx. 60% can be observed in the process with the fastest pressure ramp at Re_d = 6838, followed by the process with the pressure ramp at Re_d = 2279 (reference case) with the averaged residual activity of approx. 61% and 0.83 MPa/s with final volume weighted-averaged residual activities of 70%. This shows the possibility of using faster pressure ramps to enhance the effectiveness of the high pressure conversion process, so that the process cycle duration can be reduced and the economic efficiency increased.

The standard deviation of the volume-weighted average of the residual enzyme activity is considered as a measure of the heterogeneity of this high pressure mass conversion process and is also illustrated in Figure 52 (right). In the case with the slowest pressure ramp on the one hand, the process heterogeneity of the conversion process can already be observed in the second half of the compression phase. The heterogeneity reaches its maximum at t_t^* = 0.5 and then begins to fall. In the cases with faster pressure ramps on the other hand, the heterogeneity of the conversion process is prominent only during the pressure holding phase, where the heterogeneity reaches its maximum at approx. t_t^* = 0.7 in both cases. It can also be observed that the heterogeneity is always slightly higher in the case with the fastest pressure ramp at $Re_d = 6838$ than the reference case with $Re_d = 2279$ due to its higher temperature and longer thermal compensation time. Anyway, the heterogeneity of the mass conversion decreases with increasing pressure holding time in every case.

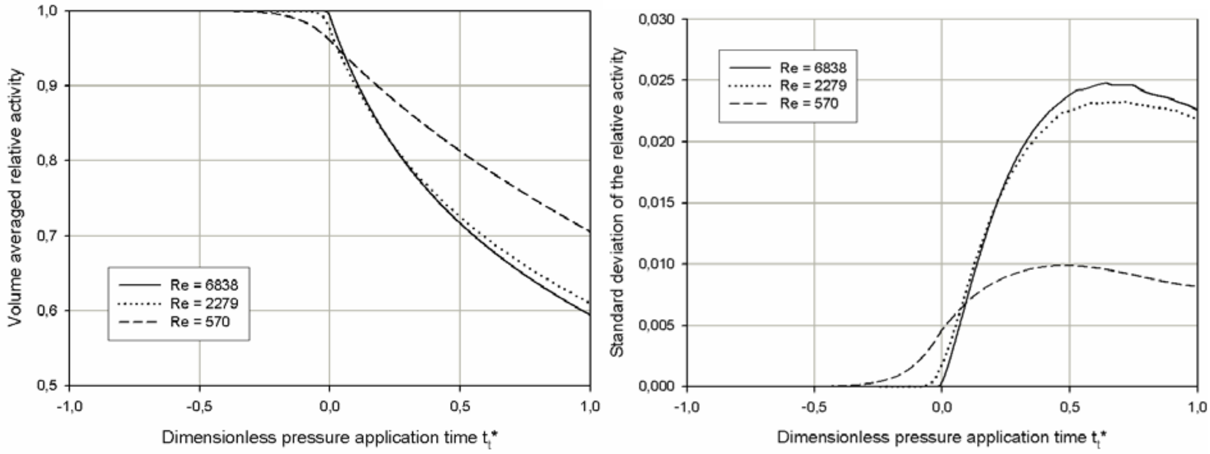

Figure 52 : Volume averaged residual enzyme activity (left) and the standard deviation (right) during high pressure treatments with different pressure ramps.

4.2.8 Effects of the position of the autoclave

In real high pressure applications, there are not only vertical but also horizontal autoclaves, which are placed horizontally. Therefore, it is of interest to carry out a numerical simulation of such an autoclave. Because the rotational symmetry cannot be applied here, the axis symmetric mesh introduced in chapter 3.1.1 is used in order to save computational costs.

Overall, the flow behavior of the free jet in this case is different from that in vertical autoclaves (compare Figure 27, Figure 28 and Figure 53). In this case the cold inflow jet is directly bent towards the bottom of the autoclave due to buoyancy forces right after its penetration into the chamber. As a result, the volume of the autoclave can be subdivided into two regions: the upper part with adiabatic temperature and the colder lower part due to the temperature of the free jet. Free convections can also be observed at the wall. At the upper wall, smaller vortices can be observed due to the descending fluid, which is cooled by the cold upper wall.

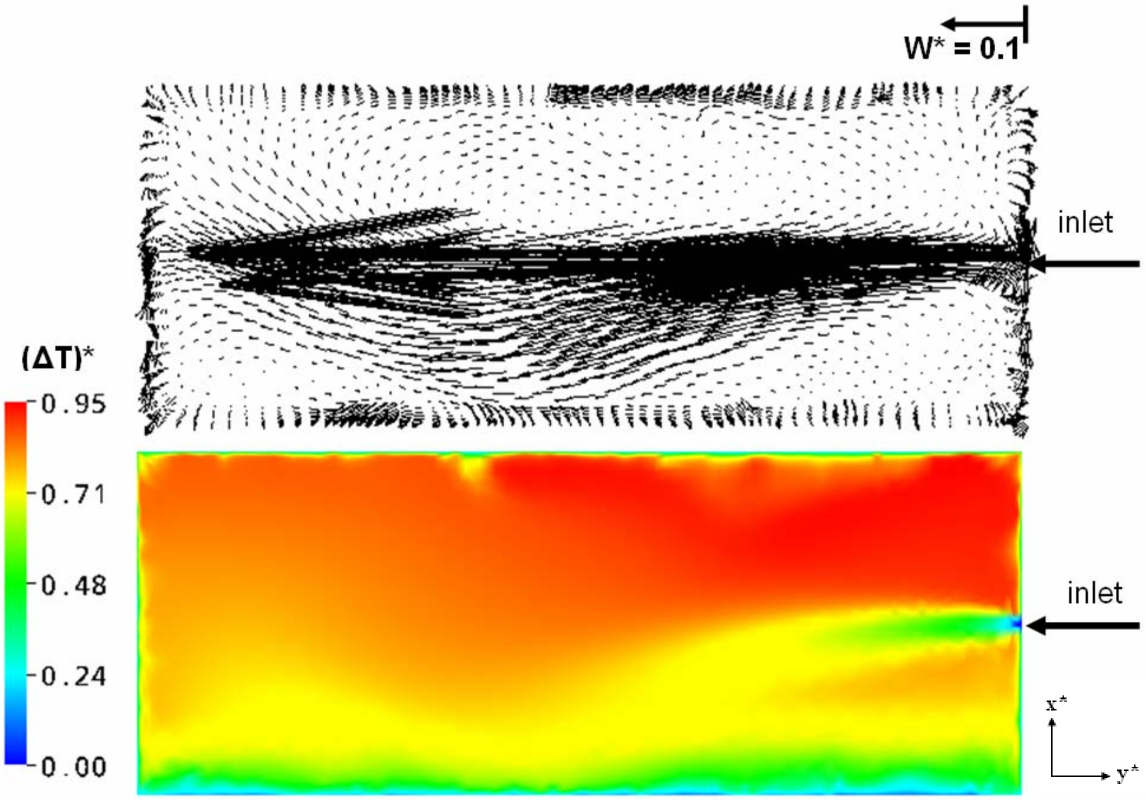

Figure 53 : Velocity vectors and temperature distribution in a horizontal high pressure autoclave at the end of the compression (and the beginning of the pressure holding phase with $t_t^* = 0$).

Considering the characteristic dimensionless groups of the thermofluiddynamical processes during the high pressure application with horizontal autoclaves, some deviations from vertical autoclaves can be seen. Due to the reduction of the height of the autoclave by placing the autoclave horizontally, the interactions between the gravitational forces and the forced convection due to the free jet are different from those in a vertical autoclave. The slightly higher Froude number of 0.12 in the studied horizontal configuration compared to 0.08 in the reference vertical case shows slightly reduced effects of the gravitational forces. The downward directed motion of the fluid at the vertical wall due to free convection is also less significant due to the reduced height of the autoclave. This can be seen in the smaller Grashof and Rayleigh numbers.

Table 16 : Characteristic dimensionless numbers and groups of the studied vertical and horizontal high pressure autoclave.

Position	Re_d	Pr	Fr	Ec	$\alpha_0 T_0$	Gr	Ra
Vertical	2279	4.33	0.08	1.9×10^{-7}	0.112	3.33×10^{9}	1.44×10^{10}
Horizontal	2279	4.33	0.12	1.9×10^{-7}	0.112	1.95×10^{8}	8.48×10^{9}

Last but not least, the distribution of the residual enzyme activity also differs from that in vertical autoclaves. Due to the temperature gradient (compare Figure 53) the distribution of the residual enzyme activity is also not homogeneous. Similar to the vertical autoclaves (Figure 35), it can be generally said that more enzymes can be inactivated in the warmer upper region of the autoclave. However, the distribution of the residual enzyme activity in a horizontal autoclave is different from that of the vertical autoclave (compare Figure 54). This is due to different flow patterns resulting from the change of the position of the autoclave.

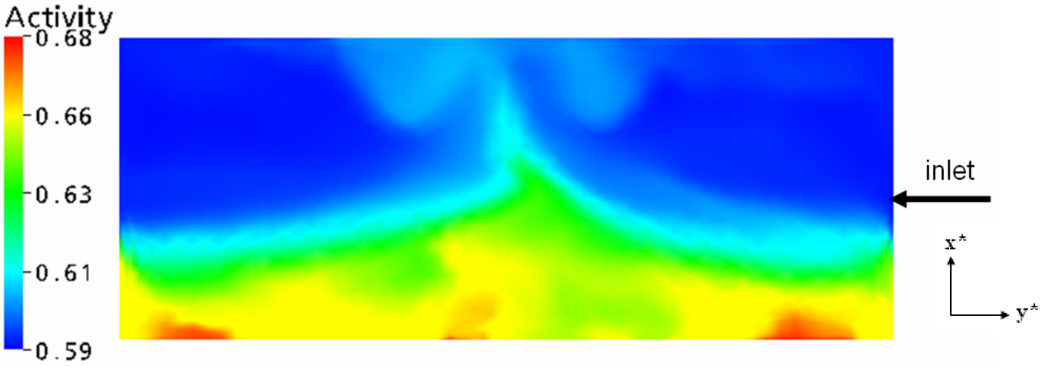

Figure 54 : Distribution of the residual enzyme activity in a horizontal autoclave.

Meanwhile, it is interesting to observe how the change in the position of the autoclave can affect the homogeneity of the products. Although the effectiveness of both autoclave types are the same (Figure 55 left), the horizontal autoclave seems to deliver a somewhat better product homogeneity (Figure 55 right), as the standard deviation of it is approx. 3% smaller than that of the vertical autoclave. This is due to the reduced height of the autoclave, so that the mixing of the warm and cold fluid as a result of the free convection is more intensive. Therefore, a little better homogeneity can also be reached just by placing the autoclave horizontally. Although this might not bring significant enhancements, it can also be considered as a small improvement of the mass conversion process.

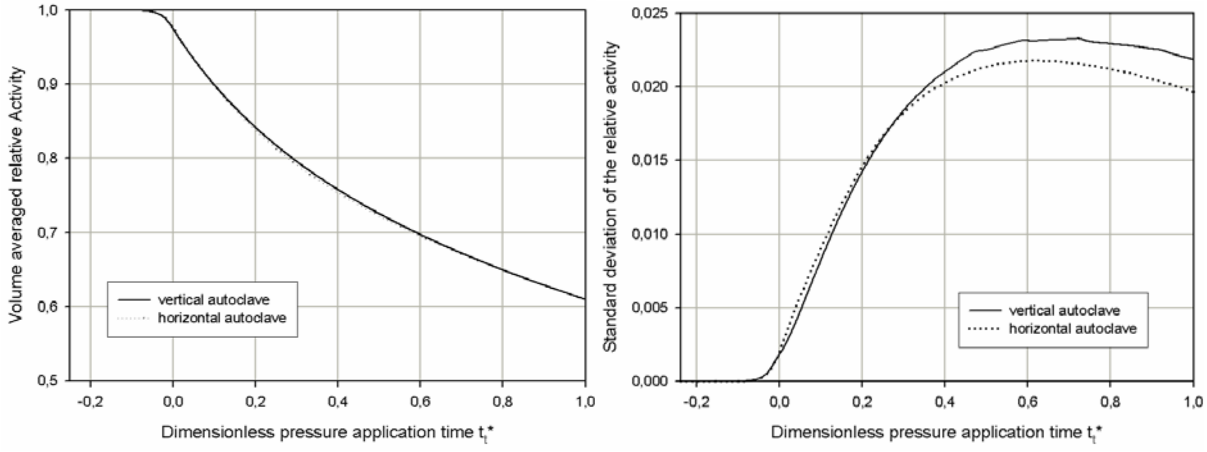

Figure 55 : Volume averaged residual enzyme activity (left) and the standard deviation (right) in the vertical and horizontal autoclaves.

Overall, it could be shown that the thermal heterogeneity caused by forced and free convection during the whole pressure treatment has crucial influences on the effectiveness and the uniformity of the mass conversion processes, i.e. protein denaturing or inactivation of enzymes or microorganisms. However, especially for microorganisms there are still no reports on the non-uniformity of the high pressure inactivation process in larger-scale autoclaves as yet. Furthermore, there are microorganisms, which inactivation kinetics does not obey the 1st order kinetics due to their pressure resistant population. Therefore, the last chapter of this work will illustrate the non-uniformity of the high pressure inactivation process of lactic acid bacteria in a 3.3 liter autoclave. Both numerical and experimental results will be discussed. Especially the aspects concerning the food safety during the high pressure processing will be emphasized.

4.3 Non-uniformity during high pressure inactivation of microorganisms

In the last chapter, it will be shown that the temperature gradient existing in the autoclave leads to non-uniformity of the temperature-dependent mass conversion processes, i.e. inactivation of enzymes or microorganism. Moreover, recently there have been many reports on the pressure resistant populations of microorganisms that could survive the high pressure treatment no matter how long the pressure is held. This effect is called the tailing effect of microorganisms. For instance, bacteria exhibit a maximum resistance against pressure at ambient temperature or a few degrees below their growth temperature [112, 113]. *L. lactis* exhibits maximum resistance to pressure when treated at a temperature of approximately 10°C below the growth temperature [114]. Because the presence of pressure-resistant fractions within populations of target organisms represents a risk for contamination, the possibility of eliminating prominent tails in survivor curves by a mildly elevated temperature seems to be necessary. This important fact has to be taken into account especially in industrial application of HP due to that fact, that isothermal conditions can hardly be observed especially during the high pressure treatments in autoclaves with larger volumes, where the temperature increase is not homogeneous throughout the entire autoclave (see section 4.2).

Considering high pressure inactivation of microorganisms, current performance standards require a legally enforced 5 log reduction of contaminating bacteria in food production (5D-concept) [115]. Furthermore, pressure treated cells are sublethally injured and fail to survive or grow in adverse bactericidal environmental conditions [116, 117, 118]. On the other hand, the bactericidal effect of pressure may be reduced by certain baroprotective additives. In particular, sucrose in molar concentrations prevents pressure-induced inactivation of bacteria even at pressures of 400 to 600 MPa. Furthermore, certain compounds may cause opposite effects during and after the high pressure treatment. For example, high levels of NaCl protect against pressure induced inactivation. On the contrary, sublethally injured cells are killed during extended exposure to high NaCl levels after pressure treatment at ambient temperature.

Thus, it is known that microbial inactivation depends strongly on pressure, temperature and the additives used. However, only few incomplete and empirical models accounting for these parameters exist. Furthermore, there is no validated model for the inactivation of bacteria in a medium or large scale high pressure autoclave considering the temperature heterogeneity as yet.

Thus, in collaboration with Dr.-Ing Klaus Kilimann, who is specialized in modelling the inactivation kinetics of microorganisms at the same institute as the author, the inactivation kinetics of *L. lactis* is investigated in terms of process heterogeneity. The primary aim of this collaboration is to analyse the non-uniformity of the inactivation of *L. lactis* in a 3.3 liter high pressure autoclave experimentally and numerically. In order to formulate a predictive microbial model for the inactivation of *L. lactis*, experiments were carried out in a 10 ml autoclave. This predictive model should take into account: pressure, temperature, additives found in the food matrix as well as the shoulder and tailing effects of the bacteria. Subsequently, this model should be combined with the High Pressure Computer Fluid Dynamics (HP-CFD) technique in order to investigate the heterogeneity of the inactivation process of *L. lactis* in a medium size high pressure autoclave numerically. Moreover, this work should provide a detailed analysis of baroprotective co-solvents and their influences on the inactivation characteristics in the high pressure application.

However, it should be mentioned that the additives used in this study have strong effects on the rheology of the treated food matrix. As there are no sufficient data for the rheological property of the treated substances, the author has decided to design an experimental setup, where the movement of the treated food can be neglected. More on this will be explained at a later point.

4.3.1 Formulating the inactivation model

The predictive modelling method used in formulating the inactivation model of *L. lactis* is discussed in Kilimann's PhD thesis [119] thoroughly and, thus, shall be explained only briefly. Overall, 3 models for lethal and sublethal injury effects caused by the high pressure application in 3 different food matrices are developed: one for the neutral matrix (milk buffer), one with high sucrose concentration of 1.5 M and the last one for extremely high salt concentration of 4M NaCl. The sucrose and NaCl concentrations used here represent the highest concentrations of both additives that could be found in the food industry. Thus, the scenario shown in this study can be considered as worst case studies. Experiments were carried out in a 4 ml autoclave at different temperature and pressure levels with various pressure holding durations. A numerical simulation of the temperature increase inside this 10 ml autoclave and series of measurements with thermocouples could prove that the temperature increase inside the 10 ml autoclave is relatively small, and that this temperature gradient disappears shortly after the pressure holding phase begins (see Figure 56). The pressure fluid can be cooled down to the temperature of the tempering bath quickly so that the time-averaged mean temperature of the whole process amounts up to only 0.018. Therefore, the temperature increase in the 10 ml autoclave is not considered in the model formulation.

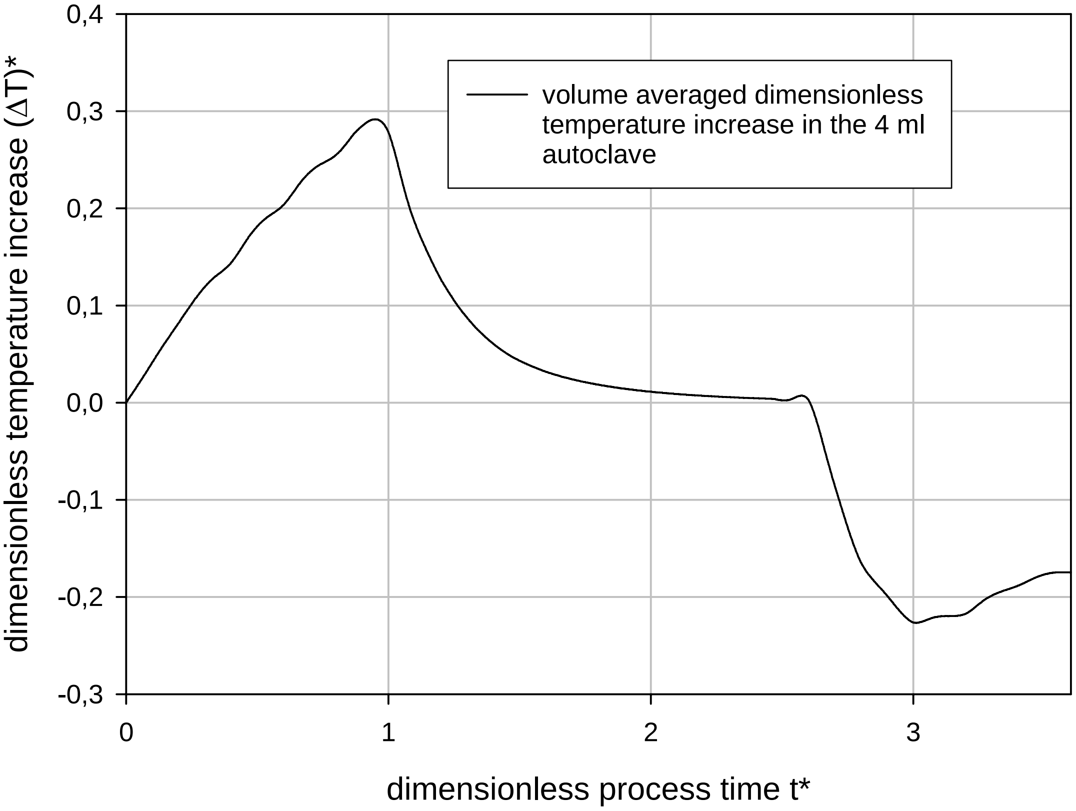

Figure 56 : Volume averaged dimensionless temperature increase in the 10 ml autoclave, as calculated by CFX-5.7, is relatively small. Furthermore, the pressure fluid is cooled down to the temperature of the tempering bath quickly. The time-averaged mean temperature of the whole process amounts up to only 0.018.

In order to create a mathematical model for the inactivation kinetics of *L. lactis*, microbiological inactivation data were transformed in the following steps. First, all control values of the same buffer system were averaged. This control value was used for all measured data belonging to one used buffer system. This data set was divided through its averaged control value. As a result of this step, data was set between 0 and 1. However, with this kind of data, no prediction of the residual population can be obtained. Therefore, data were logarithmized and then log-linearized. Due to this linearization, growth functions have been calculated representing the original data.

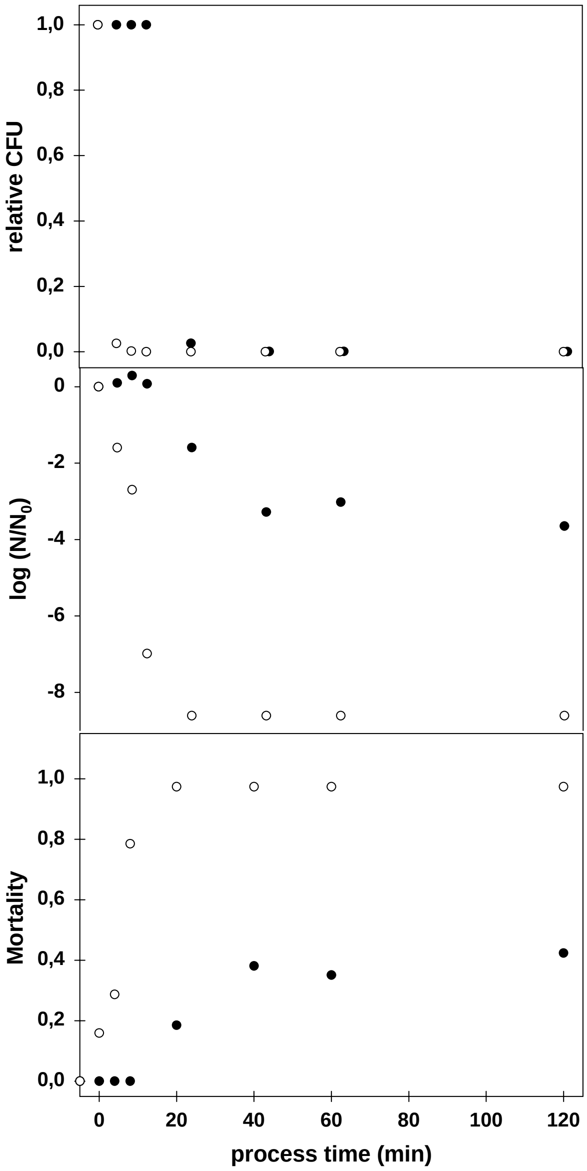

Figure 57 : Graphical explanation of the used transformation of microbiological inactivation data to obtain logistic growth data. Symbols represent data at either 30°C (●) resulting in a pronounced tailing or at 50°C (○), where no tailing was visible.

One of the most fundamental models of growth in a closed environment is the continuous logistic equation also called the Verhulst or Verhulst-Pearl model [120]. In this work, the function is used as a “mirror” function to describe pressure induced cell death. It can be written as

$$M(t) = \frac{M_{Max}}{1 + \exp\left(-m\left(t - t_0\right)\right)} \tag{4.5}$$

where the Mortality M(t) represents the inactivated fraction of the population, M_{Max} is the maximal possible inactivated population, m denotes the slope, and t_0 is the time to reach 50% of M_{Max}. The transformed inactivation data of *L. lactis* were fitted using this “mirror” function. The pressure, temperature and additive dependent constants M_{Max}, m, and t_0 where calculated using either Gauss distribution function or sigmoid functions with 4 parameters to determine the influence of the environment [119].

Figure 58 shows the maximum reduction of the viable cell counts at different temperatures and pressures according to the model developed from the experiments in the 10 ml autoclave. The inactivation data for the additive NaCl is similar to those of Sucrose and shall not be shown here.

In lab-scale autoclaves with small volumes, the temperature increase inside the autoclave is not significant due to better tempering thanks to thinner walls. Thus, the inactivation developed here (Figure 58) can be applied in smaller autoclaves without modifications. However, in autoclaves with larger volumes the temperature increase is significant. Furthermore, as shown in section 4.2 the temperature distribution inside the autoclave is local and transient. This has substantial influences on the uniformity of the pressure induced inactivation process of *L. lactis*.

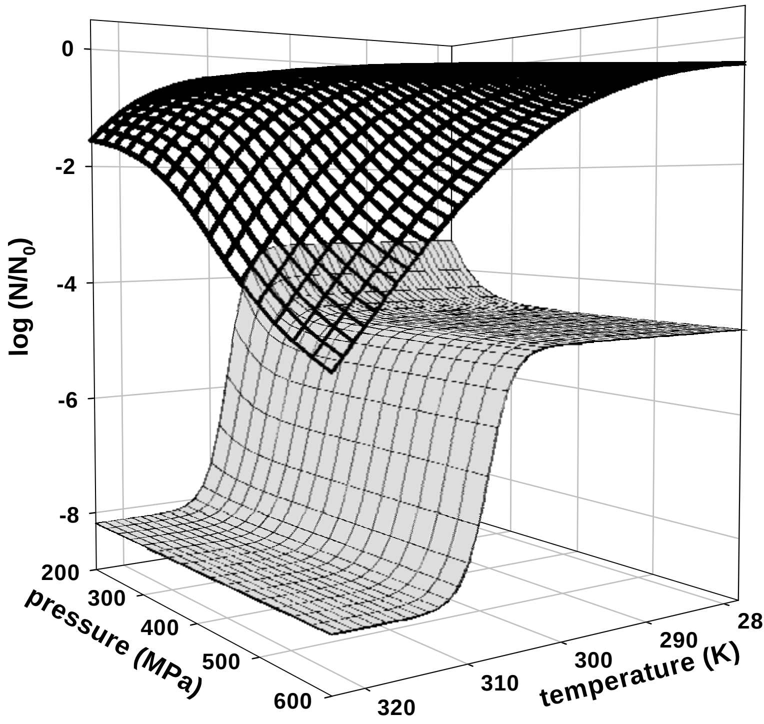

Figure 58: Distributions of $\log(N/N_0)$ of viable cell counts after pressure-temperature processing using sucrose (▭) or milk buffer (▨)

Therefore, in order to predict the high pressure induced inactivation process of microorganisms in larger autoclaves, the thermal heterogeneity inside the autoclave must also be considered. In order to calculate the local and transient Mortality rate, which depends on both pressure and temperature the equation (4.1) must be rewritten as a differential equation as follow:

$$\frac{dM}{dt}=\left(1-\frac{M\left(p,T,\vec{x},t,additives\right)}{M_{Max}}\right)\cdot m\cdot M\left(p,T,\vec{x},t,additives\right). \tag{4.6}$$

With this equation, the Mortality can be coupled with the temperature and pressure calculated by CFX-5.7. Thanks to the extremely thin wall and the excellent heat transfer properties of the PCR-tubes, used to contain the *L. lactis* probes, it can be assumed that the temperatures inside the PCR-tubes are always the same as those of the surrounding fluid. Thus, the temperatures of the fluid next to the PCR-tubes will be used to calculate the Mortality and the reduction of the cell counts after the high pressure treatment. Furthermore, no fluid motion inside the PCR-tube is considered due to its small size.

4.3.2 Temperature distribution and the flow field

Firstly, the temperature distributions and the flow field of the fluid inside the 3.3 liter autoclave at different process temperature is calculated with CFX-5.7. The target pressure of $p^* = 1.0$ (500 MPa) is built up within 150 seconds, which represents the characteristic time scale for this study, as the pressure holding time varies between 4, 8, or 12 minutes. Therefore, the transformed dimensionless time is introduced as follow:

$$t_t^* = \frac{t^*}{t_{Max}^*} = \frac{t^*}{t_{compression\ phase}^*}. \tag{4.7}$$

At the end, the decompression lasts also 150 seconds. The simulation for the compression, pressure holding and the decompression phase are carried out. As shown in Figure 59 the temperature distributions and flow field of the fluid is spatial and transient. This thermal non-uniformity leads to non-uniformity in the inactivation process of microorganisms or enzymes as well.

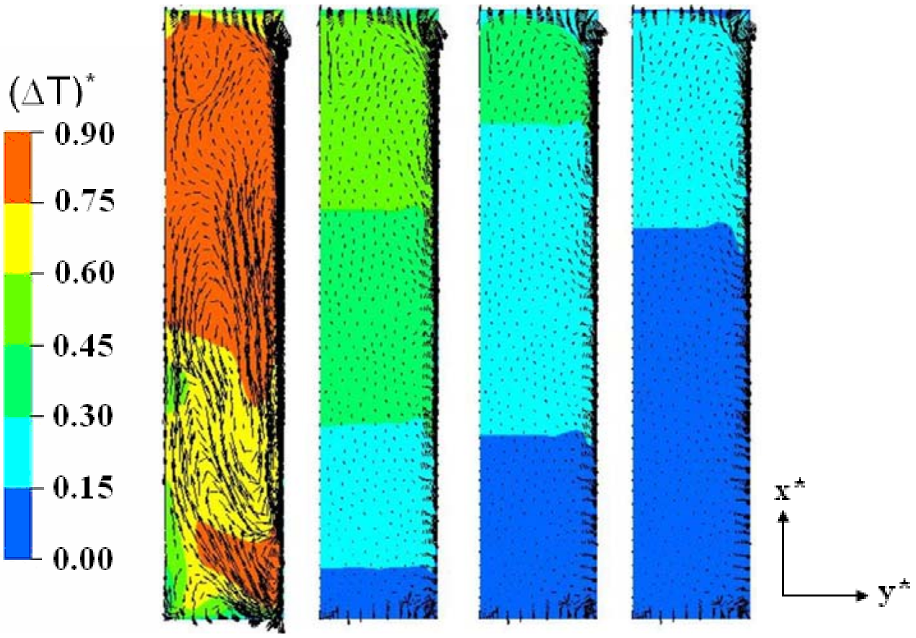

Figure 59 : Temperature distribution and flow field inside a 3.3-l high pressure autoclave tempered at T_0 = 301 K with working pressure of approx. 500 MPa. The figure shows the distributions at t_t^* = 1, 2.6, 4.2 and 5.8 of a pressure treatment (at the end of the compression phase, after 4, 8 and 12 minutes of pressure holding) from left to right respectively.

4.3.3 Non-uniformity of the inactivation process of *L. lactis*

The non-uniformity of the inactivation process of *L. lactis* is investigated both experimentally and numerically. The inactivation processes in 3 different food matrices are considered: in neutral medium, in medium with high salt concentration and in a medium with high sugar concentration. The experiments are carried out in 0.2 ml PCR-tubes (Brand, 78 13 00) installed at 2 different locations in a 3.3 liter autoclave. The positions of both PCR-tubes can be found in Figure 60. It should be mentioned that the movements of the fluids inside the PCR-tubes are not considered. Therefore, the determination of the viscosity of each food matrix is not needed here. Furthermore, due to the small size of the PCR-tubes (0.2 ml) and the excellent heat transport property of the polypropylene, which is the only component of the PCR-tubes used during this work, it is assumed that the temperature of the food matrix inside the tube is equal to the temperature of the surrounding pressure fluid. Therefore, it is enough to calculate the temperature of the pressure fluid at the locations of the tubes, which can simultaneously be assumed as the temperature inside the tubes.

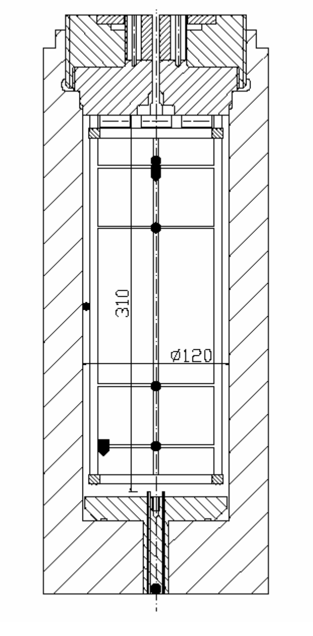

Figure 60: The locations of the PCR-tubes containing cells of *L. lactis* (♥)

The calculation of the inactivation of *L. lactis* is carried out subsequently using the numerical temperature and pressure data at both locations of the PCR-tubes. Firstly, cubic splines for temperatures and pressures at both points are created. Secondly, a FORTRAN 90 program is written containing the subroutine for the calculation of the Mortality as shown in 4.3.1.

Linking this program with the created splines, the Mortality at both locations can be achieved. The Mortality can then be retransformed as the reduction of the cell counts log(N/N_0) by multiplying it with a factor as given in the model of Kilimann [119]. Here, the results in all the 3 food matrices shall be discussed. However, only 3 representative cases will be explained thoroughly. Overall, for this part of the work, more than 40 GBytes of data were created, mostly for the calculation of the thermofluiddynamical parameters. More than 50 simulations were carried out over a period of 3 computational months with 4 computers running in serial or parallel mode.

4.3.3.1 Milk buffer

The probe with the milk buffer represents the neutral food matrix without any additives. This case can be considered as the reference case. In this case, the inactivation processes with $T_0 = 301$ and 304 K are carried out. As explained in 4.3.2, the temperature and pressure distributions inside the 3.3 liter autoclave are calculated first. Especially the temperatures at the locations of both probes as shown in Figure 61 are of interest. It can be concluded that the temperature in the upper probe is always higher than that of the lower probe.

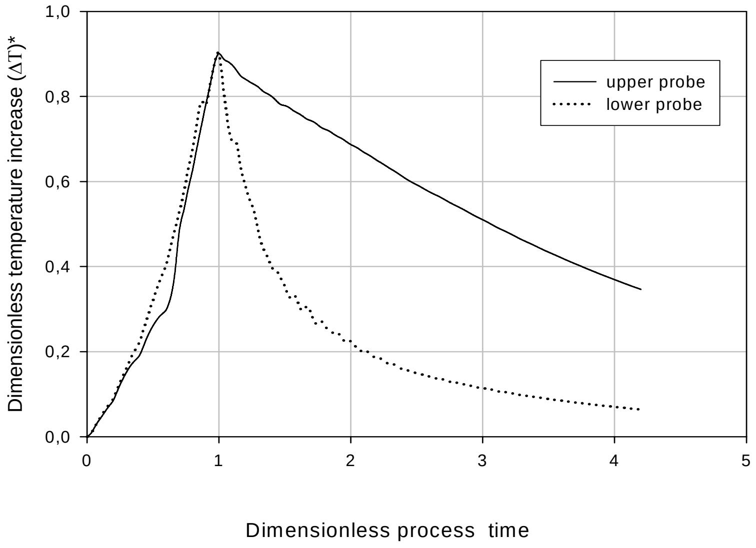

Figure 61 : Calculated dimensionless temperature increase at the locations of the PCR-probes inside of the 3.3 liter autoclave at $T_0 = 301$ K during the compression and the pressure holding phase.

To illustrate the combined effects of temperature and pressure, the temperature-pressure pairs at both locations during the whole pressure treatment are shown in combination with the maximum reduction of microorganisms achievable (maximum $\log\left(\frac{N}{N_0}\right)$) at given temperatures and pressures, which represent the tailing effects of *L. lactis* in milk buffer. As microorganisms in both probes are exposed to different temperature-pressure combinations, microorganisms in both probes show different tailing strength (pressure resistance) as can be concluded from different maximum $\log\left(\frac{N}{N_0}\right)$. Therefore, different inactivation rates during the high pressure treatment of both probes are expected.

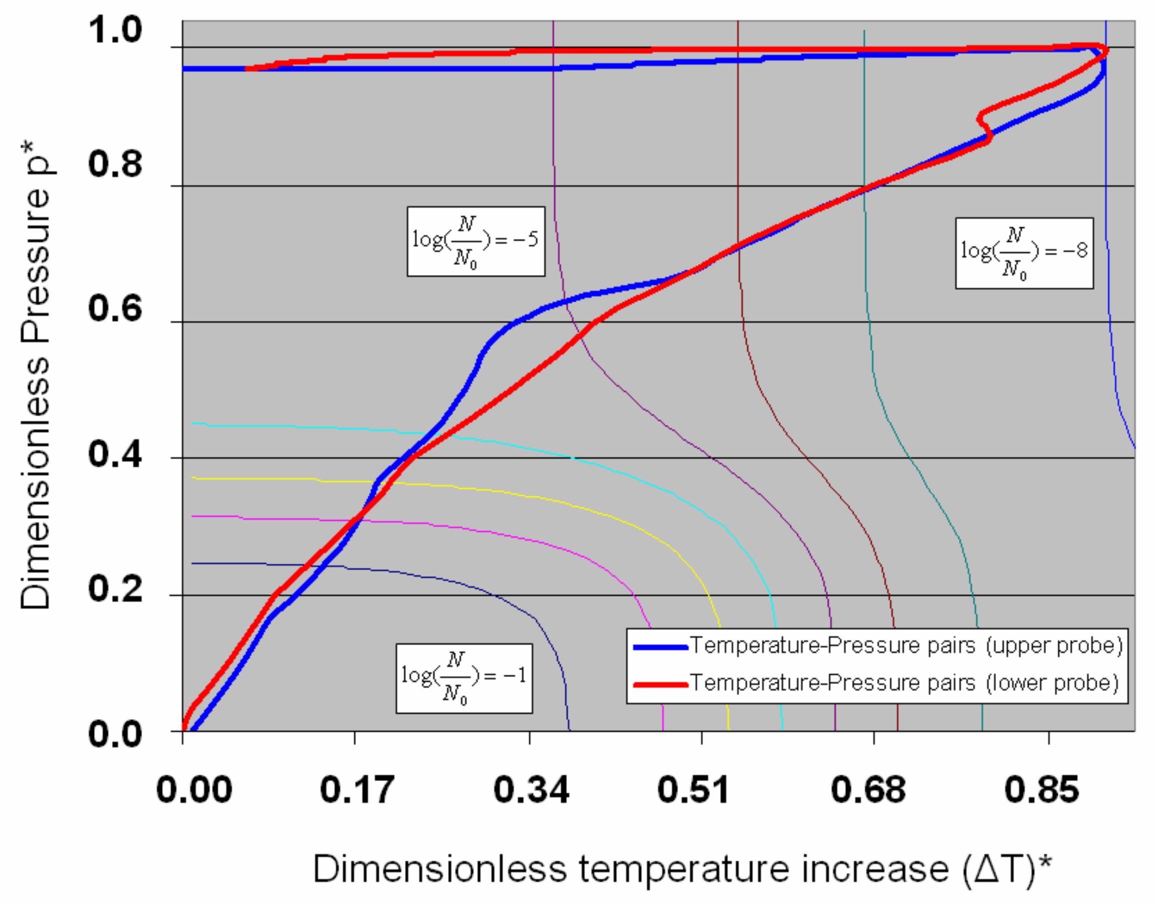

Figure 62 : Temperature-pressure pairs in both PCR-probes compared to the maximum achievable reduction of *L. lactis*. It can be seen that both probes are exposed to different temperature-pressure combinations, so that the microorganisms in both probes show different tailing (pressure resistant) strength.

Subsequently, the calculated temperatures and pressures of both probes are linked to the main FORTRAN 90 program, where the inactivation of *L. lactis* at 2 different locations can be calculated. Figure 63 illustrates the reduction of viable and stress resistant cell counts of *L. lactis* at p* = 1.0 (500 MPa) and T_0 = 301 K taking into account the temperature non-uniformity shown in Figure 59 and Figure 61.

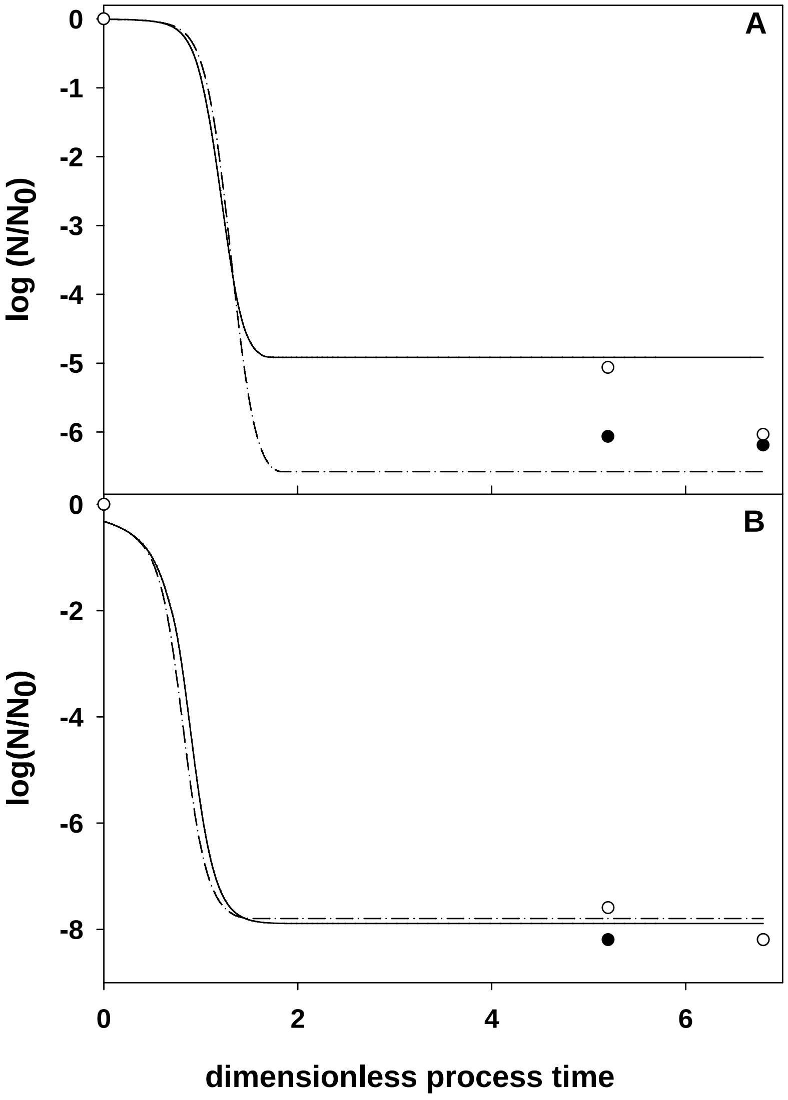

Figure 63: log(N/N$_0$) of *L. lactis* inside the PCR-tubes after 1020 seconds of pressure treatment (t_t^* = 6.8) at p* = 1.0 (500 MPa) using milk buffer as pressure medium. The start temperature is set at T_0 = 301 K (A: viable cell counts. B: stress resistant cell counts). Dotted and solid curves represent the calculated cell count reduction of the upper and the lower probes respectively. The measured data are shown as (●) for the upper and (○) for the lower probe.

At this temperature a reduction of approx. 7 log and 5 log of viable *L. lactis* can be observed in the upper part and at the bottom of the autoclave respectively. The tailing behaviour can be validated with longer pressure holding time. After pressure treatments with t_t^* = 5.2 and 6.8 (780 and 1020 seconds), both the numerical simulation and experimental results show no significant further reduction of viable cell counts.

The complete results for the viable cell counts, which are illustrated in Table 17, confirm the importance of the chosen process temperature in the high pressure treatment. At T_0 = 301 K approx. 6 log and 5 log reduction of the viable cell counts can be observed in the upper and the lower probe respectively. With a 3 K temperature upshift of T_0 to 304 K, however, an increased inactivation of bacteria by approx. 1 log can be observed in every case. Furthermore, the tailing behavior of *L. lactis* under high pressure can be confirmed. This is obvious as longer pressure holding does not contribute to further reductions of viable cell counts at both process temperatures.

Table 17 : Reduction of viable cell counts of *L. lactis* after a high pressure treatment of probes with milk buffer at p* = 1.0 (500 MPa) at different temperatures

Viable cell counts		**Log(N/N_0) Upper probe**		**Log(N/N_0) Lower probe**	
		Simulation	**Experiment**	**Simulation**	**Experiment**
T_0 = 301 K	**t_t^* = 3.6**	-6.53	-6.06	-4.90	-5.05
	t_t^* = 5.2	-6.53	-6.18	-4.90	-6.03
T_0 = 304 K	**t_t^* = 3.6**	-7.66	-6.88	-6.64	-5.92
	t_t^* = 5.2	-7.66	-6.71	-6.64	-5.73
	t_t^* = 6.8	-7.66	-6.41	-6.64	-6.24

Furthermore, the reduction of stress resistant cell counts is also a subject of interest. By analyzing the stress resistant cell counts, the effects of the sublethal injury due to high pressure can be detected. As a result of the sublethal injury, bacteria enter a viable but non-growing state. The results shown in Table 18 indicate a reduction of stress resistant cell counts by 8 log in every probe.

Table 18 : Reduction of stress resistant counts of *L. lactis* after a high pressure treatment of probes with milk buffer p* = 1.0 (500 MPa) at different temperatures

Stress resistant cell counts		**Log(N/N$_0$) Upper probe**		**Log(N/N$_0$) Lower probe**	
		Simulation	**Experiment**	**Simulation**	**Experiment**
T$_0$ = 301 K	t_t^* **= 5.2**	-7.90	-8.19	-7.90	-7.58
	t_t^* **= 6.8**	-7.90	-8.19	-7.90	-8.19
T$_0$ = 304 K	t_t^* **= 3.6**	-7.90	-7.79	-7.90	-7.48
	t_t^* **= 5.2**	-7.90	-7.79	-7.90	-7.37
	t_t^* **= 6.8**	-7.90	-7.79	-7.90	-7.79

However, there are food products, in which additives such as salt and sugar are needed due to the processing aspects. Thus, it is not enough to study only the inactivation process in neutral media. Moreover, it has been reported that sugar and salt have baroprotective effects on microorganisms during the high pressure treatment. Thus, additional experiments and numerical simulations for foods with high sugar and salt concentrations are carried out.

4.3.3.2 Milk buffer with 1.5 M sucrose

The same experiments carried out in the last chapter are now repeated with a few modifications. By adding 1.5 M sucrose to the probes, which is considered the highest sucrose concentration found in food, less lethal and sublethal injury effects of *L. lactis* are observed even at higher temperatures. Thus, the chosen start temperatures of 311, 316 and 321 K are higher than those of the last section. Figure 64 shows the lethal and sublethal injury effects achieved in both probes after 1020 seconds (t_t^* = 6.8) of pressure treatment with p* = 1.0 (500 MPa) as the autoclave was tempered at 311 K. Here again, due to higher local temperature more cell injuries can be observed in the upper part of the autoclave. The maximum reduction of viable cells of approx. 2 log can be achieved in the upper probe at t_t^* = 6.8, whereas the sublethal injury effects of approx. 4 log can be observed in both probes. Additionally, longer pressure holding does not contribute to further reduction of viable cells either. Therefore, this "tailing" effect is proven for both physiological states with this additive in both the numerical and experimental results. It should also be mentioned that the deviation between the numerical and the experimental results at the beginning ($t_t^* = 0$) is due to the start value of the inactivation as suggested by the model of Kilimann [119], which includes the technical failures during the measurements.

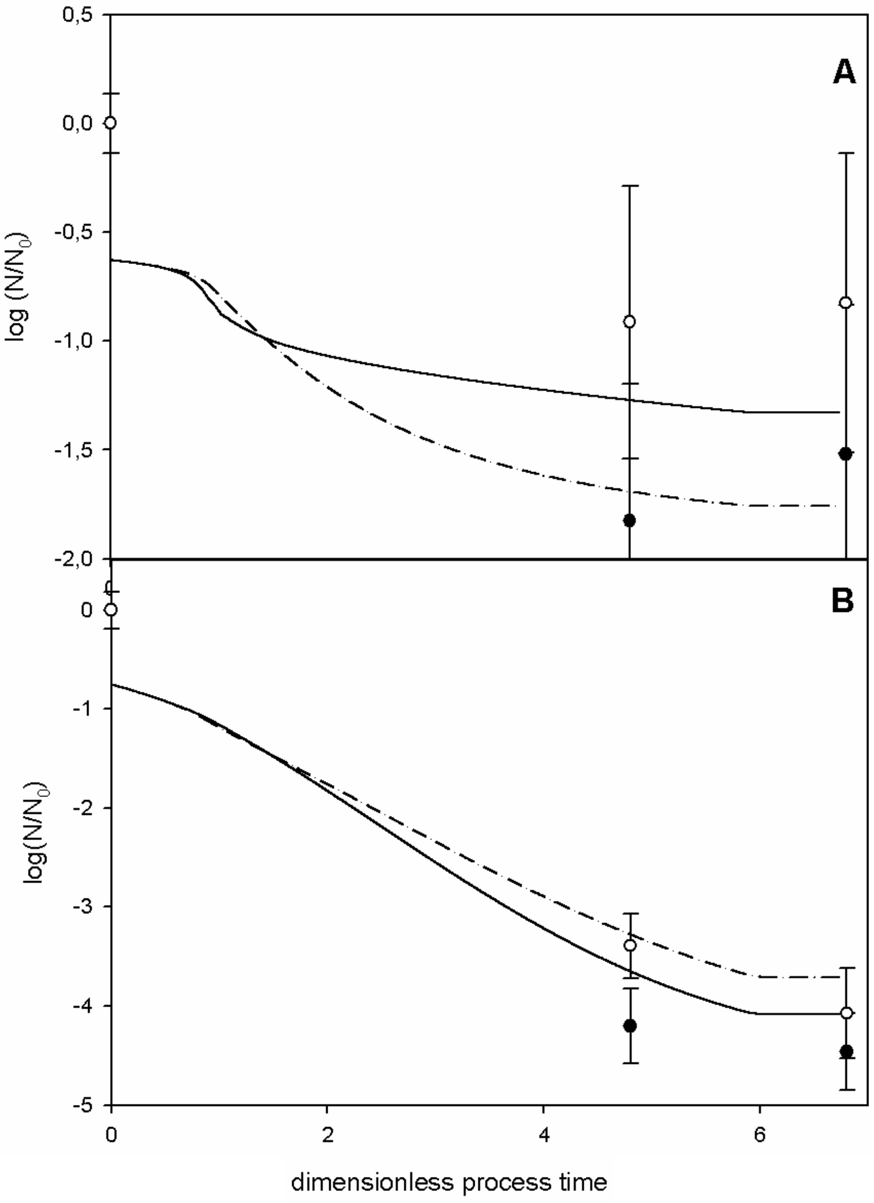

Figure 64: log(N/N$_0$) of *L. lactis* inside the PCR-tubes after $t_t^* = 6.8$ (1020 seconds) with 1.5 M sucrose as additive. The start temperature was set to $T_0 = 311$ K. (A: viable cell counts. B: stress resistant cell counts) Dotted and solid curves represent the calculated cell count

reduction of the upper and the lower probes respectively. The measured data are shown as (●) for the upper and (○) for the lower probe.

The complete results for the viable and the stress resistant cell counts are illustrated in Table 19 and Table 20 respectively. A close look at all the data in both tables reveals that less inactivation of *L. lactis* can be achieved at this high sucrose concentration of 1.5 M compared to the results with neutral media despite of the higher process temperatures used in this case. This finding confirms the existence of the tailing effect found during the high pressure treatment of microorganisms. However, this tailing can be eliminated at higher temperatures. For example, at 321 K the 5 log reduction for both viable and stress resistant cell counts can be achieved at t_t^* = 5.2 (780 seconds) at 500 MPa. However, it must also be denoted that the sucrose concentration used in this study is extremely high and can be found only in a few real food matrices. Thus, in real food with smaller sucrose concentrations, the baroprotective effects of sucrose must be smaller than shown here.

Table 19 : Reduction of viable counts of *L. lactis* after a high pressure treatment of probes with 1.5 M Sucrose p* = 1.0 (500 MPa) at different temperatures

Viable cell counts		**Log(N/N$_0$) Upper probe**		**Log(N/N$_0$) Lower probe**	
		Simulation	**Experiment**	**Simulation**	**Experiment**
T$_0$ = 311 K	t_t^* **= 5.2**	-1.74	-1.82	-1.30	-0.91
	t_t^* **= 6.8**	-1.74	-1.51	-1.30	-0.82
T$_0$ = 316 K	t_t^* **= 5.2**	-4.01	-3.63	-3.14	-3.34
	t_t^* **= 6.8**	-4.01	-4.14	-3.14	-3.37
T$_0$ = 321 K	t_t^* **= 3.6**	-5.76	-4.91	-5.24	-4.32
	t_t^* **= 5.2**	-5.76	-5.57	-5.24	-5.42

Table 20 : Reduction of stress resistant counts of *L. lactis* after a high pressure treatment of probes with 1.5 M Sucrose p* = 1.0 (500 MPa) at different temperatures

Stress resistant cell counts		**Log(N/N$_0$) Upper probe**		**Log(N/N$_0$) Lower probe**	
		Simulation	**Experiment**	**Simulation**	**Experiment**
T$_0$ = 311 K	t_t^* **= 5.2**	-4.00	-4.19	-3.60	-3.38
	t_t^* **= 6.8**	-4.00	-4.45	-3.60	-4.06
T$_0$ = 316 K	t_t^* **= 5.2**	-4.87	-5.42	-4.15	-5.03
	t_t^* **= 6.8**	-5.19	-5.57	-4.71	-5.11
T$_0$ = 321 K	t_t^* **= 3.6**	-6.00	-5.60	-4.95	-5.30
	t_t^* **= 5.2**	-6.00	-6.50	-5.11	-6.36

4.3.3.3 Milk buffer with 4 M NaCl

Similar to sucrose, NaCl also contributes to increased pressure resistance of bacteria. By adding NaCl to the buffer, bacteria becomes more resistant to higher pressures and, thus, less inactivation of *L. lactis* can be observed. Figure 65 shows the reduction of viable and stress resistant bacteria in both PCR-tubes after 1020 seconds of pressure treatment (t_t^* = 0.68) at p* = 1.0 (500 MPa) as the autoclave is tempered at 316 K. A maximum reduction of viable cell counts of approx. 3 - 5 log can be observed in the lower and the upper probes respectively. However, slightly more than 6 log of bacteria is sublethally injured in both probes.

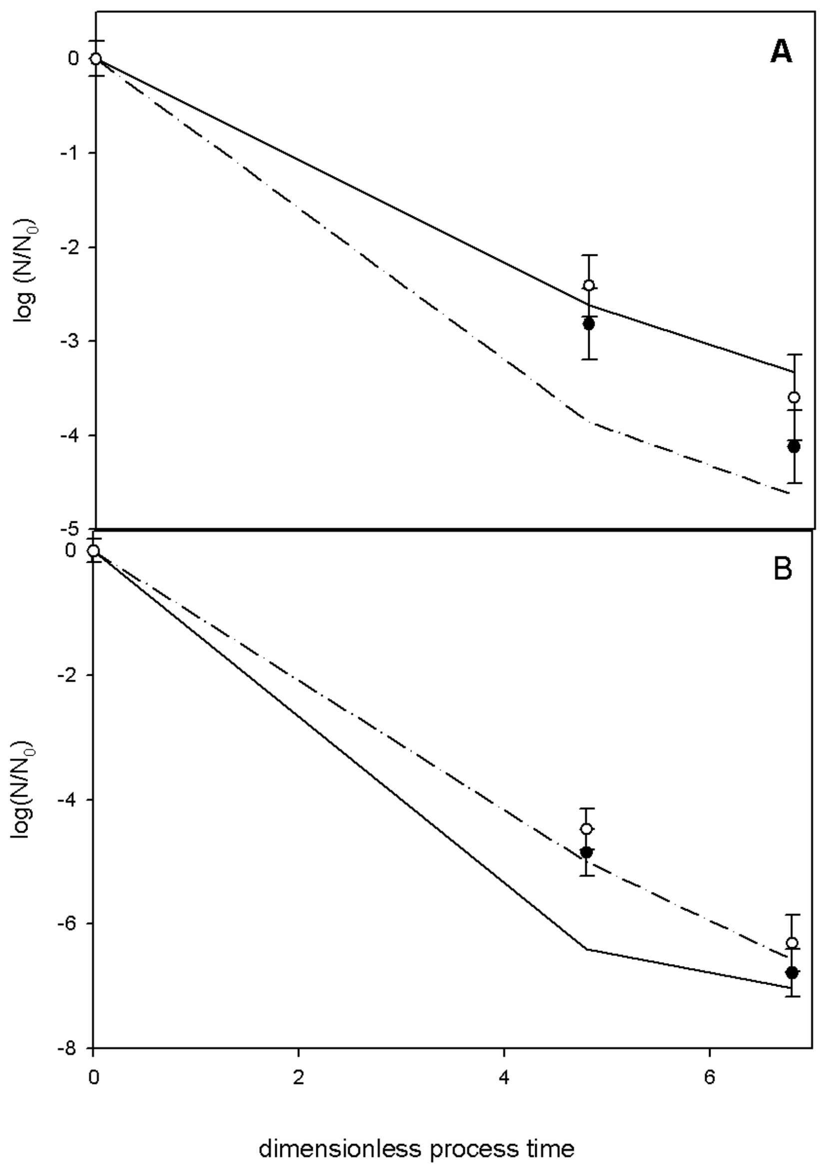

Figure 65: log(N/N$_0$) of *L. lactis* inside the PCR-tubes after t_t^* = 6.8 (1020 seconds) with 4.0 M NaCl as additive. The start temperature was set to T_0 = 316 K. (A: viable cell counts. B: stress resistant cell counts) Dotted and solid curves represent the calculated cell count reduction of the upper and the lower probes respectively. The measured data are shown as (●) for the upper and (○) for the lower probe.

At first glance, the results shown in Table 21 and Table 22 seem to be similar to those from the probes with 1.5 M Sucrose, as less cells can be inactivated compared to the case with neutral media. However, there is a little difference here. It must be mentioned that at t_t^* = 6.8 the tail is not observed as yet, as further reductions of both viable and stress resistant cell counts can still be achieved with increased pressure holding time. Overall, all these data indicate strong baroprotective properties of NaCl that protects the cells so that fewer cells can be inactivated. To eliminate this baroprotection, longer pressure holding and higher temperatures than shown in in Table 21 and Table 22 must be chosen.

Table 21 : Reduction of viable counts of *L. lactis* after a high pressure treatment of probes with 1.5 M Sucrose p* = 1.0 (500 MPa) at different temperatures

Viable cell counts		**$\log(N/N_0)$ Upper probe**		**$\log(N/N_0)$ Lower probe**	
		Simulation	**Experiment**	**Simulation**	**Experiment**
T_0 = 311 K	**t_t^* = 5.2**	-2.10	-2.64	-1.92	-1.94
	t_t^* = 6.8	-2.27	-2.58	-2.10	-2.07
T_0 = 316 K	**t_t^* = 5.2**	-3.85	-2.82	-2.62	-2.41
	t_t^* = 6.8	-4.64	-4.12	-3.33	-3.60
T_0 = 321 K	**t_t^* = 3.6**	-2.29	-1.46	-1.74	-0.89
	t_t^* = 5.2	-3.29	-3.42	-2.36	-2.71

Table 22 : Reduction of stress resistant counts of *L. lactis* after a high pressure treatment of probes with 1.5 M Sucrose p* = 1.0 (500 MPa) at different temperatures

Stress resistant cell counts		**Log(N/N_0) Upper probe**		**Log(N/N_0) Lower probe**	
		Simulation	**Experiment**	**Simulation**	**Experiment**
T_0 = 311 K	t_t^* **= 5.2**	-5.16	-4.12	-3.59	-3.44
	t_t^* **= 6.8**	-5.47	-5.37	-4.22	-4.90
T_0 = 316 K	t_t^* **= 5.2**	-6.41	-4.84	-5.00	-4.47
	t_t^* **= 6.8**	-7.03	-6.78	-6.57	-6.30
T_0 = 321 K	t_t^* **= 3.6**	-5.16	-3.66	-3.52	-3.91
	t_t^* **= 5.2**	-5.94	-6.11	-4.53	-6.21

4.3.3.4 Comparison of predicted data and experimental results

In general, results achieved in the 3.3-liter-pressure-autoclave at two different locations comprise spatiotemporal heterogenities on the temperature- and inactivation-distribution of the bacteria due to the process. A maximum of 2-Δ-log between the upper and the lower probes could be obtained by both the experiments and the numerical simulations. Furthermore, very good agreement between the experimental and numerical results could be obtained (Figure 66).

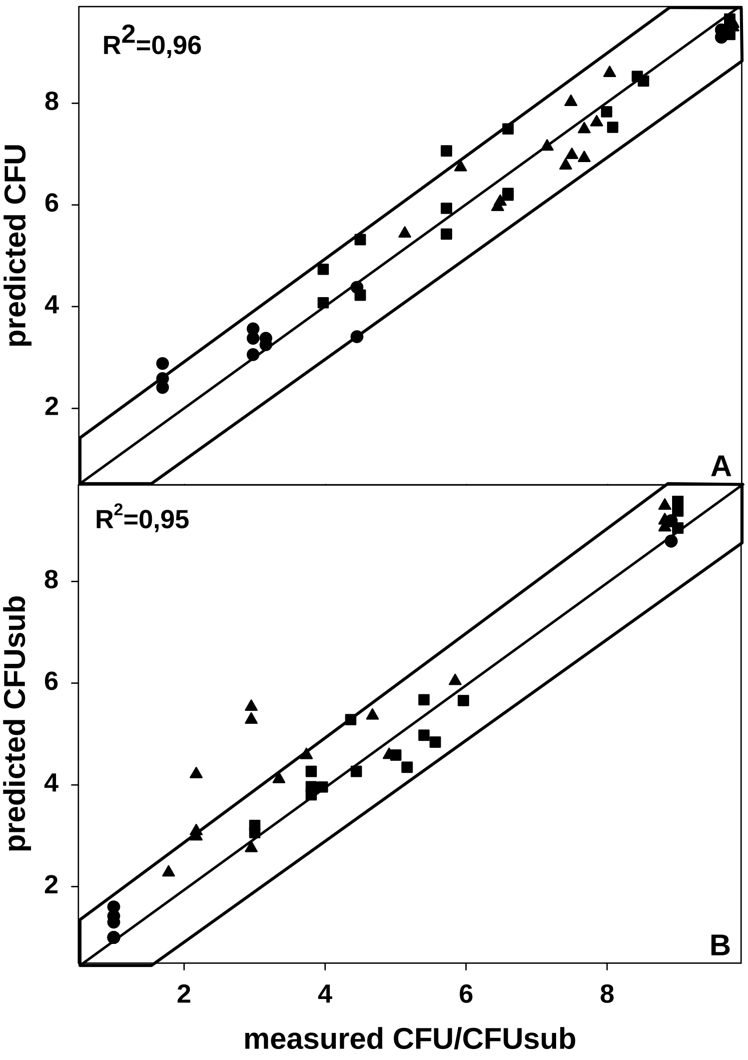

Figure 66: Comparison of predicted data and data measured for model validation after model establishment. Framed areas indicate the deviation explained by the overall experimental error of the methods for determination of CFU and CFUsub. Symbols represent data for the measurands in milk buffer (●), milk buffer sucrose (■), and milk buffer NaCl (▲). A: cell counts (CFU). B: stress resistant cell counts (CFUsub).

The hybrid of the modelling of the inactivation kinetics and the numerical techniques used in the simulations has proven to be efficient and highly accurate in predicting the inactivation kinetics of microorganisms. Despite the generally high margin of errors in the microbiological analysis techniques, which can be as high as 1 log cell counts, the regression rates of higher than 0.95 could be achieved. Thus, this hybrid approach is an interesting approach that should be considered in designing the high pressure treatments in real industrial applications.

Concerning the heterogeneity of the inactivation process, the results of both the experiments and numerical simulations indicate non-uniformities of the high pressure inactivation processes. In many cases, as high as 2 log differences of the viable and stress resistant cell counts can be observed. Not sufficient treatments of product can lead to partially contaminated products. This is where the industrial design will play a vital role. It will be important in industrial high pressure treatment of food to find the proper process parameters to achieve sufficient inactivation of microorganisms or other contaminations while trying not to expose the treated food to unnecessarily long pressure holding in order to reduce the structural damages of food and to reduce the production costs.

5 CONCLUSION

High pressure technology is becoming an interesting alternative to conventional thermal treatments of food thanks to its ability to avoid off-flavor and deterioration of food components and nutrients, to produce unique texture on food, and to save total amounts of energy required for food processing. With such growing interests from both the consumers and the industry, the high pressure research activity is one of the most interesting research fields in biotechnology. Most of the researches deal with structural or molecular changes of food structure, inactivation of food contaminations or with the ability to use high pressure to produce other innovative products. Such researches are carried out in lab-scale high pressure autoclaves, which are relatively small in size, mostly too small for real industrial applications.

In order to make the high pressure technology suitable, applicable and affordable for the food industry, high pressure autoclaves must gain in size in order to handle larger batches. Nowadays, there are high pressure autoclaves, which are as large as 500 liter, and the limit seems not to be reached yet. Thanks to techniques used in the autoclave engineering, i.e. “autofrettage” or “heat-shrink technique”, it is possible to design larger autoclaves with working pressure levels in the GPa range. With the size of the autoclaves growing, it becomes difficult to control the high pressure process inside such autoclaves. In particular, the non-uniformity of the process is one of the biggest concerns in industrial high pressure applications.

Especially the thermal heterogeneity can have strong influences on the uniformity of the product quality, since most of the high-pressure kinetics is also temperature dependent. With the size of the autoclaves growing, it becomes impossible to guarantee the thermal homogeneity at every single point in the autoclave. Although most of the high pressure autoclaves have tempering units installed at their outer walls, but as shown in this work, tempering units alone are not sufficient to control the thermofluiddynamical processes inside the autoclave. Therefore, fundamental knowledge concerning the thermofluiddynamical behaviors during the high pressure treatment must be gathered in order to understand the process non-uniformity during the high pressure treatment.

By governing thermodynamic equations of mass, momentum and energy conservation, the first impressions of the thermofluiddynamical processes occurring during the high pressure treatment can be obtained. Furthermore, by considering the dimensionless thermodynamic equations of the high pressure treatment, the contribution and the importance of each sub-process of the fluid motion can be understood.

Firstly, all the terms with the Eckert number contribute only little to the whole thermofluiddynamical processes. This is due to the relatively small velocities found in this study case. This means that in cases with such low velocities, the terms with the Eckert number can be neglected, so that huge computational costs can be saved. In fluiddynamical aspects, small Eckert numbers mean small dissipation effects. It could be shown that the dissipation effects do not play an important role in the high pressure applications. To reach 10 % dissipation effects ($Ec \approx 0.1$), the pressure medium “water” must penetrate the chamber at a speed of approx. 500 m/s, which is by far not possible with available machineries. Therefore, the temperature increase during the high pressure treatment is due to thermal expansion effects solely, as dissipation does not play a noteworthy role during the high pressure treatment.

It could also be shown that different pressure ramps cause different flow behaviors during the compression and the pressure holding phase. Steeper pressure ramps with high velocities cause turbulent inflow conditions. Although the critical Reynolds number of free jet under such high pressures is not known yet, it is assumed to be very small. First instabilities in incompressible jet flows can occur at Reynolds numbers as low as 33 [111]. Furthermore, different momentum of the free jet also causes different flow behavior in the chamber itself. The momentum flux of the jet interacts with the free convective motion due to the temperature gradients of the fluid inside the autoclave, so that different flow regimes exist. As a result of this, many vortices can be seen in several regions of the autoclave during the compression phase.

During the pressure holding phase, however, as no forced convection takes place and free convection dominates, a downward-directed fluid motion at the vertical wall of the autoclave can be observed in every case. The large Grashof and Rayleigh numbers show that the buoyant force dominates. However, as both vertical and horizontal temperature gradients exist, free convection always occur. Additional larger vortices can also be seen at the upper wall of the autoclave. However, as more heat is removed by the cold wall, temperature gradients gradually become insignificant. As buoyancy forces, which dominate the pressure holding phase, become weaker, the strength of the vortices is reduced and some of the vortices disappear finally.

The comparison of the reference case with the same simulation under compensated gravity condition could illustrate the effects of free convection. It could be observed that the gravitational forces represent the largest terms in the equations and that free convection acts positively on the homogeneity of the temperature distribution and the product due to additional movements caused by buoyancy forces. Recently, there have been proposals to use high pressure vessels in space stations. Therefore, it must be kept in mind, that there will be many differences between the high pressure processes on earth and in space, as the lack of the gravitational forces will change the results greatly.

The size of the autoclave also seems to be very important considering the homogeneity of the product. In lab-scale autoclaves, the cooling devices can act at its maximum. In very large autoclaves, on the contrary, thermal expansion dominates the whole autoclave. In these two cases, temperature gradients are not significant, and the product uniformity is acceptable. In medium-sized autoclaves, however, neither the cooling process nor the thermal expansion can dominate the process and temperature gradients occur, leading to heterogeneity of the product quality. In such cases, an easy solution to maximise the effectiveness and minimise the risks due to non-uniformed product quality can be made by installing a heat damping layer at the inner wall of the autoclave. It could be shown that heat damping cuts down up to 60 % of the process duration if the same level of product should be obtained, and that the heterogeneity can be reduced down to less than 1 %. In this work, a model to approximate the effects of the temperature gradients was introduced, and can be used to approximate the heterogeneity of the product quality. Although the effects of free convection are not considered in this analytical model, it could show that the risks of potentially non-uniform treatments of food are the highest in the middle-sized autoclaves. Furthermore, the use of horizontal autoclaves reduces the heterogeneity of the product only a little (about 0.3 % difference) but reaches the same effectiveness as vertical ones.

Moreover, the thermally induced non-uniformity of the inactivation process of microorganisms is also studied. For this part, experiments and the modelling of the inactivation kinetics of *L. lactis* under high pressure were carried out by Dr..-Ing. Kilimann. Both the experimental and the numerical results indicate extreme non-uniformity of the inactivation process of the mentioned microorganisms. Overall, the inactivation kinetics of *L.*

lactis in 3 different food-like matrices at 500 MPa is studied: neutral medium, high sucrose concentration and high NaCl concentration. In all the cases, non-uniformity of up to 2 log differences between the probes in the upper part and the lower part of the autoclave can be observed. This is due to the temperature gradients existing throughout the entire pressure treatment. Because the temperature in the upper part of the autoclave is always higher than in the lower part, more inactivation of *L. lactis* is observed here. Moreover, the baroprotectivity of the additives sucrose and NaCl and the tailing effect of bacteria in high pressure treatment in a medium-scale high pressure autoclave are confirmed. The mentioned additives protect *L. lactis* against the inactivation effects of high pressure at 500 MPa. However, these baroprotective behaviours of sucrose and NaCl can be eliminated at higher temperatures. Therefore, it is of great importance to choose the proper process temperature for the high pressure processing, so that the food safety can be assured, especially when it comes to inactivation of contaminating or toxic microorganisms, where the legally enforced 5D concept must be applied. An example for the spatial distribution of the concentration of stress resistant cells in the chamber after 4 minutes of pressure treatment is illustrated in Figure 67.

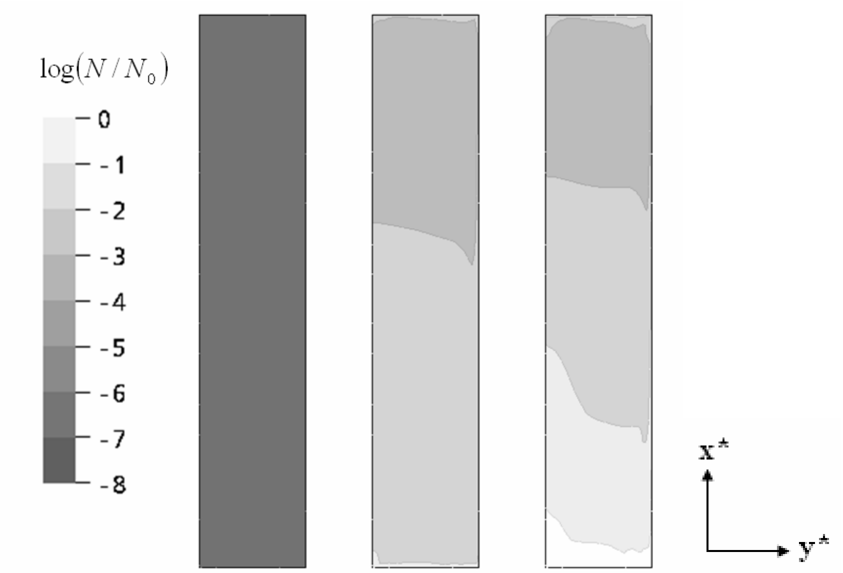

Figure 67 : Distributions of stress resistant cell counts ($\log(N/N_0)$) of *L. lactis* after 4 min of application of 500 MPa using milk buffer at 304 K, milk buffer with 1.5 M sucrose at 316 K and milk buffer with 4 M NaCl at 316 K from left to right respectively.

In case of milk buffer, an almost homogeneous distribution of stress resistant cells and a reduction by eight decimal powers of *L. lactis* can be observed even at relatively mild treatment conditions (Figure 67 left).

In the presence of baroprotectants, the distribution becomes heterogeneous and the efficiency of the inactivation process is reduced. In case of the addition of sucrose, the maximum difference in the concentration of stress resistant cell counts between the upper part and the bottom amounts up to one decimal power. Note that the process with sucrose containing buffer yields only a reduction of three to four decimal powers instead of eight when pure milk buffer is used as medium.

With addition of sodium chloride into the buffer, also here a maximum reduction of three to four decimal powers can be observed. Additionally, the non-uniformity in the cell count distribution is much larger. The largest difference between maximum and minimum inactivation levels adopts values between two and three decimal powers. This range is extreme for a high-pressure pasteurisation and reveals the potential risk that even a slight modification of the chemical composition of the food system bears.

The objective of experimentally and numerically investigating the non-uniformity of the inactivation process of *L. lactis* is achieved successfully. The hybrid technique used in this work delivers highly accurate predictions of the inactivation process of microorganisms. The regression rates of higher than 0.95 is excellent for such microbiological problems. While an excellent agreement between measured and calculated temperatures is found in the upper part of the autoclave, the simulation underestimates the data in the lower part of the autoclave. This underestimation can be due to the assumption of a constant temperature at the inlet of the autoclave, which may not be completely justified. Since the fluid is compressed in the inlet vane it should adopt a higher temperature. Measurements of the inlet temperature showed out to be difficult due to strong hydrodynamic interaction between the thermocouple and the fluid. An additional limitation of the theoretical approach is coupled to the fact, that the microbial samples are immobilized in plastic tubes. The simulation can not account for this temperature barrier and assumes instantaneous temperature equilibrium between the pressure medium around the sample and the bacteria suspension inside the sample. In reality there is a delay in the equilibration between temperatures inside and outside of the sample due to thermal inertia. Further refinement of the modelling techniques in both, microbiological and thermo-fluiddynamical aspects must remain subject to future work. Especially, fat containing food systems are challenging due to the stronger temperature increase during compression and delayed thermal equilibration due to higher viscosity compared to watery solutions. Further, packed food should be taken into account. In this case, heat transfer between food, package material and pressure medium could deliver further insight into control and safety of high-pressure bacteria inactivation.

Numerical simulations proved to be an effective tools for studying both the thermofluiddynamical processes and the biotechnological aspects of the high pressure technology. In this work, it could be proven that the hybrid of CFD and other modelling technniques delivers high potential to predict the biotechnological subprocesses during the high pressure treatment with extremely high precision. Therefore, the use of CFD-hybrid in the research field of the high pressure technology should be maintained and further developed. Besides the processes shown in this work, there are many other applications of high pressure, which can also be studied with such CFD-hybrid. For example, the non-uniformity of the phase changing process of water or of the denaturation process of proteins under high pressure are interesting aspects of the high pressure technology, which can be explained using such CFD-hybrid also. It is also possible to predict inactivation of microorganisms in the indirect pressure treatment of packed foods with the fluid structure interaction techniques. In order to do this, the finite volume code for the fluid movement must be coupled with the finite element code for the deformation of the packages.

For high pressure systems with pistons, although no free jet would occur, it might be possible that the flow inside the autoclave becomes turbulent, if the piston moves fast enough. Such autoclaves with pistons are planned to be used in “short time ultra high pressure” applications, in which the target pressure can be built up within a few seconds. With such configuration, the adiabatic temperature can be reached throughout the autoclave, which could maximise the effectiveness of the high pressure process. However, with proceeding process time more heat is removed by the wall and free convection occurs. This is somewhat similar to what could be shown in this work. However, as the temperature is higher, somewhat larger velocities and Grashof and Rayleigh numbers are awaited.

The possibility to use polymers, which become warmer than the pressure fluid under high pressure, as so called “hot spots” [33] must also be studied. With such process configuration, adiabatic temperature increased can be assured throughout the autoclave. However, studies must be carried out in many aspects such as the techniques of how to utilize such hot spots or if the polymer is changed in its substances. The food safety must also be considered. Overall, it could be concluded that the thermofluiddynamical processes during the high pressure treatment are subject to chosen boundary conditions. Therefore, no autoclave is the same. Further studies to generalize the characteristics of the processes in high pressure autoclaves must be carried out. Some attempts shown in this work should act as a basis for such further studies.

In the short future it will be possible to observe thermofluiddynamical processes during high pressure treatment in medium-sized autoclaves in-situ. At the same institute, a 2-liter high pressure autoclave with optical measuring systems is being engineered. Together with the liquid crystal techniques introduced in [36], it will be possible to observe process heterogeneity in a medium-scale high pressure autoclave. Also the inactivation process during the direct treatment of liquid food can be observed in-situ. There are liquid crystals, which reflect against light with different colors depending on the residual activity of the given enzymes. This will enable the first validation of the results shown here in this work. Also the presence of the turbulence can be observed with additional laser-doppler anemometry devices.

Overall, the study of the non-uniformity of the high pressure treatment is a very important issue for the high pressure food industry. Only when the process non-uniformity can be fully controlled, only then high pressure treated food will become absolutely safe for the consumers.

6 APPENDIX

In order to provide better understanding of the mathematical equations used in this thesis, the basic notation used throughout this PhD work must be explained. First of all, the gradient operator ∇ is defined as:

$$\nabla = \left(\frac{\partial}{\partial \mathrm{x}}, \frac{\partial}{\partial \mathrm{y}}, \frac{\partial}{\partial \mathrm{z}} \right) \tag{6.1}$$

For a general scalar $\phi(x, y, z)$ the gradient of ϕ can be defined as

$$\nabla \phi = \left(\frac{\partial \phi}{\partial x}, \frac{\partial \phi}{\partial y}, \frac{\partial \phi}{\partial z} \right) \tag{6.2}$$

for a vector $\vec{W}(x, y, z)$ with the components $W_{x,}\ W_y, W_z$ in the x-, y- and z-direction respectively. The divergence of the vector $\vec{W}$ is defined by

$$\nabla \bullet \vec{W} = \left(\frac{\partial W_x}{\partial x} + \frac{\partial W_y}{\partial y} + \frac{\partial W_z}{\partial z} \right). \tag{6.3}$$

The tensor product of two vector spaces $\vec{W}$ and $\vec{V}$, denoted $\vec{W} \otimes \vec{V}$ and also called the tensor direct product, is a formal bilinear multiplication of two vector spaces. The direct tensor product $\vec{W} \otimes \vec{V}$ is defined as:

$$\vec{W} \otimes \vec{V} = \begin{bmatrix} W_x V_x & W_x V_y & W_x V_z \\ W_y V_x & W_y V_y & W_y V_z \\ W_z V_x & W_z V_y & W_z V_z \end{bmatrix}. \tag{6.4}$$

Using specific tensor notation the equations relating to each dimension can be combined in a single equation, i. e.:

$$\nabla \bullet \rho\left(\vec{W} \otimes \vec{V}\right) = \begin{bmatrix} \frac{\partial}{\partial x}(\rho W_x V_x) + \frac{\partial}{\partial x}\left(\rho W_x V_y\right) + \frac{\partial}{\partial x}(\rho W_x V_z) \\ + \frac{\partial}{\partial x}\left(\rho W_y V_x\right) + \frac{\partial}{\partial x}\left(\rho W_y V_y\right) + \frac{\partial}{\partial x}\left(\rho W_y V_z\right) \\ + \frac{\partial}{\partial x}\left(\rho W_z V_x\right) + \frac{\partial}{\partial x}\left(\rho W_z V_y\right) + \frac{\partial}{\partial x}\left(\rho W_z V_z\right) \end{bmatrix}, \tag{6.5}$$

where ρ represents the density. The transpose of a matrix is defined by the operator^T. For instance, if the matrix is defined by

$$\nabla \phi = \begin{bmatrix} \frac{\partial \phi}{\partial x} \\ \frac{\partial \phi}{\partial y} \\ \frac{\partial \phi}{\partial z} \end{bmatrix}, \tag{6.6}$$

$$[\nabla \phi]^T = \begin{bmatrix} \frac{\partial \phi}{\partial x} & \frac{\partial \phi}{\partial y} & \frac{\partial \phi}{\partial z} \end{bmatrix}. \tag{6.7}$$

Last but not least, the unit matrix is defined as

$$\delta = \begin{bmatrix} 1 & 0 & 0 \\ 0 & 1 & 0 \\ 0 & 0 & 1 \end{bmatrix}. \tag{6.8}$$

7 BIBLIOGRAPHY

[1] Suzuki A., 2002. High pressure-processed foods in Japan and the world. Trends in High Pressure Bioscience and Biotechnology (ed. R. Hayashi), Elsevier Science, Amsterdam

[2] Hite, B. H. 1899. The effect of pressure in the presentation of milk, West Virginia Agricultural Experiment Station, Morgantown, Bulletin 58, 15-35.

[3] Bridgman, P. W. 1914. The coagulation of albumen by pressure, J. Biol. Chem., 19, 511-512.

[4] Bridgman, P. W. 1923. The thermal conductivity of liquids under pressure, Proc. Am. Acad. Arts. Sci., 59, 141-169.

[5] Knorr, D. 1996. Advantages, opportunities and challenges of high hydrostatic pressure application to food systems, Proceedings of the International Conference on High Pressure Bioscience and Biotechnology, Kyoto, Japan, Ed.: Hayashi, R., Balny, C., High Pressure Bioscience and Biotechnology, 279-287.

[6] Lambert, Y., Demazeau, G., Largeteau, A., Bouvier, J. M., Laborde-Croubit, S., Cabannes, M. 2000. Packing for high-pressure treatments in the food industry, Packing Technology and Science, 13, 63-71.

[7] Harte, F., Amonte, M., Luedecke, L., Swanson, B. G., Barbosa-Cánovas, G. V. 2002. Yield stress and microstructure of set yogurt made from high hydrostatic pressure-treated full fat milk, Journal of Food Science, 67, 2245-2250.

[8] Baars A, Kulisiewicz L, Gebhardt R, Doster W, Delgado A. 2006. Viscosity and Aggregation of ß-Lactoglobulin under High Pressure. Proc. 4th Int. Symp. Food Rheology and Structure, 19.-23.2.2006, Zurich.

[9] Baars A, Marjanovic D, Delgado A. 2004. Relations of diffusive momentum transport and conformational changes in aqueous beta-lactoglobulin solutions under high pressure. 3rd International Conferences on High Pressure Bioscience and Biotechnology, 27.-30.9.2004, Rio de Janeiro, Brazil.

[10] Bridgman, P. W. 1912. Water in the liquid and five solid forms under pressure, Proceedings of the American Academy of Arts and Sciences, 47, 439-558.

[11] Le Bail, A., Chevalier, D., Mussa, D. M., Ghoul, M. 2002. High pressure freezing and thawing of foods, a review, International Journal of Refridgeration, 25, 504-513.

[12]Özmutlu Ö., Hartmann C., Delgado A. 2003. Visualization of Temperature and Velocity Fields during Phase Change of Water under High Hydrostatic Pressure, GALA 2003- Laser Methods in Fluid Mechanics, 9-11 September 2003, Braunschweig, Germany.

[13]Ferstl P, Baars A, Özmutlu Ö, Hartmann C, Delgado A. 2005. Momentum and Energy Transfer During Phase Change of Water under High Hydrostatic Pressure, Gesellschaft für Angewandte Mathematik und Mechanik (GAMM), Luxembourg, Proceedings in Applied Mathematics and Mechanics (PAMM), WILEY-VCH Verlag Weinheim, 5(1), 595-596.

[14] Masson, P., Tonello, C., Balny, C. 2001. High-pressure biotechnology in medicine and pharmaceutical science: review article, Journal of Biomedicine and Biotechnology 1(2), 85-88.

[15] Silva, J. L., Foguel, D., Da Poian, A. T., Pevelige, P. E. 1996. The use of hydrostatic pressure as a tool to study viruses and other macromolecular assemblages, Current Opin. Struct. Biol., 6, 166-175.

[16] Silva, C., Giongo, V., Simpson, A., Camargos, E., Silva, J.L., and Koury, M., 2001. Effects of hydrostatic pressure on a membrane-enveloped virus: high immunogenicity of the pressure-inactivated virus. J Virol, 66, 4, 2111-7.

[17] Silva, J.L. and Weber, G., 1988. Pressure-induced dissociation of brome mosaic virus. J Mol Biol, 199, 1, 149-59.

[18] Jurkiewicz, E., Villas-Boas, M., Silva, J. L., Weber, G., Hunsmann, G., Clegg, R. M. 1995, Inactivation of simian immunodefficiency virus by hydrostatic pressure, Proc. Natl. Acad. Sci.USA, 92, 6935-6937.

[19] Perche, P. Y., Cléry, C., Bouloy, M., Burkhart, M. F., Masson, P., Michel, P. 1997. Study of inactivation and immunogenicity of Rift valley fever virus type 13 clone treated by high hydrostatic pressure, Am. J. Trop. Med. Hyg., 57(3S), 256-257.

[20] Korn, A., Frey, B., Sheriff, A., Gaipl, U. S., Franz, S., Meyer-Pittroff, R., Herrmann, M., Bluemelhuber, G. 2004. High hydrostatic pressure inactivated human tumour cells preserve their immunologenicity, Cellular and Molecular Biology, 50(4), 469-477.

[21] Silva, J.L., Foguel, D., and Royer, C.A., 2001. Pressure provides new insights into protein folding, dynamics and structure. Trends in Biochemical Sciences, 26(10),612-618.

[22] Smelt, J.P.P.M., 1998. Recent advances in the microbiology of high pressure processing, Trends in Food Science & Technology, 9, 152-158.

[23] Hinrichs, J. 2000. Ultrahochdruckbehandlung von Lebensmitteln mit Schwerpunkt Milch und Milchprodukte-Phänomene, Kinetik und Methodik-Fortschritt-Berichte VDI, Reihe 3, Nr. 656, Düsseldorf: VDI.

[24] Ananta, E. Heinz, V., Schlueter, O., Knorr, D. 2001. Kinetic studies on high pressure inactivation of Bacillus stearothermophilus spores suspended in food matrices. Innovative Food Science and Emerging Technology, 2, 261-272.

[25] Gänzle, M. G., Ulmer, H. M., Vogel, R. F. 2001. High Pressure inactivation of Lactobacillus plantarum in a model beer system, J. Food Sci., 66, 1174-1181.

[26] Gänzle, M. G. , Vogel, R. F. 2001. Online-Fluorescent determination of pressure mediated outer membrane damage in Escherichia coli, Systematic and Applied Microbiology, 24, 477-485.

[27] Indrawati, I., Ludikhuyze, L. R., Van Loey, A. M., Hendrickx, M. E. 2000. Lipoxygenase inactivation in green beans (Phaseolus vulgaris L.) due to high pressure treatment at subzero and elevated temperatures, J. Agricult. Food. Chem., 48(5), 1850-1859.

[28] Fachin, D., Van Loey, A., Indrawati, A., Ludikhuyze, L., Hendrickx, M. 2002. Thermal and high-pressure inactivation of tomato polygalacturonase: A kinetic study, Journal of Food Science, 67, 1610-1615.

[29] Ludikhuyze, L., Van den Broeck, I., Weemaes, Hendrickx, M. E., et al. 1997. Kinetic parameters for temperature-pressure inactivation of Bacillus subtilis α-amylase under dynamic conditions, Biotechnology Progress, 13, 617-623.

[30] Ludikhuyze, L. Van den Broeck, I., Weemaes, C. A., Heremanns, C. H. , Van Impe, J. F., & Hendrickx, M. E., et al. 1997. Kinetics for isobaric-isothermal inactivation of Bacillus subtilis α-amylase, Biotechnology Progress, 13, 532-538.

[31] Denys, S., Ludikhuyze, L., Van Loey, A. M., Hendrickx, M. E. 1999. Modelling conductive heat transfer and process uniformity during batch high-pressure processing of foods. In H. Ludwig (Ed.), Trends in high pressure bioscience and biotechnology (pp. 381-384). Berlin: Springer.

[32] Denys, S., Van Loey, A. M., Hendrickx, M. E. 2000. A modelling approach for evaluating process uniformity during batch high hydrostatic pressure processing: combination of a numerical heat transfer model and enzyme inactivation kinetics, Innovative Food Science and Emerging Technologies, 1, 5-19.

[33] Delgado, A., Hartmann, C. 2000. Pressure treatment of food: instantaneous but not homogeneous effect, Proceedings of the 2nd International Conference on High Pressure Bioscience and Biotechnology Dortmund, 459-464.

[34]Delgado A, Özmutlu Ö, Hartmann C, Baars A. 2004. Optical diagnosis systems for measuring thermofluiddynamical phenomena in liquid biosystems under ultra high pressure. Proc. ICTAM 15.-21.8.2004. Warsaw, Poland.

[35]Kowalczyk W., Ferstl P., Baars A., Delgado A. 2005. *Vortrag*: Impuls- und Wärmeaustausch beim Phasenübergang unter Hochdruck, 3. Statusseminar: Hochdrucklebensmitteltechnologie und –bioverfahrenstechnik, 19.-20.9.2005, Freising.

[36] Pehl, M. PhD thesis, TU München

[37] Pehl, M., Delgado, A., 1999. An in situ Technique to visualize temperature and velocity fields in liquid biotechnological substances at high-pressure. In H. Ludwig (Ed.), Advances in high-pressure Bioscience and Biotechnology, (pp. 519-522). Heidelberg: Springer.

[38] Pehl, M., Werner, F., Delgado, A., 2000. First visualisation of temperature fields in liquids at high-pressure using thermochromic liquid crystals, Experiments in Fluids, 29(3), 302-304.

[39] Pehl, M., Delgado, A., 2002. Experimental investigation on thermofluiddynamical processes in pressurized substances. In R. Hayashi (Ed.), Trends in high pressure bioscience and biotechnology, (pp. 429-435). Amsterdam: Elsevier.

[40] De Heij, W. B. C., Van Schepdel, L. J. M. M., Moezelaar, R., Hoogland, H., Matser, A. M., Van den Berg, R. W. 2003. High Pressure Sterilization: Maximizing the Benefits of Adiabatic Heating, Food Technology, 57(3), 37-41.

[41] Hartmann, C., Delgado, A. 2004. Numerical simulation ofthe mechanics of a yeast cell under high hydrostatic pressure, Journal of Biomechanics, 37, 977-987

[42] Otero, L., Molina Garcia, A. D., Sanz, P. D. 2000. Thermal effects in foods during quasi-adiabatic pressure treatments, Innovative Food Science & Technology, 1, 119-126.

[43] Otero, L., Molina, A. D., Sanz, P. D. 2002. Thermal control simulation in high pressure treatment of foods, High Pressure Research, 22, 627-631.

[44] Schuhholz, J. 2003. Experimental and numerical investigation of temperature heterogeneities in a 3-liter high pressure chamber, Diplomarbeit, TU München

[45] Hartmann, C. 2002. Numerical simulation of thermodynamic and fluiddynamic processes during the high pressure treatment of fluid food systems, Innovative Food Science and Emerging Technologies, 3, 11-18.

[46] Hartmann, C., Delgado, A. 2002. Numerical simulation of convective and diffusive transport effects on a high-pressure-induced inactivation process, Biotechnology and Bioengineering, 79, 94-104.

[47] Hartmann, C., Delgado, A. 2003. Convective and diffusive transport effects in a high-pressure-induced inactivation process of packed food, International Journal of Food Engineering, 59(1), 33-34.

[48] Hartmann, C., Delgado, A. 2003. On the influence of transport effects on the high pressure induced inactivation in packed substances, Biotechnology and Bioengineering, 82(6), 725-735.

[49] Hartmann, C., Schuhholz, J.-P., Kitsubun, P., Chapleau, N., Le Bail, A., Delgado, A. 2004. Experimental and numerical analysis of the thermofluiddynamics in a high-pressure autoclave, Innovative Food Science and Emerging Technologies, 5, 399-411.

[50] Rademacher, B. 1999. Hochdruckbehandlung von Milch-Untersuchung zur Inaktivierung von Mikroorganismen und Enzymen und deren kinetische Beschreibung, Fortschritt-Berichte VDI Reihe 14, Nr. 96, Düsseldorf: VDI.

[51] Kowalczyk, W., Hartmann, C., Delgado, A. 2003. Modelling and numerical simulation of pressure induced phase changes of a fluid food system, Proceedings of the 2nd International Conference on High Pressure Bioscience and Biotechnology, Advances in High Pressure Bioscience and Biotechnology, Ed.: Winter, R., Dortmund, 465-469.

[52] Kowalczyk, W., Hartmann, C., Delgado, A. 2004. Freezing and Thawing at the high hydrostatic pressure conditions – modelling and numerical simulation, Proceedings in Applied Mathematics and Mechanics, GAMM 2003, Wiley-VCH Verlag Weinheim,3, 388-389.

[53] Kowalczyk, W., Hartmann, C., Delgado, A. 2004. Modelling and numerical simulation of convection driven high pressure induced phase changes, International Journal of Heat and Mass Transfer, 47(5), 1079-1089.

[54] Kowalczyk, W. 2004. Numerische Simulation von Fest-Flüssig-Phasenübergängen bei der Hochdruckbehandlung, PhD Thesis, TU München.

[55] Eder, C., Delgado, A., Golbach, M., Eggers, R. 2003. Interferometrische in-situ Densitometrie fluider hochkomprimierter Lebensmittel. Proceedings der 11. Fachtagung „Lasermethoden in der Strömungsmesstechnik“ GALA 2003, Beitrag 29, Braunschweig, 09.-11.09.2003

[56] Werner, M., Baars, A., Delgado, A. 2003. Bestimmung der Wärmeleitfähigkeit niedrigviskoser Lebensmittel unter Hochdruck mittels Hitzdrahtmethode. Proceedings des 6. Dresdner Sensor-Symposium, 8.-10.12.03, Dresden, 37 – 4.

[57] Wagner, C.; Friedrich, R. 1998. Direct numerical simulation of turbulent flow through permeable or rough pipes. In: K.D. Papailiou et al. [Hrsg.]: Computational Fluid Dynamics 98, John Wiley & Sons, New York/USA, S. 238 - 243, ECCOMAS, Athen, 07.-11. September 1998.

[58] Wagner, C.; Hüttl, T.B.; Friedrich, R. 1998. Low-Reynolds-number effects derived from direct numerical simulations of turbulent pipe flow. In: Third Asian Computation Fluid Dynamics Conference, S. 189 - 194, Third Asian Computation Fluid Dynamics Conference, Bangalore/India, 07.-11. Dezember 1998

[59]Wagner, Claus; Friedrich, Rainer. 2000. DNS of turbulent flow along passively permeable walls. International Journal of Heat and Fluid Flow, 29, S. 489 - 498

[60] Wagner, W., Kruse, A., 1998. Properties of Water and Steam, Springer-Verlag, Berlin.

[61] IAPWS Release on the Viscosity of Ordinary Water Substance, 1997. IAPWS Secretariat.

[62] IAPWS Release on the Thermal Conductivity of Ordinary Water Substance,1998. IAPWS Secretariat.

[63] Brown, T. L., LeMay, H. E., 1985. Chemistry, The Central Science, 3rd Ed., Prentice-Hall Inc.

[64] Okhulkov, A. V., Demianets, Y. N., Gorbaty, W., E., 1994. X-ray-scattering in liquid water at pressures of up to 7.7 kbar - test of a fluctuation model, J. Chem. Phys., 100, 1578-1588.

[65] Sun, Q., Zheng, H., Xu, J., Hines,E., 2003. Raman spectroscopic studies of the stretching band from water up to 6 kbar at 290 K. Chem. Phys. Lett., 379, 427-431.

[66] Bett, K. E., Cappi, J. B., 1965. Effect of pressure on the viscosity of water, Nature, 207, 620-621.

[67] Tanaka, H., 2003. A new scenario of the apparent fragile-to-strong transition in tetrahedral liquids: water as an example, J. Phys. Condens. Matter, 15, L703-L711.

[68] Kawamoto, T., Ochiai, S., Kagi, H., 2004. Changes in the structure of water deduced from the pressure dependence of the Raman OH frequency, J. Chem. Phys., 120, 5867-5870.

[69] Atkins, P. W., 2001. Kurzlehrbuch Physikalische Chemie, Wiley-VCH.

[70] Zemansky, M. W., 1957. Heat and Thermodynamics, New York, London, McGraw-Hill.

[71] Wesseling, P. 2000. Principles of Computational Fluid Dynamics, Springer-Verlag Berlin, Heidelberg, New York.

[72] Patankar, V., 1980. Numerical Heat Transfer and Fluid Flow, Taylor & Francis, Bristol, PA.

[73] Oertel, H., Laurien, E., 2003. Numerische Strömungsmechanik, Vieweg Braunschweig/Wiesbaden.

[74] Noll, B., 1993., Numerische Strömungsmechanik, Grundlagen, Springer Verlag, Berlin.

[75]Lechner, R., Sesterhenn, J., Friedrich, R. 2001. Effects of compressibility and fluid properties in turbulent supersonic channel flow. Proc. 2nd Int. Symp. Turbulence and Shear Flow Phenomena, Stockholm, 27-29 June 2001.

[76] Lechner, R., Sesterhenn, J., Friedrich, R. 2001. DNS of turbulent supersonic channel flow: Effects of compressibility and wall permeability, Direct and Large-Eddy Simulation IV. Edited by B.J.Geurts et al., Kluwer Academic Publishers, pp. 29-36.

[77] Jischa, M., 1982. Konvektiver Impuls-, Wärme- und Stoffaustausch, Vieweg Braunschweig/Wiesbaden.

[78] Spurk, J.H., 2004. Strömungslehre, Einführung in die Theorie der Strömungen, 5. Auflage, Springer-Verlag Berlin Heidelberg.

[79] Rohsenow, W. M, Hartnett, J. P., Ganić, E. N., 1973. Handbook of Heat Transfer Fundamentals, McGraw-Hill Book Company, New York..

[80] Baehr, H. D., 2002. Thermodynamik, 11. Auflage, Springer-Verlag, Berlin, Heidelberg, New York.

[81] Meixner, J., Reik, H. G., 1959. Thermodynamik der irreversiblen Prozesse. In: S. Flügge (Hsrg.): Handbuch der Physik. Bd. III/2. 413 – 523.

[82] Landau, L. D., Lifschitz, E.M., 1966. Lehrbuch der Theoretischen Physik, Band VI: Hydrodynamik, Akademie-Verlag, Berlin.

[83] Saul, A., Wagner, W. 1989. A fundamental equation for water covering the range from the melting line to 1273 K at pressures up to 25000 Mpa, Journal of Physical and Chemical Reference Data, 18, 1537-1564.

[84] Watson, J. T. R., Basu, R. S., Sengers, J. V. 1980. An improved representative equation for the dynamic viscosity of water substance, Journal of Physical and Chemical Reference Data, 9, 1212-1255.

[85] Först, P., 2001. In situ Untersuchungen der Viskosität fluider komprimierter Lebensmittel, PhD Thesis, TU München.

[86] Först, P., Werner, F., Delgado, A., 2000. The viscosity of water at high-pressures-especially at subzero degrees centigrade. Rheologica Acta, 39, 566-573.

[87]Rauh, C., Baars, A., Delgado, A., 2005.Temperatur- und Geschwindigkeitsfelder in flüssigen Lebensmitteln während der Kurzzeit-Hochdruck-Behandlung. VDI-GVC Fachausschuss "Lebensmittelverfahrenstechnik", Berlin, March 7 – 9, 2005

[88] Schlichting, H., Gersten, K., 2000. Boundary Layer Theory, 8th Revised and Enlarged Edition, Springer-Verlag Berlin Heidelberg New York.

[89] Sato, H., 1960. The stability and transition of a two-dimensional jet. J. Fluid. Mech., 1, 53-80.

[90] Morgan, P. L., Armfield, S. W., 2003. An Investigation of the behaviour of Planar Jets Using a Time Accurate Fractional Step Scheme, ANZIAM J., 4(3), C550-C568.

[91] Eck., B., 1961 Technische Strömungslehre, Sechste Auflage.

[92] Moin, P., Mahesh, K., 1998. Direct numerical simulation: a tool in turbulence research, Annu. Rev. Fluid. Mech., 30, 539-578.

[93] Friedrich, R., Hüttl, T.J., Manhart, M., Wagner, C., 2001. Direct Numerical Simulations of incompressible turbulent flows Computers & Fluids 30, 555-579.

[94] Murakami, S., Mochida, A., Hibi, K., 1987. Three-dimensional simulation of air flow around a cubic model by means of large eddy eimulation, J. Wind. Eng. Ind. Aerodyn., 25, 291-305.

[95] Hinze, J. O., 1975. Turbulence, 2nd edition, New York, NY.

[96] Launder, B. E., Spalding, D. B., 1974. The Numerical Computation of Turbulent Flows, Computer Methods in Applied Mechanics and Engineering, 3, 269-289.

[97] Wilcox, D. C., 1993. The Remarkable Ability of Turbulence Model Equations to Describe Transition, DCW Industries Inc., La Canada, CA.

[98] Wilcox, D. C., 1993, Turbulence Modelling for CFD, DCW Industries Inc., La Canada, CA.

[99] Menter, F. R., 1994. Two-Equation Eddy Viscosity Turbulence Models for Engineering Applications, AIAA Journal, 32(8), 1598-1605.

[100] Vieser, W., Esch, T., Menter, F., 2002. Heat Transfer Predictions using Advanced Two-Equation Turbulence Models, CFX Validation Report, CFX-VAL10/0602.

[101] Kilimann KV, Hartmann C, Delgado A, Vogel RF, Gänzle MG., 2005. Combined high pressure and temperature induced lethal and sublethal injury of Lactococcus lactis - application of multivariate statistical analysis, submitted to International Journal of Food Microbiology

[102] Gänzle, M.G., Vogel, R.F., 2001. On-line fluorescence determination of pressure mediated outer membrane damage in *Escherichia coli*. Systematic and Applied Microbiology 24, 477-485.

[103] Casadei, M.A., Manas, P., Niven, G., Needs, E., Mackey, B.M., 2002. Role of membrane fluidity in pressure resistance of *Escherichia coli* NCTC 8164. Applied and Environmental Microbiology 68, 5965-5972.

[104] Molina-Höppner, A. 2002. Physiological response of *Lactococcus lactis* to high pressure. Doctoral thesis, Technische Universität München, Centre for Life and Food Sciences Weihenstephan

[105] Barth, T. J., and Jesperson, D. C., 1989. The Design and Application of Upwind Schemes on Unstructured Meshes. AIAA Paper 89-0366.

[106] Schiller, L., Naumann, A. Z., 1933. „Über die grundlegenden Berechnungen bei der Schwerkraftaufbereitung“, Z. Vereines Deutscher Inge., 77, 318–321.

[107] Ranz W E & Marshall W R, Jr., 1952. Evaporation from drops. Parts I & II. Chem. Eng. Progr. 48, 141-146 and 173-180.

[108] James R. DeBonis, 2000. The Numerical Analysis of a Turbulent Compressible Jet, Dissertation , Ohio State University, Cleveland, Ohio.

[109]Batchelor, G.K. & Gill, A.E., 1962. Analysis of the stability of axisymmetric jets. *J. Fluid Mech.,* 14, 529-551.

[110]Grant, A.J., 1974. A numerical model of instability in axisymmetric jets. *J. Fluid Mech.,* 66, 707-724.

[111] Andrade, E.N.C., 1939. The velocity distribution in a liquid-into-liquid jet. Part 2: The plane jet. *Physical Soc*., 51, 784-793.

[112] Sonoike K, Setoyama T, Kuma Y, Kobayashi S. 1992. The effect of pressure and temperature on the death rates of *Lactobacillus casei* and *Escherichia coli*. In: Balny C, Hayashi R, Heremans K, Masson P (Eds.), High pressure and biotechnol. London: John Libbey and Company. P 297-301

[113] Ter Steeg PF, Hellemons JC, Kok AE. 1999. Synergistic actions of nisin, sublethal ultrahigh pressure, and reduced temperature on bacteria and yeast. App Environ Micro 65:4148-4154.

[114] Kilimann KV, Hartmann C, Delgado A, Vogel RF, Gänzle MG. 2005. Combined high pressure and temperature induced lethal and sublethal injury of *Lactococcus lactis* - application of multivariate statistical analysis, submitted to Int J Food Micro.

[115] Anonymous. 2003. Scientific criteria to ensure safe food. Committee on the review of the use of scientific criteria and performance standards for safe food, food and nutrition board, board on agriculture and natural resources. The national academic press, Washington, DC.

[116] Garcia-Graells C, Hauben KJ, Michiels CW. 1998. High-pressure inactivation and sublethal injury of pressure-resistant *Escherichia coli* mutants in fruit juices. App Environ Micro 64:1566-1568.

[117] Kalchayanand N, Sikes A, Dunne CP, Ray B. 1998. Interaction of hydrostatic pressure, time and temperature of pressurization and pediocin AcH on inactivation of foodborne bacteria. J Food Prot 61:425-431.

[118] Garcia-Graells C, van Opstal, I, Vanmuysen SC, Michiels CW. 2003. The lactoperoxidase system increases efficacy of high-pressure inactivation of foodborne bacteria. Int J Food Micro 81:211-221.

[119] Kilimann, K. V., 2005. PhD Thesis, TU-München

[120] Brown D, Rothery P. 1993. Models in biology – Mathematics, Statistics and Computing. Chichester:John Wiley.